PATIENT-SPECIFIC FINITE ELEMENT MODELING OF BIOMECHANICAL INTERACTION IN TRANSCATHETER AORTIC VALVE IMPLANTATION

A Dissertation
Presented to
The Academic Faculty

by

Qian Wang

In Partial Fulfillment
of the Requirements for the Degree
Doctor of Philosophy in the
Department of Biomedical Engineering

Georgia Institute of Technology
May 2015

PATIENT-SPECIFIC FINITE ELEMENT MODELING OF BIOMECHANICAL INTERACTION IN TRANSCATHETER AORTIC VALVE IMPLANTATION

Approved by:

Dr. Wei Sun, Advisor
Department of Biomedical Engineering
Georgia Institute of Technology

Dr. Ajit Yoganathan
Department of Biomedical Engineering
Georgia Institute of Technology

Dr. Rudolph Gleason
Department of Biomedical Engineering
Georgia Institute of Technology

Dr. Stamatios Lerakis
School of Medicine
Emory University

Dr. Muralidhar Padala
School of Medicine
Emory University

Date Approved: November 5, 2014

Dedicated to my parents,
Wang Jiaxiang and Zhang Xiuhua,
for their unwavering support.

ACKNOWLEDGEMENTS

First and foremost, I would like to express my deepest gratitude to my advisor Wei Sun for his support and guidance throughout the years and pushing me to reach my full potential. I also thank him for giving me the opportunity to work with many different collaborators and allowing me to expand my skill set. I also thank my thesis committee members, Dr. Ajit Yoganathan, Dr. Rudolph Gleason, Dr. Stamatios Lerakis, and Dr. Muralidhar Padala for their mentorship and support.

I thank current members and alumni of the Tissue Mechanics Laboratory, namely Dr. Kewei Li, Dr. Thuy Pham, Dr. Eric Sirois, and Caitlin Martin for the wealth of technical advice they gave and being supporters of my interdisciplinary work in cardiovascular biomechanics. I also thank other colleagues in the Tissue Mechanics Laboratory for their tangible and intangible assistance during my time at Georgia Tech and the University of Connecticut. In particular, I would like to thank Gregory Book, Dr. Zhongwei Hu, Dr. Sonia Helena Contreras Ortiz, Dr. Haofei Liu, Dr. Shamik Bhattacharya, Dr. Wenbin Mao, Andres Caballero, and Joseph Calderan.

I would like to give special acknowledgement to Dr. Charles Primiano from the Hartford Hospital, CT and Dr. Susheel Kodali from Columbia University, NY. This work would not have been possible without their assistance and guidance on understanding cardiovascular diseases, cardiology and transcatheter aortic valve implantation procedure.

I also thank the undergraduate researchers who worked with me, and our funding sources: NIH HL104080, HL108239 grants, and AHA predoctoral fellowship 13PRE14830002.

TABLE OF CONTENTS

LIST OF TABLES

LIST OF FIGURES

SUMMARY

Transcatheter aortic valve implantation (TAVI) is an effective alternative treatment option for patients with severe aortic stenosis, who are at a high risk for conventional surgical aortic valve replacement or considered inoperable. Despite the short- and mid-term survival benefits of TAVI, adverse clinical events, such as paravalvular leak, aortic rupture, and coronary occlusion, have been reported extensively. Many of these adverse events can be explained from the biomechanics perspective. Therefore, an in-depth understanding of biomechanical interaction between the device and native tissue is critical to the success of TAVI. The objective of this thesis was to investigate the biomechanics involved in the TAVI procedure using patient-specific finite element (FE) simulations. Patient-specific FE models of the aortic roots were reconstructed using pre-procedural multi-slice computed tomography images. The models incorporated aged human aortic material properties with material failure criteria obtained from mechanical tests, and realistic stent expansion methods. TAV deployment and tissue-device interaction were simulated; and the simulation results were compared to the clinical observations. Additionally, parametric studies were conducted to examine the influence of the model input on TAVI simulation results and subsequently the potential clinical complications such as paravalvular leak, annular rupture, and coronary artery occlusion. The methodology presented in this thesis could be potentially utilized to develop valuable pre-procedural planning tools to evaluate device performance for TAVI and eventually improve clinical outcomes.

CHAPTER 1

INTRODUCTION

1.1 Background

Cardiovascular disease is the leading cause of death in the United States. Among various types of cardiovascular disease, valvular heart disease is a significant cause of morbidity and mortality; and it affects approximately 11.7% of people older than 75 years old. In the United States, it is estimated that approximately 85,000 heart valve related procedures are performed annually. Valvular heart disease is responsible for about 22,144 deaths per year [1]. The two most common valvular heart diseases are aortic stenosis and mitral valve regurgitation. In this dissertation, my research effort primarily focuses on the study of aortic valve function and the modeling of the associated aortic valve intervention techniques. Thus, I will begin this chapter with a brief introduction of the heart and its four valves, then the normal aortic valve structure and function, followed by main clinical issues and current clinical treatment techniques for aortic valve disease. Then, I will give a brief overview of current aortic valve biomechanical studies, which will lead to the motivation of my research on the modeling of minimally invasive aortic valve replacement procedure.

1.1.1 Heart and Heart Valves

The heart has four major valves: aortic, mitral, tricuspid and pulmonary valves. As shown in Figure 1.1, aortic valve is between the left ventricle and the aorta. Mitral valve is between the left atrium and left ventricle. Tricuspid valve is located between the right atrium and right ventricle. Pulmonary or pulmonic valve is between the right ventricle and the pulmonary artery. The common function of these four valves is to ensure unidirectional flow of blood in and out of the heart. The four valves are primarily passive structures in terms of biomechanical functions, i.e., they open and close due to the differential blood pressure on both sides of the valve leaflets. Closure of the valve is achieved by coaptation of the leaflets (or cusps). Proper coaptation of the leaflets prevents backflow of blood. Diseased valves often involve improper coaptation and closure of the leaflets; and the two most common heart valve diseases are stenosis and regurgitation. Stenosis is narrowing of the valve orifice, which leads to restriction of the blood flow. Conversely, regurgitation is backflow of blood through a defective heart valve. Other valvular diseases are rheumatic diseases, which results in valve leaflet prolapse, or billowing of the leaflets, and sometimes cause regurgitation. The aortic mitral and mitral valves are most commonly affected because they are located on the left side of the heart, which is responsible to pump blood to the rest of the body and has higher pressure and more turbulent hemodynamic conditions.

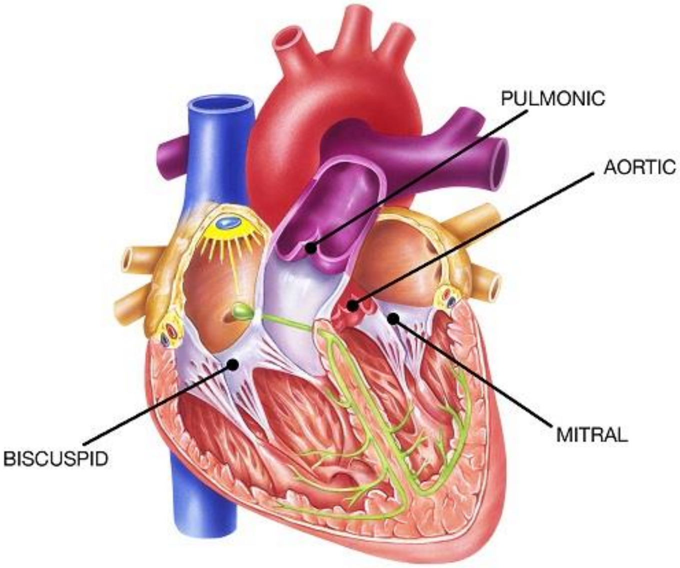

Figure 1.1 Anatomical structure of the heart and the heart valves (adopted from www.stdom.com)

The blood circulation inside the heart is shown in Figure 1.2. Blood pressure rises in the left ventricle at the beginning of systole. When left ventricle contracts and the left ventricle pressure is higher than the aortic pressure as shown in Figure 1.3, the aortic valve opens, allowing blood to enter the aorta from the left ventricle. When ventricular systole ends, pressure in the left ventricle rapidly drops (Figure 1.3), and the aortic pressure forces the aortic valve to close. As the atrium contracts, blood flows from the left atrium into the left ventricle through the open mitral valve. When the ventricle is full, the mitral valve shuts. This prevents blood from flowing backward into the atrium while the ventricle contracts.

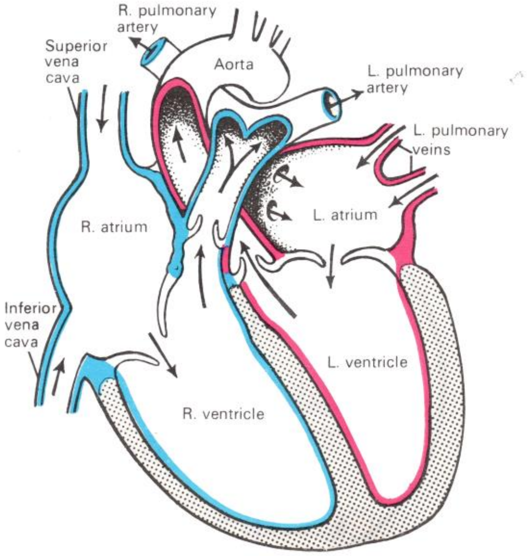

Figure 1.2 Blood circulation inside human heart as well as between the heart and the rest of the body (adopted from thefoodweeat.co.uk)

Cardiovascular disease is the leading cause of death for both men and women in the United States, and valvular heart disease constitute a major part of the cardiovascular disease [2]. Among valvular heart diseases, aortic valve diseases occur frequently and result in more dire consequences due to its high pressure load bearing nature during the cardiac cycle. There are two common aortic valve diseases: 1) aortic stenosis, where the valve cannot open completely, thus obstructing blood flow from the left ventricle to aorta, and 2) aortic insufficiency, also called aortic regurgitation, where the aortic valve is incompetent and blood flows passively back to the left ventricle.

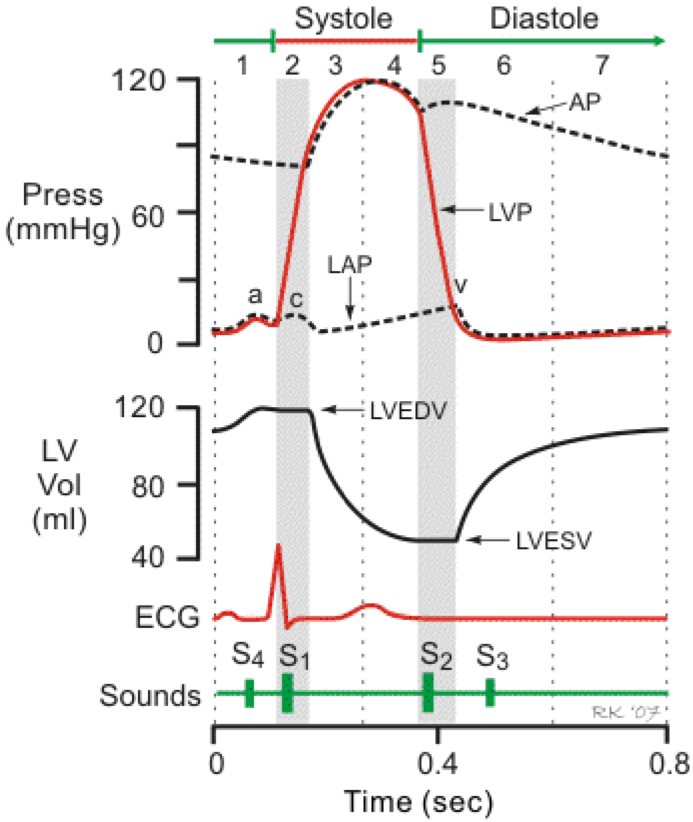

Figure 1.3 Aortic and left ventricular pressure curves during cardiac cycle (adopted from http://www.cvphysiology.com)

1.1.2 Aortic Stenosis and Treatments

Aortic stenosis (AS) is the narrowing of the aortic valve due to the buildup of calcium deposits. AS is the most common valvular heart disease in developed countries [3] and its prevalence is growing with an aging population [4, 5]. AS affects about 3% of the population above the age of 75 years, and leads to greater morbidity and mortality than any other cardiac valve disease [6]. The prevalence of AS in patients older than 65 years is estimated at 2% for severe stenosis, 5% for moderate stenosis, and 9% for mild stenosis [7]. Severe obstruction of blood flow to the aorta from the left ventricle is usually characterized (Table 1.1) by the following: (1) an aortic jet velocity greater than

4 m/sec; (2) a mean systolic pressure gradient exceeding 40 mm Hg in the presence of a normal cardiac output; or (3) an effective aortic orifice less than approximately 1.0 cm^2 in an average-sized adult (i.e., $< 0.6\ cm^2/m^2$ of body surface area, approximately 25% of the normal aortic orifice of 3.0 to 4.0 cm^2) [7]. After the appearance of symptoms, AS is associated with a high mortality rate (approximately 50% in the first 2 years) if left untreated [8, 9].

Table 1.1 Severity of aortic stenosis

Degree of aortic stenosis	**Mean gradient (mmHg)**	**Aortic valve area (cm^2)**	**Jet velocity (m/sec)**
Mild aortic stenosis	< 25	> 1.5	< 3.0
Moderate aortic stenosis	25 - 40	1.0 - 1.5	3.0 - 4.0
Severe aortic stenosis	> 40	< 1.0	> 4.0

Currently, there is no effective medical therapy for severe AS [10]. Surgical aortic valve replacement (SAVR) with either a mechanical or bioprosthetic heart valve (Figure 1.4), also called a tissue valve, is the standard of care for patients with severe symptomatic AS. Not only does it offer symptomatic relief, the operation improves long term survival. In the absence of serious comorbidities, the procedure is associated with low operative mortality. In the United States, there were over 75,000 aortic valve replacement procedures performed in 2008 [11]. Mechanical heart valves shown in Figure 1.4a are usually made from metal and/or pyrolitic carbon, a hard ceramic-like material. Bioprosthetic heart valves shown in Figure 1.4b are normally made from soft, leather-like biological materials and are intended to mimic the function of the native aortic valve. A mechanical heart valve could last a lifetime, but patient requires a daily dosage of anticoagulant medicine. Patients on anticoagulant medicine must follow dietary restrictions and cannot participate in physical activities or sports that might cause bleeding. Alternatively, implantation of a bioprosthetic heart valve is also not ideal. Although bioprosthetic heart valves do not induce blood clotting and thus do not require anticoagulant medicine, they eventually fail due to fatigue or calcification and need to be replaced surgically or by a less invasive treatment. Compard with the lifetime durability of the mechanical heart valve, in the best-case scenario, the bioprosthetic heart valve could only last 20 years.

Nevertheless, in clinical practice it was reported that approximately 50% of patients with severe AS are referred for open heart surgery and only about 40% undergo SAVR according to data from 10 United States centers of various sizes and geographic distribution [12]. Reasons for not undergoing AVR included high perioperative risk, advanced age, lack of symptoms, and patient/family refusal [12-14]. Therefore, there is a pressing need for less invasive, non-surgical techniques for those high risk patients.

(a) (b)

Figure 1.4 Representatives of mechanical and bioprosthetic heart valves: (a) St. Jude mechanical heart valve with two semicircular leaflets and (b) Carpentier-Edwards PERIMOUNT bioprosthetic heart valve with three tissue leaflets (adopted from www.heart-valve-surgery.com and my.clevelandclinic.org)

1.2 TAVI Procedure

For the inoperable [15] and “high risk” [16] patients, minimally-invasive transcatheter aortic valve implantation (TAVI) presents a viable treatment option [17]. Since the first-in-man TAVI was performed in 2002 [18], more than 90,000 patients worldwide [19] have benefited from this revolutionary procedure. Short and mid-term clinical results are promising and show that TAVI can significantly improve valve hemodynamics and patient quality of life with the added benefits of lower operative risk and shorter recovery time compared to SAVR [20, 21].

The TAVI procedure were described in detail by Webb et al. [22] in 2006. Briefly, patients receive a general anesthesia with TEE guidance when the procedures are performed to facilitate sheath placement and removal. Aortic root angiography is usually used to help position the prosthesis. Before the TAVI procedure, balloon valvuloplasty can be performed with a balloon slightly smaller than the diameter of the TAV. If retrograde transfemoral is chosen as the TAVI access technique, the delivery sheath is inserted over a guidewire into the femoral artery. The steerable catheter is used to direct the prosthesis through the aorta and cross the stenotic native valve. After the TAV is positioned coaxially with the native valve, the prosthesis is deployed during rapid ventricular pacing under the TEE and angiographic guidance (Figure 1.5). Angiography and TEE are also performed to reassess valve competency and coronary patency. Once the delivery system is retrieved from the patient, the femoral access site is closed surgically.

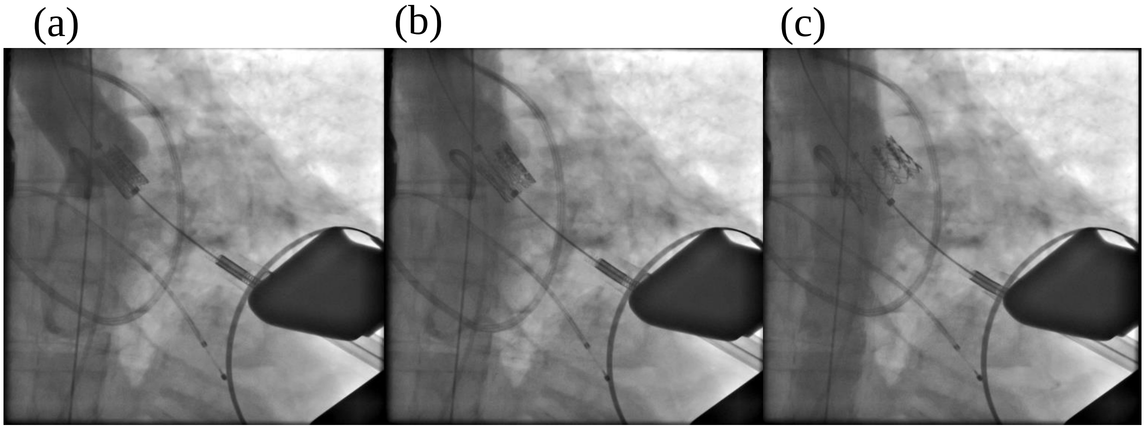

Figure 1.5 (a) Balloon-mounted prosthetic valve positioned adjacent to native valve calcification (b) Partial inflation of the deployment balloon (c) Full inflation of the deployment balloon. (Images are obtained from Hartford Hospital, CT with Institutional Review Broad approval).

1.3 TAVI Complications

Ideally an implanted TAV device should ensure optimal diastolic coaptation with negligible regurgitation, maintain a minimal transvalvular pressure gradient during systole, minimize downstream turbulence and stagnation, and allow physiological coronary artery flow patterns [23]. However, in contrast to traditional SAVR, where the surgeon has direct access to the aortic root to suture the prosthesis into place, in TAVI, the prosthesis is remotely delivered, preventing the physician from knowing how the suture-less device will interact with the surrounding tissues. Furthermore, unlike in SAVR where the calcified native valve tissues are excised, in TAVI, these tissues are left intact and may become displaced and/or alter the final TAV stent shape during deployment, owing to many procedural uncertainties. Consequently, despite worldwide clinical successes, there are still many complications associated with TAVI including: paravalvular leak (PVL), stroke, device migration, aortic root rupture, and coronary artery occlusion [24-27].

PVL due to gaps between the deployed stent and the surrounding tissue is the most frequent TAVI complication (Figure 1.6). In the Placement of AoRtic TraNscathetER Valve (PARTNER) trial [15], 68% of patients exhibited trace to mild PVL at 30 days, while 12% had moderate to severe PVL, representing much higher rates compared to conventional SAVR. Still more concerning, the 2-year results from the PARTNER trial showed that even mild PVL was associated with increased mortality [28]. Significant PVL is typically the result of 1) annulus-prosthesis mismatch due to the pattern or extent of calcification or annular eccentricity, 2) undersizing of the device, or 3) suboptimal positioning of the device [25]. In some cases post-implantation balloon dilation of the valve is considered to correct PVL; however, it is not always effective and has been shown to be associated with a higher incidence of cerebrovascular events [25, 29]. Balloon postdilation increases the interaction force between the TAV stent and the surrounding native aortic tissue, thus increasing the chance for calcium deposits to become dislodged and released into the blood stream causing stroke.

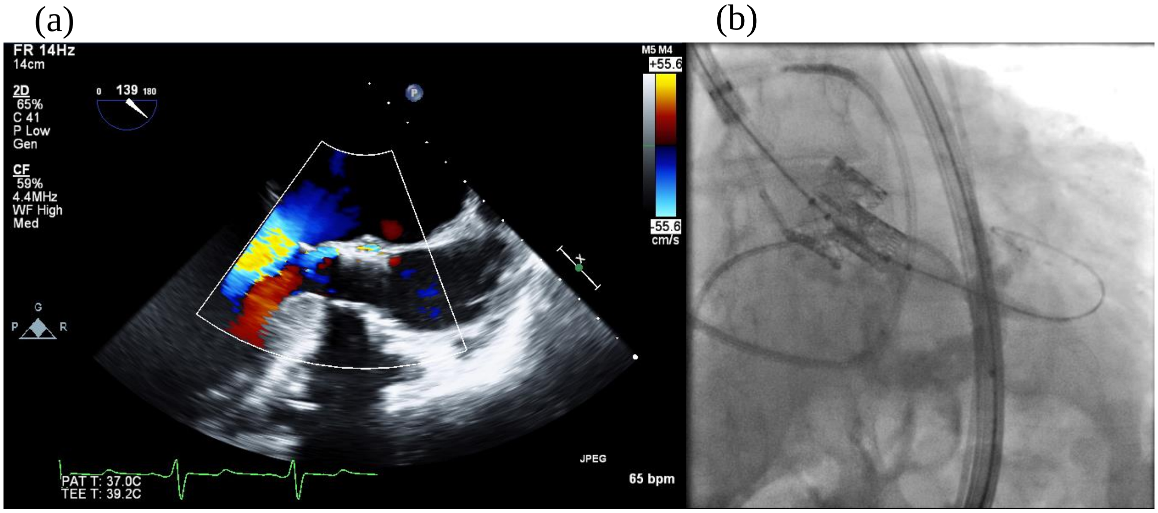

Figure 1.6 Echocardiogram and angiogram of a TAVI case. The implantation height of the first TAV was suboptimal, as the native leaflet insertion point was adjacent to the lower edge of the stent. PVL (Figure 1.2a) was present after the deployment of the first TAV. Subsequently, a second TAV (Figure 1.2b) was deployed inside the first one, in an attempt to correct the complication due to suboptimal valve positioning. (Images are obtained from Hartford Hospital, CT with Institutional Review Broad approval).

TAVI-associated stroke is an invariable concern. The 30-day major stroke rate in the PARTNER trial was 3.8% and 5% in cohorts A and B respectively [15, 16]. A large multicenter registry showed that 54% of strokes occurred within 24 h of the TAVI procedure [29, 30]. Along with balloon postdilation, valve dislodgement due to insufficient friction between the stent frame and the aortic wall, has also been identified as an independent predictor of acute stroke [29]. Antithrombotic treatment is generally used after TAVI to reduce stroke risk, while several embolic protection devices have been developed for use during TAVI in the hope that they may prevent cerebral embolization.

Aortic root rupture (Figure 1.7) during TAV deployment is a more rare but catastrophic complication of TAVI reported in about 1% of cases [26]. It is a major concern particularly for balloon-expandable TAVI devices, because the balloon expansion force can exert large forces on the stent and surrounding tissues. Left ventricular outflow tract (LVOT) calcification, aggressive device oversizing, small annular size, and excessive annular calcification have all been identified as risk factors for aortic rupture with balloon expandable TAVI devices [31, 32]. A ruptured aortic root can only be treated with emergency open heart surgery.

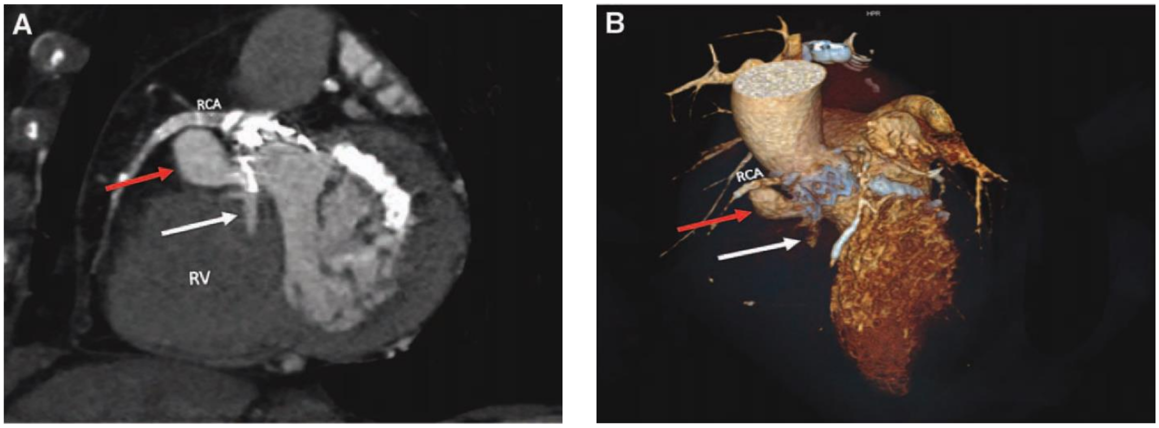

Figure 1.7 (a) Two-dimensional CT scan and (b) three-dimensional CT reconstruction showing the presence of a contained aortic root rupture with a false aneurysm (red arrow) [33].

During deployment the TAV may also displace the native leaflets or calcification and cause coronary obstruction (CO). CO is also a rare, but life-threatening complication of TAVI [24, 34, 35]. Baseline and procedural variables associated with CO include: advanced age, female sex, no previous coronary artery bypass graft, the use of a balloon-expandable TAV, and previous surgical aortic bioprosthesis. Additionally, a lower-lying coronary ostium (<12 mm above the annulus) and a shallow SOV (<30 mm) have been identified as anatomical factors associated with CO. In most cases, CO can be successfully treated by percutaneous coronary intervention (Figure 1.8); however, hemodynamic support and/or conversion to open heart surgery are often necessary.

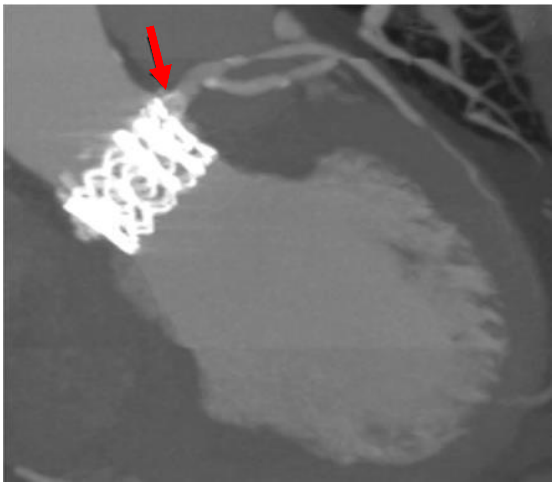

Figure 1.8 Multi-detector computed tomography scan showing the spatial relationship between the prosthesis and coronary artery (red arrow) [24].

1.4 TAVI procedural considerations

A successful TAVI procedure is the result of proper device selection and deployment strategy; however, determining these factors is not trivial. A patient's unique aortic root anatomy, tissue properties, and dimensions are all of importance.

1.4.1 Aortic Root Anatomy

The healthy aortic root (Figure 1.9) is defined as the portion of the LVOT delineated by the sinotubular ridge superiorly and the bases of the valve leaflets inferiorly [36]. It is comprised of the sinuses, the aortic valve leaflets, the commissures, and the interleaflet triangles. The sinuses are the expanded portions of the aortic root which are confined proximally by the valve leaflet attachments and distally by the sinotubular junction. The valve leaflets are attached to the aortic root wall in a semilunar fashion. Proximal to the leaflets, is the aortic annulus. The term “annulus” is frequently used in the TAVI device sizing process, but it should be noted that in this context the term “annulus” refers to a location rather than a structure. The aortic annulus is not in fact a clearly defined structure. The posterior aspect of the annulus between the left and non-coronary leaflets is supported by fibrous tissue connected to the mitral valve for approximately 55% of its circumference, while the remainder is supported by ventricular muscle [37, 38]. Each of these sub-regions has distinct nonlinear, anisotropic material properties, and plays a unique role in the aortic biomechanics. For instance, the fibrous trigones located proximally to the sinuses and along the annulus are much stiffer than the aortic tissue to provide mechanical support.

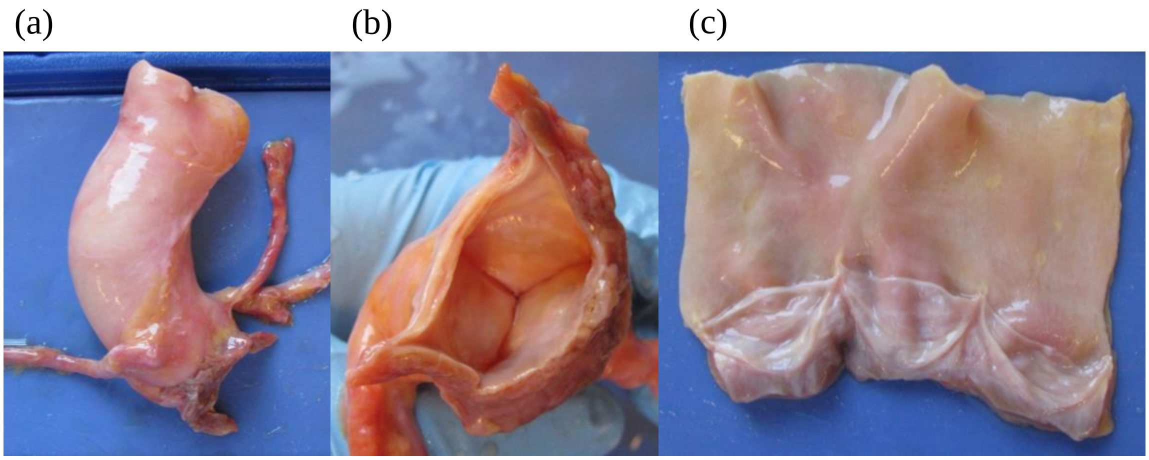

Figure 1.9 (a) Side and (b) bottom views of a human aortic root with (c) three aortic leaflets.

For patients with AS, there is also the presence of calcification to consider (Figure 1.10). AS patients present with mild, moderate, or severe degenerative aortic valve calcification clinically [39]. A mildly calcified valve is characterized by small, localized, and nondense calcium deposits, a moderately calcified valve has dense calcification in some but not all leaflets, and a severely calcified valve has severe calcification involving the majority of the leaflets. Porcelain aorta is also prevalent in patients with severely calcified valves. Calcium deposition can vary greatly among patients, and adds to the already complex anatomy of the healthy aortic root.

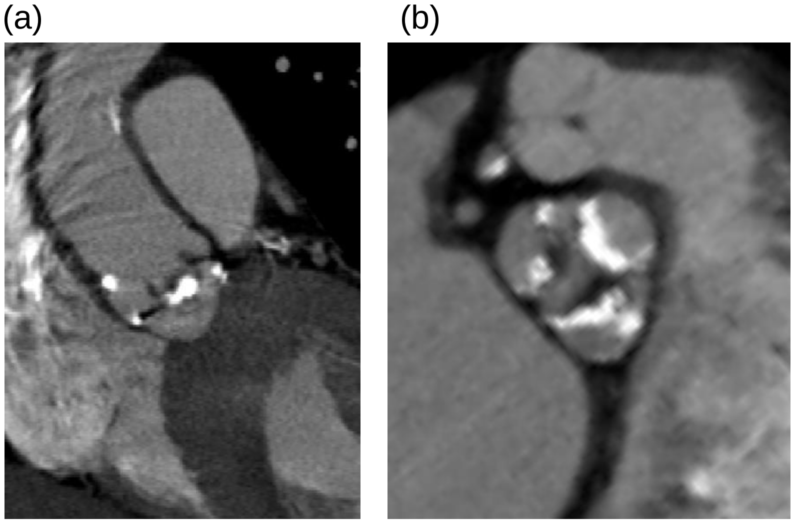

Figure 1.10 MSCT images of a stenotic aortic valve in long-axis and short-axis views.

1.4.2 Valve Sizing for TAVI

Accurate measurement of the aortic annulus is essential for appropriate TAV sizing. Incorrect valve sizing may lead to PVL, valve embolization, patient-prosthesis mismatch, or catastrophic annular rupture [40]. However, while TAV devices typically have a circular cross section, several studies have shown that aortic annulus (Figure 1.11) is not circular, but rather elliptical in nature, so there is an inherent mismatch in geometries. Recent studies show that area-derived and circumference-derived cross-sectional annulus diameters may be more applicable for TAV sizing as they account for this eccentricity [41-45]. Still the complex shape of the aortic root (Figure 1.12) makes accurate dimensional measurements intrinsically difficult, particularly based on 2-dimensional imaging modalities such as echocardiography. Accordingly, 3-dimensional multi-slice computed tomography (CT) has become the preferred modality for aortic annular measurement in TAVI procedures [41, 44, 46-48].

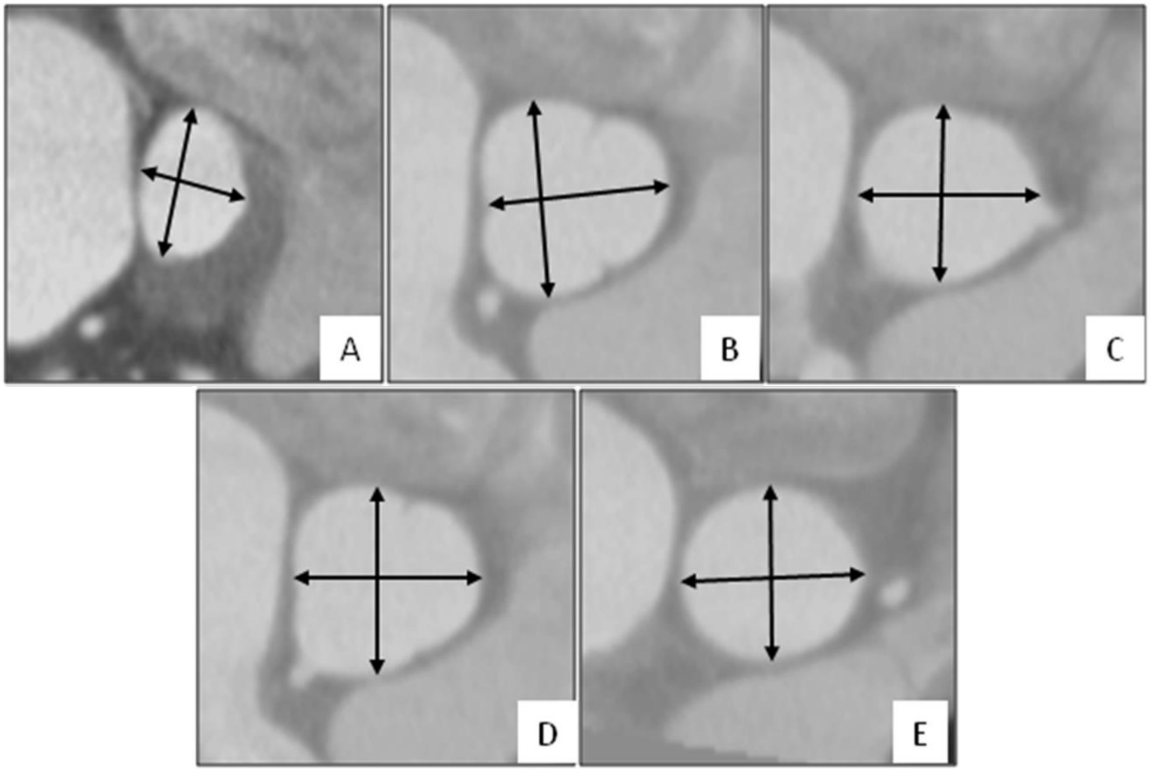

Figure 1.11 Representative short axis views with diameter measurement lines at the annulus (A), sinus of Valsalva (B), left coronary ostium (C), right coronary ostium (D), and ascending aorta (E). Major axis (vertical) and minor axis (horizontal) lines are indicated on the cross-section images.

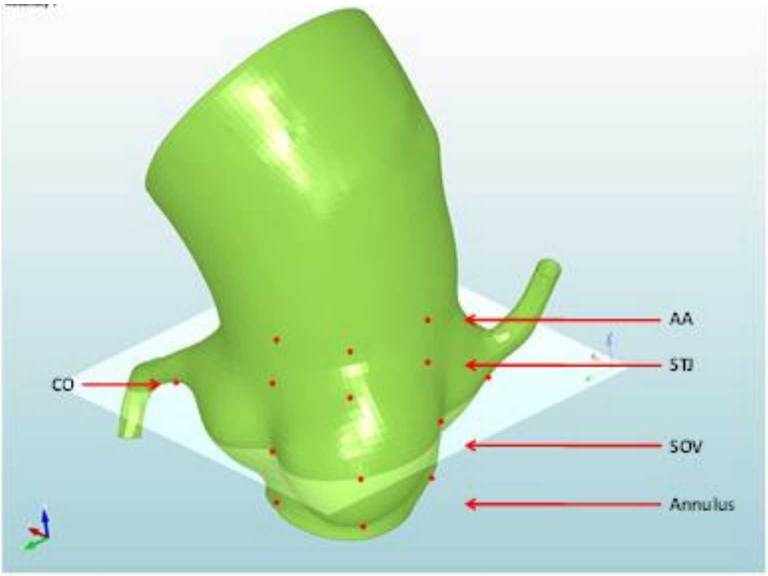

Figure 1.12 Reconstructed finite element model of a human aortic root using CT scans with a cross-sectional plane and the landmark points created for each height level, ascending aorta (AA), sino-tubular junction (STJ), sinus of Valsalva (SOV), aortic annulus, and coronary ostia (CO).

1.4.3 TAVI Devices

Currently, the balloon-expandable Edwards SAPIEN, SAPIEN XT (Edwards LifeSciences, USA), and self-expandable Medtronic CoreValve (Medtronic, USA) are the commercially available TAVI devices in the US (Figure 1.13). The Edwards SAPIEN valve is composed of a trileaflet bovine pericardial valve sutured to a cylindrical stainless steel stent. The second generation Edwards SAPIEN XT valve is comprised of a cobalt-chromium stent and three bovine pericardial leaflets. Meanwhile, the CoreValve is made of three porcine pericardial leaflets sewn to an asymmetrical self-expanding Nitinol frame. While success has been demonstrated for several first-generation TAVI systems, several design limitations have been identified which have contributed to suboptimal clinical outcomes.

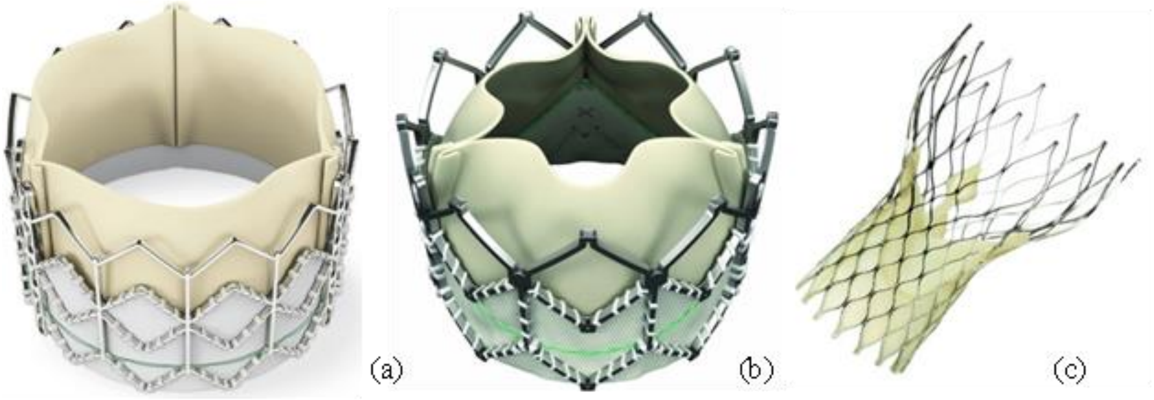

Figure 1.13 Representatives of transcatheter aortic valve devices: (a) Edwards SAPIEN transcatheter aortic valve, (b) Edwards SAPIEN XT transcatheter aortic valve and (c) Medtronic CoreValve system (adopted from www.edwards.com and www.medtronic.com)

Many new-generation TAVI devices (Figure 1.14) addressing these limitations are currently in the early stages of clinical evaluation [49, 50]. Modifications in the new devices include the ability to reposition the valve before final deployment, features to reduce PVL, and the introduction of low-profile delivery systems.

The decision to implant a particular bioprosthesis depends largely on the availability of the device types and sizes, the experience of the clinician with each device, and pre-procedural anatomical assessment of the vascular access site and the aortic annulus. Although multimodality imaging such as echocardiography, CT, angiography, and cardiovascular magnetic resonance are usually used for detailed anatomical screening, many TAVI-related complications remain due to the fact the TAVI does not allow the prediction of the interaction between the suture-less stent and native tissue before the procedure. Therefore, TAVI device selection based on biomechanical evaluation may lead to improved patients outcomes.

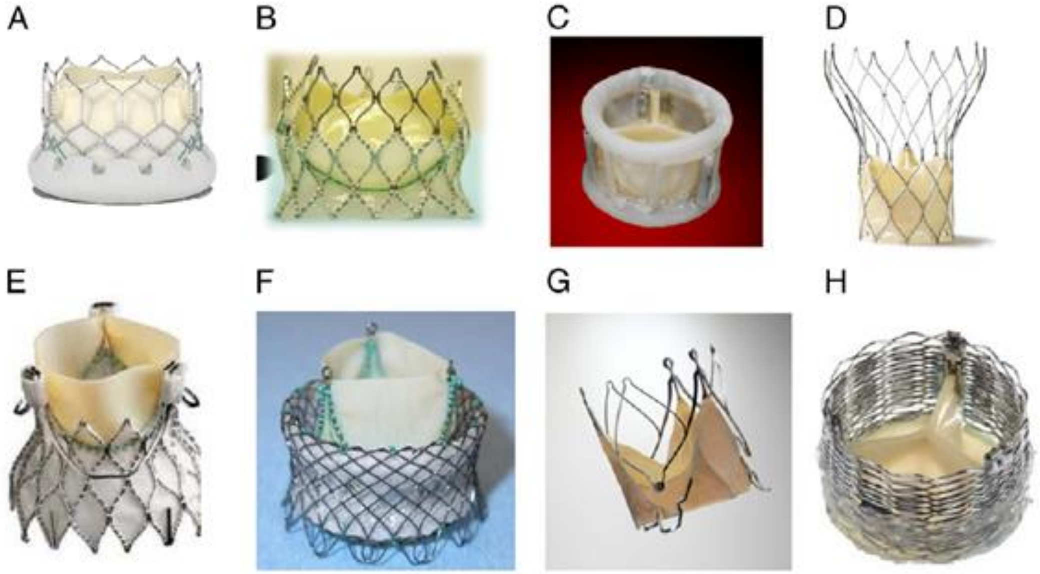

Figure 1.14 New generation transcatheter aortic valve systems [25]. (A) SAPIEN 3 (Edwards Lifesciences, Irvine, California). (B) CENTERA (Edwards Lifesciences). (C) Direct Flow Medical (Direct Flow Medical, Santa Rosa, California).
(D) Portico (St. Jude Medical, St. Paul, Minnesota). (E) Engager (Medtronic, Minneapolis, Minnesota). (F) Heart Leaflet Technologies (Heart Leaflet Technologies, Maple Grove, Minnesota). (G) JenaValve (JenaValve Technology, Munich, Germany). (H) Sadra Lotus Medical (Boston Scientific SciMed Inc., Maple Grove, Minnesota).

1.5 Biomechanical Evaluation of TAVI

Due to the significant differences between the SAVR and TAVI procedures, it is important to evaluate the efficacy and potential risk of the TAVI procedure using computational and experimental engineering analysis. In this section, major findings and limitations of the current studies in the literature on biomechanical factors related to TAVI deployment considerations using computational and experimental methods were summarized.

In a percutaneous, TAVI procedure, a crimped valve is remotely delivered through the vasculature via catheter to the site of the diseased valve annulus. Once in place, the valve is expanded (by balloon or self-expansion) to a diameter larger than that of the native root (also called “oversizing”). The interactive force between the stent and the calcified aortic root effectively locks the TAV in position. During this process, the stent can become partially embedded in the surrounding tissue or be deformed into an oval shape which can adversely affect valve hemodynamics and durability, in the case where the aortic root is heavily calcified and non-extensible [51]. Since there is a large variation in human stenotic aortic valve properties, e.g. annulus size, sinus height, coronary ostia location [45, 46, 52] and tissue stiffness [53, 54], determination of the tissue-device interaction forces is a non-intuitive, non-trivial task. Yet, not all patients have suitable root anatomy and tissue properties for TAVI. Currently the Edwards SAPIEN and SAPIEN XT valves are only available in three sizes - size 23, size 26, and size 29, while there are numerous valve sizes for their surgical counterparts. This lack of TAV sizes limits the patient population suitable for this technique and increases the possibility of patient-prosthesis mismatch. Moreover, it reflects a lack of systematic study on the biomechanics involved in TAVI.

Many catastrophic TAV failures observed in clinics can be explained from the biomechanics perspective. For example, a TAV positioned too high in the root close to the coronary ostia may cause impairment or occlusion of coronary artery flow, resulting in myocardial infarction. On the other hand, if positioned too low, the TAV may induce conduction problems and/or damage to the anterior mitral leaflet. Furthermore, ill positioning, either too high or too low with respect to the annulus, can also result in regurgitation if the TAV fails to seal the annulus. An aggressively oversized stent may cause aortic injury due to excessive radial forces, while a significantly undersized stent may migrate due to insufficient radial forces or cause aortic regurgitation secondary to PVL. Excessive or asymmetric calcification may also result in PVL due to incomplete apposition of the prosthesis within the native annulus. Thus, a quantitative understanding of the aortic tissue-TAV biomechanical interaction is essential for the science-based design of next-generation devices, and an enabling step towards patient-specific device selection and procedural planning. In the proceeding sections the current experimental and computational work to study the biomechanics associated with TAVI will be discussed.

In addition to prosthesis positioning, the angle of LVOT to ascending aorta may be important for proper seating of the entire prosthetic frame within the aortic root, with an increased angle favoring PVL after implantation.

1.5.1 Experimental Studies

In vitro experiments have been used to study aortic fluid and structural mechanics in response to TAVI. While in vivo flow patterns can be visualized using imaging modalities such as transthoracic echocardiography, in vitro experiments allow for controlled parametric evaluation of TAV performance with superior spatial and temporal resolution. In addition, because it is challenging to obtain in vivo tissue properties and biomechanical parameters, in vitro structural experiments have been adopted to measure the compliance of human aortic roots and TAV - native tissue interactions.

1.5.1.1 In Vitro Hemodynamic Studies

Particle image velocimetry (PIV) has been used extensively to quantify in vitro flow characteristics for TAVI with the Edwards SAPIEN, Medtronic CoreValve, and Boston Scientific Lotus Valve (Boston Scientific, USA) devices [55-57]. Using PIV, Stühle et al. [57] have shown that the peak flow for the SAPIEN valve is similar to that of the native aortic valve. Saikrishnan et al. [55] have shown that the Lotus Valve system composed of bovine pericardial leaflets and a Nitinol frame, also displays very good hemodynamic performance with no regions of stagnation in the vicinity of the valve. However, the results of Ducci et al. [58] suggest that SAPIEN and CoreValve implantation significantly reduces flow activity at the sinuses of Valvsalva. The observed flow stagnation may promote thrombus formation and increase the incidence of ischemic events post-TAVI.

Several groups have also investigated the effects of sub-optimal deployment on TAV flow characteristics. Scharfschwerdt et al. [56] investigated the effects of SAPIEN XT deployment in elliptical annuli, as exhibited by many bicuspid aortic valve patients. The results showed that while feasible, noncircular deployment could lead to increased leakage. Similarly, Kuetting et al. [59] have shown that elliptical stent deployment for the CoreValve device may result in worsened valve function and regurgitation. Gunning et al. [60] evaluated the potential for turbulent blood flow and blood cell damage due to eccentric TAV deployment. There were not substantial differences in the effective orifice areas and mean transvalvular pressure gradients between the circular and eccentrically deployed valves. However, eccentric deployment induced asymmetric systolic jet formation, which increased shear stresses and regions of turbulent flow. Groves et al. [61] examined the effects of TAV positioning on the aortic root fluid dynamics and showed that TAVs should be positioned as close to the native valve annulus as possible to provide optimal hemodynamics in the sinuses of Valsalva and ascending aorta. Thus it is clear that sub-optimal TAV deployment may adversely affect hemodynamic performance.

In vitro fluid experiments have also been used to develop an elastic model of the ascending aorta with aortic calcification [62], and to evaluate a new trileaflet polymer TAV design [63]. These studies demonstrate the importance of in vitro methods for assessing TAV hemodynamic performance; however, several limitations exist in these experiments which prevent the characterization of TAV device-tissue interactions. 1) The aortic root geometry was incompletely represented with a lack of LV and calcification descriptions, and 2) the human aortic tissues were inaccurately modeled with idealized surrogate materials such as acrylic plastic and silicone.

1.5.1.2 In Vitro Structural Mechanic Studies

Because successful TAV deployment and function relies heavily on the device-tissue interaction, an understanding of the aortic tissue structural mechanics is also of importance. Li et al. [64] measured and compared the structural compliance of human and porcine aortic roots in different regions through whole-vessel pressure inflation tests. The tissue stiffness was similar for all three human sinuses in the physiological pressure range. The human aortic tissues were significantly stiffer than the corresponding porcine tissues, suggesting that the porcine model may not be representative of the typical TAVI patient (≥65 years old). To study TAV stent-aortic tissue interaction mechanics, Mummert et al. [65] deployed self-expandable woven stents in excised ovine and porcine aortic roots. They found that the coefficient of friction between the tissue and stent is approximately 0.10 ± 0.01, and regardless of the aortic annulus size and tissue species, a minimum of approximately 2.5 mm in annular dilatation, induced by about 60N of radial force applied by the expanded stent, is needed to anchor a stent in the aortic root and prevent device migration. While they were able to quantify important tissue-stent contact variables for self-expanding TAV stents including the stent radial expansion force, stent pullout force, and the annulus deformation response, the main limitation of this study, was that the experiments were conducted on animal rather than human heart tissues.

1.5.2 Computational Studies

Using computational methods, in vivo TAV device interactions with human tissues can be predicted from in vivo and in vitro testing data. Current imaging modalities such as 3D echocardiography, magnetic resonance imaging, and CT, allow for accurate reconstruction of anatomical structures to be used in computational analyses [66, 67]. Recently, a number of researchers have employed finite element (FE) and computational fluid dynamics (CFD) methods to investigate the structural and hemodynamic performance of TAV devices within patient-specific aortic anatomy. With the proper validation, these models have the potential to be applied to new-generation TAV device design and optimization, and TAVI pre-operative planning.

1.5.2.1 FE Analysis

FE analysis has been used to evaluate the structural performance of TAV leaflets and stents. Li et al. [68] simulated the deformation of a pericardial bioprosthetic valve under quasi-static loading conditions to examine the effects of different material properties and tissue thickness on the leaflet stress distribution (Figure 1.15). Their results showed that, as expected, leaflet stresses decrease with increasing tissue thickness, and that under the same loading and boundary conditions, bovine pericardium leaflets have a lower peak stress than porcine pericardium leaflets. In a comparable study, Smuts et al. [69] investigated the influence the leaflet material and orientation on pericardial bioprosthetic valve function. It was concluded that kangaroo pericardium is superior to bovine pericardium for TAV applications owing to its lower thickness and greater extensibility. In both studies [68, 69] it was concluded that the tissue fiber orientation should be aligned with the circumferential direction of the valve. Sun et al. [70] used a similar approach to investigate the impact of elliptical TAV deployment due to severe aortic calcification on valve function (Figure 1.16). They found that the distorted elliptical TAV configuration induced elevated leaflet stresses and central aortic regurgitation, which has since been confirmed by in vitro experiments [56, 59, 60]. The results from these studies have important implications for TAV design. Such analyses could pave the way for the design of next-generation TAV devices with improved durability and robustness to non-optimal deployment configurations.

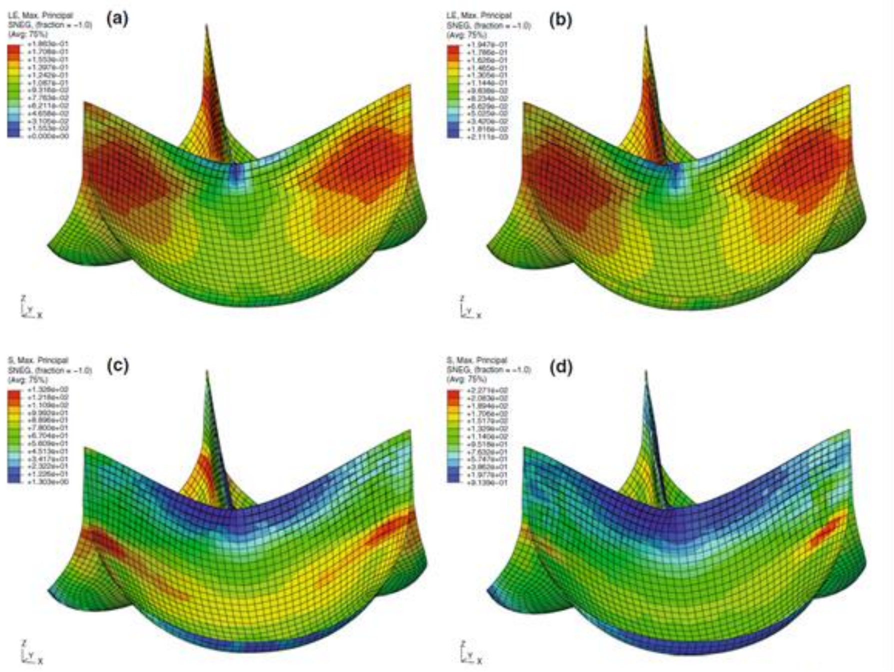

Figure 1.15 FE simulation results of PAV (on aortic side) with different material properties: maximum principal strain distribution of PAV with (a) BP and (b) PP and maximum principal stress (PSI) distribution of PAV with (c) BP and (d) PP. Note the mean thickness of each material was used in these simulations [68].

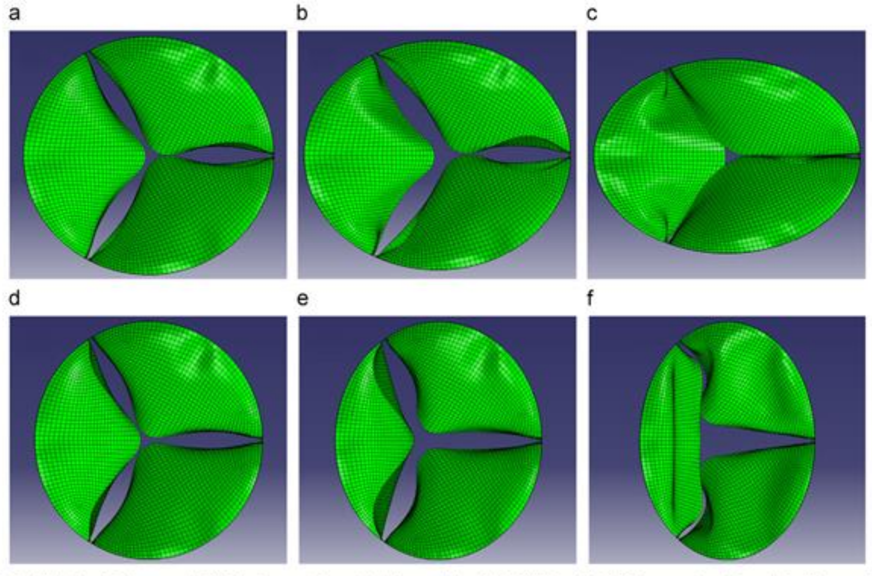

Figure 1.16 Six elliptical models of asymmetric TAV [70]. The first row is Scenario 1 with eccentricity of (a) 0.3, (b) 0.5, and (c) 0.68. The second row is Scenario 2 with eccentricity of (d) 0.3,(e) 0.5, and (f) 0.68.

In order to quantify TAV device-tissue interaction forces, several FE-based approaches have been implemented. The first approach involves the analysis of the deployed stent shape to inversely determine radial forces. Gessat et al. [71] developed a spline-based method to reconstruct deformed CoreValve stent geometry from post-TAVI CT images. Local stent deformations were determined by comparing the nominal and deformed stent geometries and were described by a set of displacements vectors. These displacement boundary conditions were then applied to an undeformed CoreValve FE model using an iterative relaxation algorithm until the deformed stent geometry was achieved [72], and the radial components of the stent-tissue interaction force could be extracted. Hopf et al. [72] have also used a similar approach to determine patient-specific contact forces between a CoreValve implant and the surrounding tissue. While these studies provide meaningful insight for improved stent design, it is difficult to determine the possible mechanisms for altered stent deformation when the deployment process and surrounding tissue are not included in the analysis. Through TAV deployment simulations in idealized LVOT geometries, Tzamtzis et al. [73] has shown that the host tissue geometry and stiffness may impact the radial contact force between the stent and tissue. Furthermore, because this approach is retrospective, it is not suitable for predicting possible TAVI related complications in an incoming patient.

There has been a recent push in the field to develop computational methods for the patient-specific analysis of TAV deployment in order to determine the precise effects of the aortic geometry and tissue properties. Capelli et al. [74] and Wang et al. [75] were among the first groups to publish patient-specific FE analyses of TAVI deployment. These analyses showed that patient-specific geometry induces asymmetric stress distributions on the device and tissue [74, 75], and impacts a particular patient’s risk of PVL, CO, and rupture [75]. Auricchio et al. [76], Gunning et al. [77], and Morganti et al. [78] have since shown that TAV leaflets may become distorted when the device is deployed within a realistic rather than an idealized and circular aortic root geometry;

thus, patient-specific analyses are important for predicting device function in addition to device-tissue interactions. Device positioning to align the TAV commissures with the native aortic valve commissures may also be important for reducing TAV leaflet stresses and consequently achieving a durable result [77]. More sophisticated FE models, which include the aortic valve calcification in addition to the aortic root and leaflets [72, 74, 78-81], have demonstrated that the extent and location of calcium deposits significantly affect the stent expansion process and a patient's risk of aortic root rupture during deployment [80]. The most complex patient-specific TAVI FE model in the literature to data presented by Wang et al. [80], which includes the aortic root, aortic leaflets, calcification, anterior mitral leaflet, and surrounding myocardium, with elastic and failure properties derived from human tissue mechanical tests, has been used for retrospective and prospective analysis of multiple TAVI patients. The simulation results for an exemplary retrospective case indicated that SAPIEN deployment would induce aortic root rupture below the left main coronary artery due to the stent pushing a large calcium deposit into the left coronary sinus during expansion (shown in Figure 1.17). Rupture in this location was also observed in the actual clinical procedure for this patient. The model predictions for potential PVL and CO were also in good agreement with clinical evaluations. It is hoped that with further validation of these modeling techniques, TAVI engineering analyses could become a part of clinical practice to improve patient outcomes.

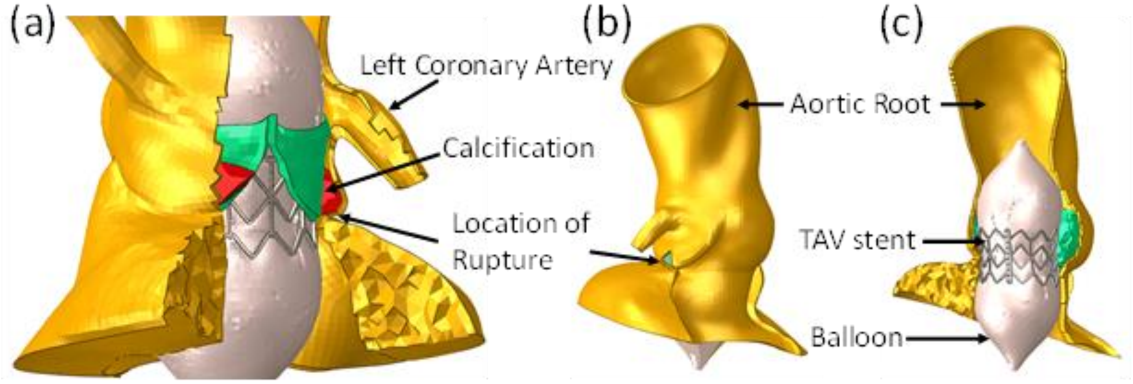

Figure 1.17 Aortic Annulus Rupture [81]: During a TAVR procedure, tearing and rupture occurred below the left main coronary artery. Simulation: (a) local and (b) full views of the deformed the aortic root and (c) balloon deployment show annulus tearing under the left coronary ostium due to dislodgement of calcification into the vulnerable part of the aortic sinus. (For illustration purposes, the yellow geometry in our finite element models represented the aortic root, the green geometry represented native aortic leaflets, the red geometry represented calcification, and the grey geometry represented the TAV stent.)

1.5.2.2 CFD Analysis

The inherent limitation of TAVI structural analyses is the lack of blood flow information; thus, several groups have used CFD to investigate the effects of TAVI on aortic hemodynamics. In Dwyer et al. [82] the effects of TAV degeneration on the device hemodynamic performance were assessed. The results suggest that shear stresses acting on the leaflets increase dramatically once a TAV has become stenosed; thus, stenosed TAVs should be carefully monitored to prevent catastrophic device failure. In a follow-up study, Dwyer et al. [83] quantified TAV migration forces in the noncalcified aortic root. The simulation results indicated that there was 6.01N retrograde force acting on the closed valve during diastole; and without aortic calcification to anchor the TAV in place, stent migration into the left ventricle was a major concern. Therefore, in order to extend the TAVI treatment method to patients with noncalcific aortic sufficiency, alternate device anchoring strategies must be explored. Sirois et al. [84] have investigated patient-specific hemodynamic changes following TAVI (Figure 1.18). The results show that while TAVI can reduce the peak transvalvular pressure drop, and increase the effective orifice area, it may also disturb flow in the vicinity of the sinuses and coronary arteries. Patient-specific analyses may be important for predicting whether sufficient cardiac output reaches the coronary arteries post-TAVI deployment.

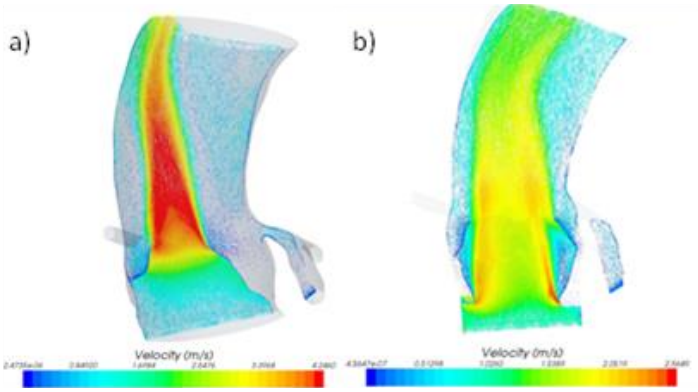

Figure 1.18 (a) Pre-deployment long section view of velocity distribution within the TAV at 1 ms after peak systole and the same view post-deployment at 7 ms after peak systole.

1.6 Review of the Biaxial Testing Method

Testing methods to characterize aortic valve tissue properties usually include uniaxial and biaxial studies of material properties of aortic valve, and pressure-inflation tests of structural properties of aortic roots. As shown the following chapters, biaxial testing method has been using the extensively to obtain aortic valve tissues mechanical properties, thus its testing setup and theories behind the data analysis are briefly summarized here.

Illustrated on Figure 1.19 is a typical setup of a biaxial testing device. Biaxial experiments are generally performed a square piece of planar soft tissue, with the sample of about 10-25 mm of lateral length. The specimen is mounted to the biaxial device in trampoline-like fashion using thin threads, which allows the edges to expand freely in the lateral direction. Testing is generally performed with the specimen completely immersed in phosphate buffered normal saline (pH 7.4) at room or body (37 °C) temperature. The central target region must be sufficiently small and located away from the outer edges to avoid the tethering effects. Thus, in the central target region the stress and strain field is generally considered homogeneous.

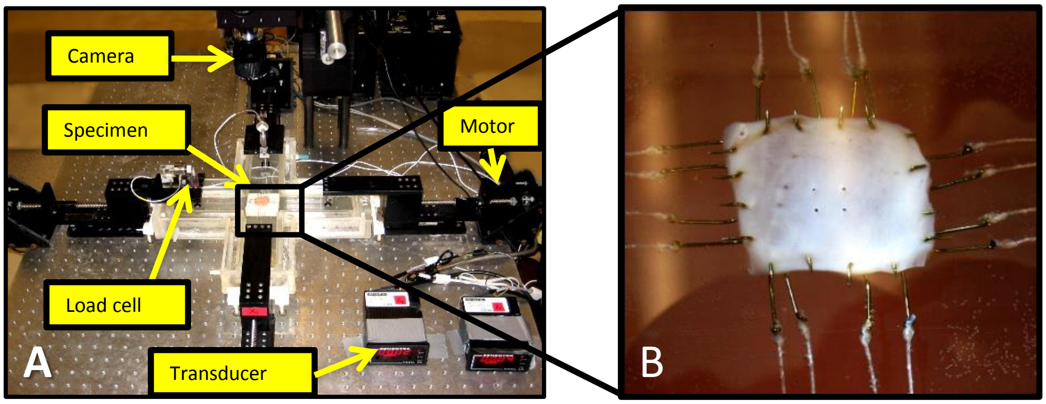

Figure 1.19 a) The biaxial testing system with an actual testing setup, showing the camera, the two load cells, the two signal conditioners and the four motors; b) A representative specimen is submerged in an appropriate physiologic solution, marked with four black graphite particles (optical markers for strain measurement) and attached to the device via four hooks at each side.

The following is a brief summary of the most important aspects of the kinematics of a biaxial mechanical test [85]. Consider deformation of membrane tissues under a biaxial stress state, including non-zero in-plane shear stresses. For this case, let Ω_0 and Ω be the (fixed) reference and deformed configurations of the continuous body, respectively. Consider the general mapping $\chi : \Omega_0 \to \mathbf{R}^3$, which transforms a material point $\mathbf{X} \in \Omega_0$ to a position $\mathbf{x} = \chi(\mathbf{X}) \in \Omega$ in the deformed configuration. For planar homogeneous deformations that occur during a biaxial test, this mapping reduces to

$$x_1 = \lambda_1 X_1 + \kappa_1 X_2, \quad x_2 = \lambda_2 X_2 + \kappa_2 X_1, \quad x_3 = \lambda_3 X_3 \tag{1.1}$$

where λ_i are the axial stretch ratios and κ_i measures of in-plane shear. λ_i and κ_i are also components of the deformation gradient tensor **F**, which for deformation described in eqn. 1.1 is $\mathbf{F} = \mathrm{Grad}(\mathbf{x})$ or

$$\mathbf{F} = \begin{bmatrix} \frac{\partial x_1}{\partial X_1} & \frac{\partial x_1}{\partial X_2} & \frac{\partial x_1}{\partial X_3} \\ \frac{\partial x_2}{\partial X_1} & \frac{\partial x_2}{\partial X_2} & \frac{\partial x_2}{\partial X_3} \\ \frac{\partial x_3}{\partial X_1} & \frac{\partial x_3}{\partial X_2} & \frac{\partial x_3}{\partial X_3} \end{bmatrix} = \begin{bmatrix} \lambda_1 & \kappa_1 & 0 \\ \kappa_2 & \lambda_2 & 0 \\ 0 & 0 & \lambda_3 \end{bmatrix} \tag{1.2}$$

where the out-of-plane stretch $\lambda_3 = h/H$ is the ratio of deformed (h) to the undeformed thickness (H) of specimen. **F** is a critical mathematical quantity since it completely describes the deformation state. Since soft tissues are composed primarily of water and have negligible permeability [86], they can be considered incompressible so that J=det**F**=1. From **F** the right Cauchy-Green deformation tensor is defined as $\mathbf{C}=\mathbf{F}^{\mathrm{T}}\cdot\mathbf{F}$, from which the components of the in-plane Green-Lagrange strain tensor $\mathbf{E} = ½ (\mathbf{C} - \mathbf{I})$, where **I** is the identity tensor. **E** is the most common finite strain measure in the soft tissue literature due to the simplicity of the constitutive formulations. In practice the components of **E** are computed more directly using:

$$\mathbf{E} = \frac{1}{2}(\mathbf{F}^{\mathrm{T}}\mathbf{F} - 1) = \frac{1}{2} \begin{bmatrix} \lambda_1^2 + k_2^2 - 1 & \lambda_1 k_1 + \lambda_2 k_2 & 0 \\ \lambda_1 k_1 + \lambda_2 k_2 & \lambda_2^2 + k_1^2 - 1 & 0 \\ 0 & 0 & \lambda_3^2 - 1 \end{bmatrix} \tag{1.3}$$

The components of **F** are determined optically to avoid any mechanical interference with the specimen.

As mentioned above, biaxial testing of biological tissues is performed using thin specimens (no more than ~3 mm, usually <1 mm) and acted on by only in-plane loads. A state of plane stress is thus assumed so that the components t_{i3} (i=1,2,3) of the Cauchy stress **t** (force/deformed area) are 0. During actual experiments one can directly measure only the initial specimen dimensions, so that the Lagrangian stresses **T** (force/unit original cross-sectional area) are used for convenience. The components of **T** are computed from the measured axial forces **P** using

$$T_{11}=\frac{P_1}{hL_2}, \quad T_{22}=\frac{P_2}{hL_1} \tag{1.4}$$

where h is the specimen thickness and L_i are the specimen lengths. Since experimentally applied loads are normal to the edges, $T_{12}=T_{21}=0$. The 2nd Piola-Kirchhoff stress tensor **S** is the most commonly utilized stress tensor for soft tissue constitutive theories, and is determined using $\mathbf{S}=\mathbf{T}\bullet\mathbf{F}^{-1}$. The Cauchy stress tensor **t** is determined using $\mathbf{t}=\mathbf{F}\bullet\mathbf{T}/J$, which in component form is given by (with $T_{12}=T_{21}=0$):

$$t_{11}=\lambda_1 T_{11},\ t_{22}=\lambda_2 T_{22},\ t_{12}=\kappa_1 T_{22},\ t_{21}=\kappa_2 T_{11} \tag{1.5}$$

In the case where there is negligible shear strain (i.e. $E_{12}\sim 0$), the normal components of the two stress tensors are related by:

$$S_{11} = T_{11}/\lambda_1,\ S_{22} = T_{22}/\lambda_2 \tag{1.6}$$

1.7 Review of Constitutive Models of Heart Valves

i) Linear elastic models. Early attempts to describe valve tissue properties relied on the linear elastic material model, following the generalized Hooke's law [87, 88]

$$\sigma_{ij} = C_{ijkl}\epsilon_{kl} \tag{1.7}$$

where σ_{ij} is the stress tensor, ϵ_{kl} is the strain tensor and C_{ijkl} is the fourth order elasticity tensor. Linear elastic models are appropriate when the stress-strain relationship is indeed linear, and are typically restricted to relatively small deformations. Linear elastic material properties were chosen for various reasons [89-91], but mainly to simplify the simulation process in order to achieve numerical convergence in FE simulation solutions. Over the physiological range of pressures, valve tissues have been shown to exhibit a relatively linear stress-strain relationship [92]. However, for a FE simulation of valve deformation from the undeformed state to a deformed state, the valve material response is clearly nonlinear and the use of nonlinear material models is essential for any realistic valve simulations.

ii) Fung-elastic model. The Green-strain based exponential model proposed by Fung [86] is probably the most commonly used hyperelastic model for characterizing the mechanical response of soft tissues [86, 93]. A two-dimensional Fung-type strain energy function W can be expressed as:

$$W = \frac{c}{2}\left[e^{Q} - 1\right], \qquad (1.8)$$

$$Q = A_1 E_{11}^2 + A_2 E_{22}^2 + 2A_3 E_{11} E_{22} + A_4 E_{12}^2 + 2A_5 E_{11} E_{22} + 2A_6 E_{22} E_{12}$$

where c and Ai are material constants, E is the Green strain tensor. Note that Eqn. (1.8) has other variants that could be easily treated as a subset or expansion of this model [94]. Eqn. (1.8) is often used to model planar biaxial mechanical responses of valve tissues [95] and should be implemented with plane stress elements, such as shell or membrane elements. One problem with Eqn. (1.8) is that the transverse shear stiffness in the 13 and 23 directions are undetermined due to the lack transmural response definitions in this model. As shown by Sun et al. [94], valve peak stress is insensitive to change of TSS values for the valve closure simulation. However, to simulate valve opening, the tissue bending response is critical, and without accurate transverse shear stiffness values, the use of Eqn. (1.8) may give inaccurate results. The details on the FE implementation of Eqn. (1.8) can be found in Sun and Sacks [94]. The 3D Fung model has not been widely used to model valve functions. Labrosse et al. [96, 97] has successfully utilized a 3D Fung model in simulation of native AV deformation.

iii) Strain invariant-based fiber-reinforced hyperelastic model. Weiss et al. [98] and Holzapfel [99] presented a computational framework to implement strain invariant-based models that can accommodate the effects of one or two families of elastic fibers. To use this class of models, typically, the valve tissues are assumed to be composed of a matrix material with two families of imbedded fibers, each of which with a preferred direction. The deviatoric strain invariant $\overline{I_1}$ is used to describe the matrix material; and $\overline{I_{4i}}$ is used to describe the properties of the fiber families. One example of such models proposed by Holzapfel et al. [99] can be expressed as

$$W=C_{10}\left(\overline{I_1}-3\right)+\frac{k_1}{2k_2}\sum_{i=1}^{2}\left[\exp\left\{k_2\left[\kappa\overline{I_1}+\left(1-3\kappa\right)\overline{I_{4i}}-1\right]^2\right\}-1\right]+\frac{1}{D}\left(J-1\right)^2, \; i=1,2 \qquad (1.9)$$

where, C_{10}, k_1, k_2 and D are material constants. Particularly, C_{10} describes the matrix material and D enforces near incompressibility. In addition, a dispersion parameter, κ, is used to describe the distribution of the fiber orientation. Local coordinate systems should be defined for each leaflet to include fiber orientations. There are several variations of the model that have been applied to heart valve simulations. Prot et al. [100] implemented the Holzapfel material model into the analysis of healthy and pathological human mitral valves. Similarly, in the study by Stevanella et al. [101], the MV dynamics were simulated where leaflet properties were characterized through a transversely isotropic model proposed by May-Newman and Yin [102], while the same material model was used by Conti et al. [103] and Auricchio et al. [104] to simulate AV biomechanics.

1.8 Motivation of the Study

The many significant adverse TAVI complications emphasize the importance of improved pre-procedural planning methods to improve patient outcomes. Many of these complications can be explained using the biomechanics; thus, an in-depth understanding of the biomechanical interactions, such as the radial and tangential forces between the TAVI device and the native tissue, is critical to the success of TAVI. Additionally, each

TAV valve has specific characteristics and different aortic anatomic requirements. In consequence, pre-procedural planning plays an essential task for correct sizing, proper device and patients' selection, and decision-making on implantation strategies. To help clinicians evaluate complicated, high-risk cases with potentials for aforementioned complications, I proposed to examine the biomechanical interaction between the native tissue and prosthesis during TAVI stent deployment using patient-specific FE simulations.

The overall goal of this research was to investigate the biomechanics involved in the TAVI stent deployment process using a combined experimental and computational approach. Specifically, the objectives of this thesis are:

i) To reconstruct patient-specific aortic root geometry and obtain TAVI-relevant measurements using the CT scans

ii) To characterize the aged human aortic root tissue material properties using biaxial and uniaxial testing

iii) To simulate balloon-expandable stent deployment process during TAVI procedure using FE method

vi) To evaluate the potential of the clinical adverse events associated with TAV expansion using biomechanical characteristics of the FE simulation results

Successful completion of the proposed work could generate a computational methodology to model TAVI stent deployment, which could provide useful information for pre-procedural planning of TAVI.

CHAPTER 2

DIMENSIONAL ANALYSIS OF AORTIC ROOT GEOMETRY

Accurate measurement of anatomical characteristics of the aortic root is needed for pre-procedural planning of many valve procedures and development of novel valve intervention devices. Dimensional measurement of the aortic root is usually performed on 2-dimensional (2D) images, rather than on a full 3-dimensional (3D) geometric model.

In this chapter, full 3D aortic root geometric models, reconstructed from clinical multi-slice computed tomography (MSCT) scans during diastole, were used to perform dimensional analysis of the aortic root geometry of 94 patients. Thirty-two landmark points were placed on anatomic feature locations of each aortic root model for the measurement of aortic root dimensions. Diameters of the annulus, sinus of Valsalva (SOV), sino-tubular junction, and ascending aorta were compared with measurements obtained from 2D MSCT images in short axes. Additionally, the spatial distribution of the left coronary ostium (CO) within the left coronary sinus was determined due to its significance in transcatheter aortic valve implantation.

Overall, the results of this chapter suggested that similar results could be obtained using the 3D models compared to 2D MSCT images. Since anatomical features of the aortic root can be easily identified on a full 3D geometric model, more complete information could be obtained. The results of this chapter were published in [45].

2.1 Introduction

To achieve a successful surgical operation and catheter intervention in patients with aortic root diseases, accurate anatomical information of the aortic root and surrounding structures is essential. A quantitative understanding of the aortic root geometry is also necessary for designing innovative interventional prosthesis and for constructing numerical models, such as a finite element (FE) model and a computational fluid dynamics model, to evaluate biomechanical behaviors of aortic tissues and host tissue-device interactions during treatment. In recent years, multi-slice computed tomography (MSCT) has been used to generate accurate measurement of aortic dimensions for pre-procedural planning of many valve procedures including valve-sparing aortic root repair, transcatheter aortic valve implantation (TAVI), as well as treatment of coronary artery or other aortic diseases [3, 18, 22, 105-108].

Previous studies [105, 109, 110] have showed that clinical MSCT could be used to measure aortic root anatomic geometries with greater accuracy than 2-dimensional (2D) echocardiography or angiography. Although the MSCT data are collected in a 3-dimensional (3D) volumetric format, the geometric measurements of the aortic root are currently determined from a 2D slice plane, often in the coronal or sagittal views. Since the aortic root is an asymmetric, non-uniform 3D structure (e.g., the three aortic sinuses have different sizes), some anatomic dimensions may not be fully measurable on a 2D cross-sectional image. In this chapter, we aimed to explore a new approach to investigate anatomic dimensions of the aortic root using full 3D aortic valve geometric models extracted from clinical 64-slice CT scans. We attempted to establish the feasibility of using the 3D models for such dimensional measurements, i.e., similar results could be obtained using the 3D models compared to 2D MSCT images. Moreover, since anatomical features of the aortic root can be easily identified on a full 3D geometric model, more complete information than 2D measurements may be obtained.

2.2 Methods

2.2.1 Study Population

Full phase cardiac MSCT scans were collected from patients at Hartford Hospital (Hartford, CT) between 2005 and 2009. Institutional Review Broad approval to review de-identified images was obtained for this study. All patients underwent MSCT scans because of suspected coronary artery disease. The exam images were used for retrospective analysis in this study. Patients with severe aortic stenosis and bicuspid aortic valve were not included in this study to simplify the data comparison between the 3D method and the conventional 2D measurements.

2.2.2 MSCT Image Acquisition

The MSCT examination was performed on a GE LightSpeed 64-channel volume computed tomography scanner. Prior to MSCT angiography, prospective calcium score acquisition was performed (collimation 25 × 3.0 mm, rotation time 375 ms, voltage 120 kV, and tube current 500 mA). The temporal window was set at 75% interval after the R wave for electrocardiographically (ECG) triggered prospective reconstruction.

For MSCT coronary angiography, a collimation of 25-30 × 0.625 mm and a rotation time of 375 ms were used resulting in a temporal resolution of less than 200 ms. The tube current modulation was automated to a maximum of 800 mA at 120 kV. Images were obtained with helical scanning and ECG gating. A timing bolus of 20 cc bolus of Ultravist 370 contrast (Bayer Healthcare Pharmaceuticals, NJ) was administered and followed by a 20 cc bolus of normal saline. A 1 s axial scan with a 1 s inter scan delay with a region of interest at the level of the ascending aorta (AA) was obtained until contrast density detected. 80 cc of Ultravist 370 contrast was administered via the antecubital vein at a flow rate of 5.0 ml per second using a Medrad Stellant dual headed injector (Medrad, Warrendale, PA). Data acquisition was obtained during an inspiratory breath hold of approximately 6-8 s with ECG gating. In general, a total of 2000 slices of images with thickness of 0.625 mm were collected for the whole cardiac cycle.

2.2.3 Diameter Measurement on 2D MSCT Images

MSCT scans were loaded into a custom-made image processing program, written with C++ and the Visualization Toolkit library (VTK) [111]. Full 3D rotation of the CT volume within the program allowed a 2D slice plane to be cast through the volume to create an oblique view in any direction. Diameters of aortic annulus, the sinus of Valsalva (SOV), the sino-tubular junction (STJ), and the AA were measured at the diastole phase using oblique short-axis views. The aortic valve annulus was defined at the lowest level of the insertion of the valve cusps into the aortic root [112], where maximum and minimum annulus diameters were measured. The diameter of the SOV was determined from measurements extending from the middle of the non-coronary sinus (NCS) cusp to the opposite commissure [112]. The STJ diameter was measured at the junction of the sinuses and tubular portion of the AA [112]. The AA diameter was measured approximately 5 mm above the STJ.

2.2.4 Diameter Measurement on 3D Aortic Root Models

The same MSCT scans were imported into the Mimics software (Materialise, Leuven, Belgium) for the 3D reconstruction and evaluated using a window width of 950 and -50 Hounsfield units in Mimics. The interior surfaces of the aortic root were automatically identified and separated from the rest of the chest images to create a 3D representation. FE surface mesh was generated for the 3D aortic root model using the HyperMesh (Altair Engineering, Inc., MI) software.

Thirty-two landmark points (Figure 2.1) were selected from the model to identify the anatomic regions of the aortic annulus, the SOV, the STJ, the AA, and the coronary ostia (CO). For the aortic annulus, one point was created at the nadir of the bulging surface of each sinus. The three nadirs were used to define the annulus plane, on which another point was selected approximately in the middle of two sinuses. A smooth curve was generated using these six points to represent the perimeter of the aortic annulus

(Figure 2.1 and Figure 2.2 a&b). For the SOV, one point was created at the zenith of each sinus surface. Similar to the annulus, the three zeniths were used to define the SOV plane. Due to the cloverleaf geometry of the SOV, three more points were selected between two zeniths, as shown in Figure 2.1 & 2.2. Thus, a total of 12 landmark points were used to define the perimeter of the SOV. The SOV perimeter was also determined by the largest circle through the cloverleaf geometry and the smallest circle through the inter-sinus trigonal region (Figure 2.2 c&d). The STJ plane was defined at the superior border of the sinuses (Figure 2.3) and the AA was measured approximately 5 mm above the STJ (Figure 2.3) using 6 landmarks, similar to the aortic annulus.

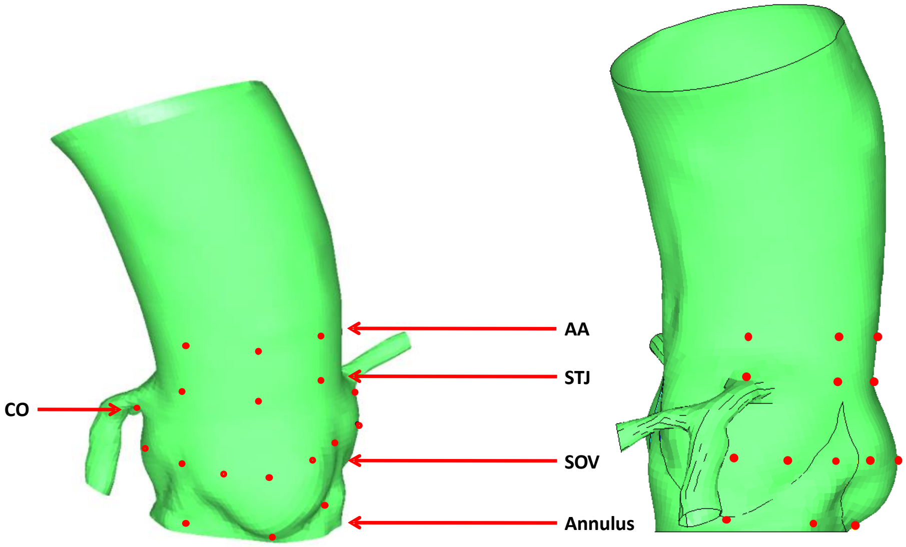

Figure 2.1 Finite element model of the aortic root and the landmark points created for each height level, ascending aorta (AA), sino-tubular junction (STJ), sinus of Valsalva (SOV), aortic annulus, and coronary ostia (CO) in the (a) front view and (b) in the side view.

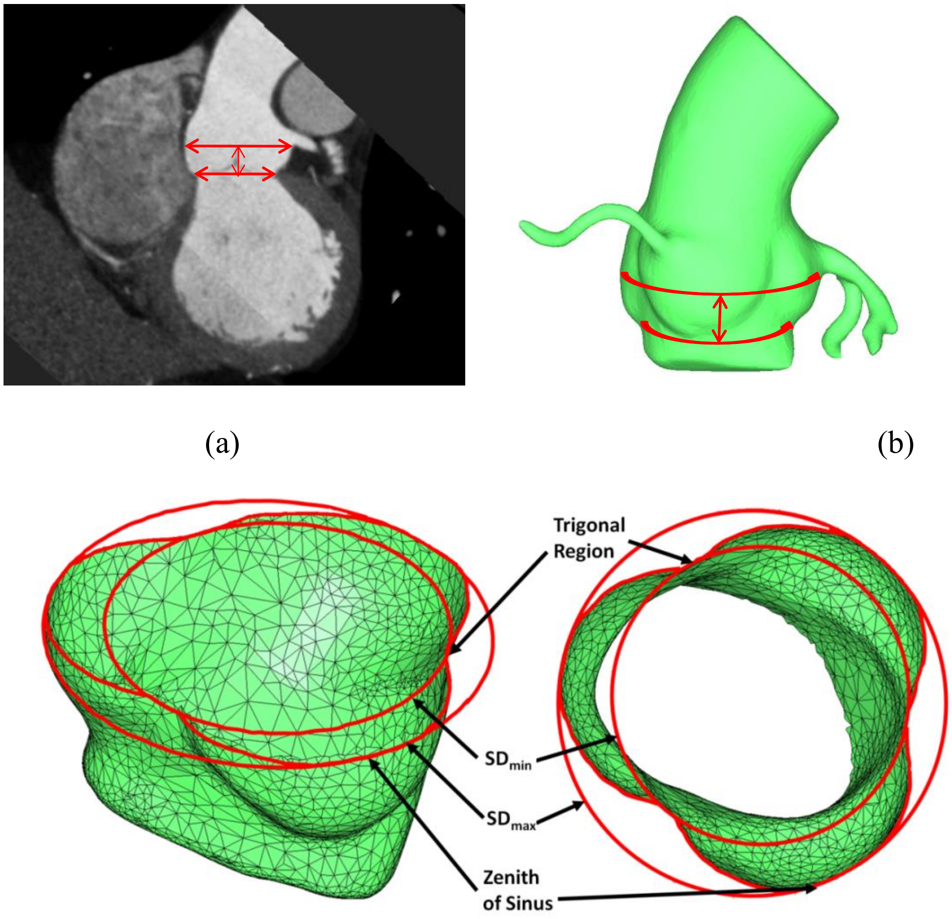

(a) (b)

(c) (d)

Figure 2.2 The measurement of the sinus of Valsalva (SOV) (a) the maximum diameter of the SOV in the coronal view (b) diameter measurement taken from the finite element model. Additionally, the distance between the aortic annulus and the level of the maximum diameter of the SOV was measured. (c) 3D perimeter measurements on the cross-section of the SOV in the front view and (d) in the top view.

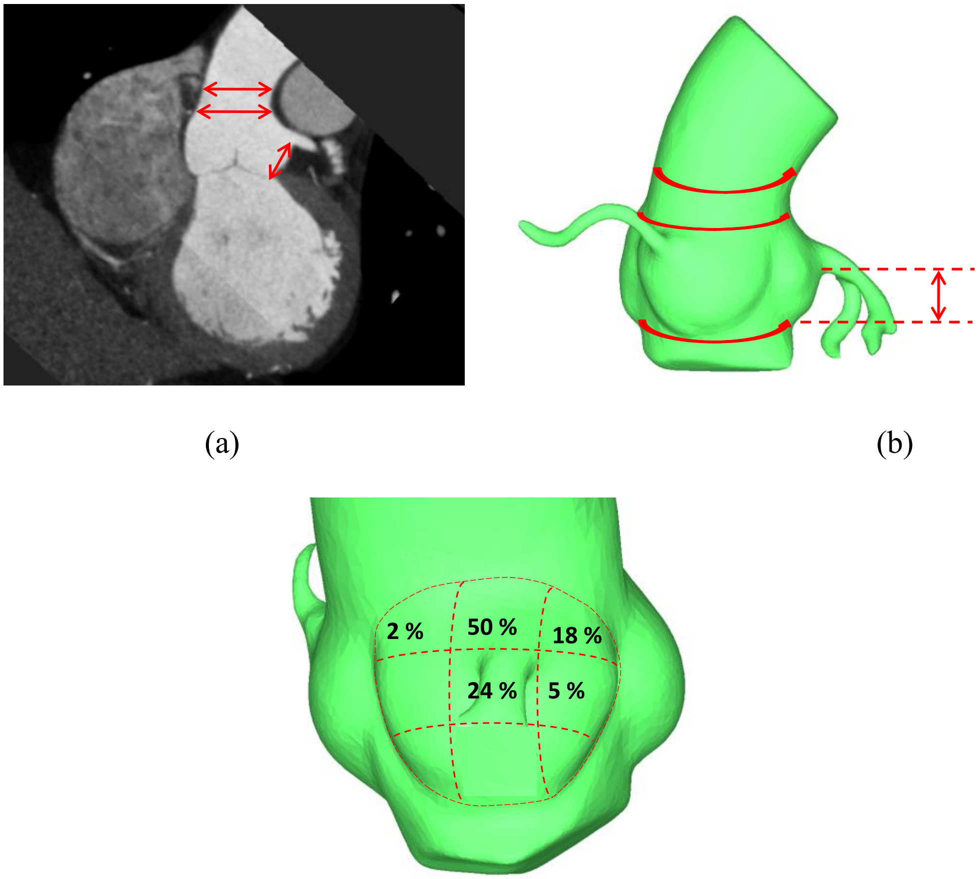
(a)

(b)

(c)

Figure 2.3 The measurement of the ascending aorta (AA), sino-tubular junction (STJ), and coronary ostia (CO) (a) the maximum diameter of the STJ, AA, and the distance between the CO and aortic annulus were examined in the 2D coronal view (b) STJ and AA diameter measurement taken from the finite element model. Also, the projected distance between the CO and the aortic annulus plane was measured. (c) The spatial location of left CO with respect to the left aortic sinus.

The measurements obtained from the 3D aortic root models include: a) 2D diameters of the aortic annulus, SOV, STJ, and AA during diastole, which were directly measured on the 3D aortic root models using the anatomical planes defined above in order to compare with the 2D MSCT measurements. b) 3D perimeter-derived aortic root diameters, which were calculated by dividing the 3D perimeter measurements by the value of π. c) the area of the aortic annulus, which was determined by creating a surface and calculating the surface area of the orifice using HyperMesh.

2.2.5 Height Measurement on 3D Aortic Root Models

The measurement of the distance in the axial direction was conducted by projecting the landmark points representing each height level to the aortic annulus plane. Of note, the planes of SOV, STJ and AA may not be parallel, or co-axial, to the annulus plane, thus the distance was calculated using the mean projected distances of the landmarks to the annulus plane. The height of the CO was measured as the axial (vertical) distance from the inferior border (a landmark point) of the coronary artery to the aortic annulus plane (Figure 2.3). The height of the sinus was evaluated as the axial distance from the STJ to the aortic annulus plane.

2.2.6 Spatial Location of Left CO

To determine the spatial location of left CO with respect to the left coronary sinus (LCS), we divided the LCS into 9 regions defined by 3 evenly spaced arc length distances along the longitudinal direction of the sinus and 3 evenly spaced arc length distances in circumferential direction. We counted the number of the left CO within each region to obtain its spatial probability distribution, which is important for prosthesis design and pre-procedural planning, but was not reported in the literature.

2.2.7 Data Analysis

Statistical analysis was conducted using Minitab 15 (Minitab Inc., PA). Normality tests indicated that all measurement results followed normal distribution. All variables were thus reported as mean values with standard deviations. Linear regression analysis and Bland-Altman plots were used to compare the aortic root measurements by 2D MSCT images and 3D FE models. Paired t tests and Pearson correlations were used to compare the difference in annulus diameters obtained from 2D MSCT images and 3D models. Analysis of Variance (ANOVA) tests with Tukey comparison were performed to determine the significant difference between various height levels. Significance was determined by a p-value of 0.05 or less.

Intra-observer and inter-observer variability of annulus measurements were evaluated by absolute difference between measurements. For intra-observer variability analysis, fifteen patients were randomly selected from our dataset and the aortic annulus diameter was measured twice for each patient by one observer. For inter-observer variability analysis, the same fifteen patients were used and the aortic annulus diameter was measured for each patient by 2 observers blind to clinical information.

2.3 Results

2.3.1 Patient Information

A total of 94 patients (55 males and 39 females) were included in this study. The average age of the patients was 56 ± 12 years. The age distribution of the study population was such that there were 28 patients in each of three age groups (< 50, 50 - 60, and 60 - 70), and 10 patients in age 70 + group.

2.3.2 Aortic Root Diameters by 2D MSCT and 3D FE Models

Comparisons of aortic root diameters directly measured in short axes using 2D MSCT images and 3D models were shown in Table 2.1, and Figure 2.4. Pearson correlation tests (Table 2.1) and linear regression analysis (Figure 2.4) indicated that in general there was very good agreement between all variables by the two methods. The results of paired t test (Table 2.1) and Bland-Altman analysis (Figure 2.4) showed that difference in the mean maximum annulus diameter and mean SOV diameter between the two methods was slightly larger than the other measurements.

Table 2.1 Comparisons of aortic root diameters between 2D MSCT and 3D FE models.

Aortic Root Characteristics	**2D MSCT (mm)**	**3D Model (mm)**	**r Value**	**Bias (mm)**	**p Value**
Max. Annulus Diameter	27.1 ± 3.0	26.9 ± 3.0	0.94	0.24	0.035
Min. Annulus Diameter	21.8 ± 2.5	21.8 ± 2.7	0.93	0.08	0.466
Average Annulus Diameter	24.5 ± 2.6	24.3 ± 2.8	0.96	0.16	0.061
SOV Diameter	33.0 ± 4.1	32.7 ± 3.7	0.95	0.27	0.051
STJ Diameter	28.8 ± 3.8	28.7 ± 3.3	0.94	0.08	0.559
AA Diameter	29.7 ± 3.9	29.9 ± 3.6	0.93	-0.18	0.226

Footnote: r value is coefficient of correlation, sinus of Valsalva (SOV), sino-tubular junction (STJ), ascending aorta (AA)

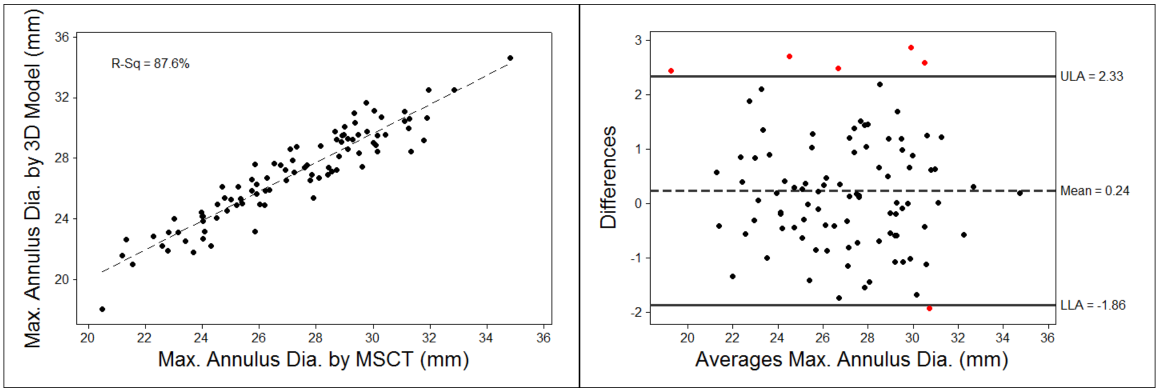
R-Sq = 87.6%
Max. Annulus Dia. by 3D Model (mm)
Max. Annulus Dia. by MSCT (mm)
20 22 24 26 28 30 32 34 36
20 24 28 32 36
Differences
Averages Max. Annulus Dia. (mm)
ULA = 2.33
Mean = 0.24
LLA = -1.86
-2 -1 0 1 2 3

(a) (b)

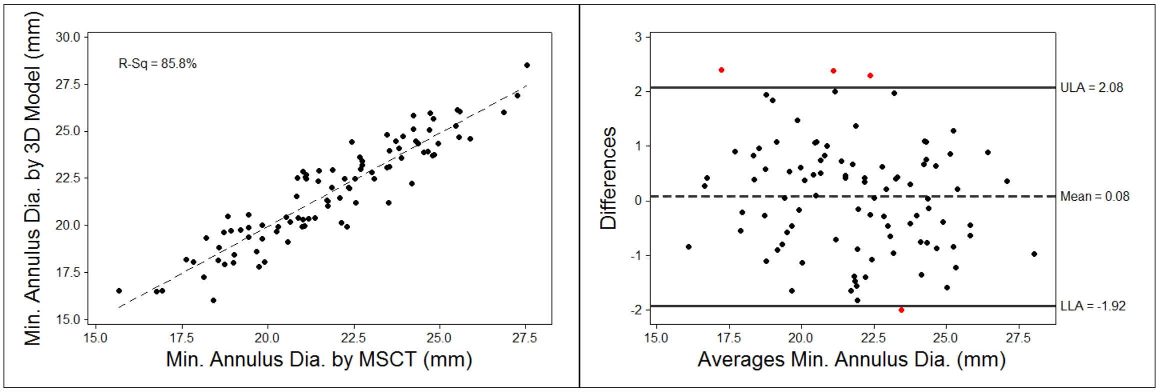
R-Sq = 85.8%
Min. Annulus Dia. by 3D Model (mm)
Min. Annulus Dia. by MSCT (mm)
15.0 17.5 20.0 22.5 25.0 27.5 30.0
Differences
Averages Min. Annulus Dia. (mm)
ULA = 2.08
Mean = 0.08
LLA = -1.92
-2 -1 0 1 2 3

(c) (d)

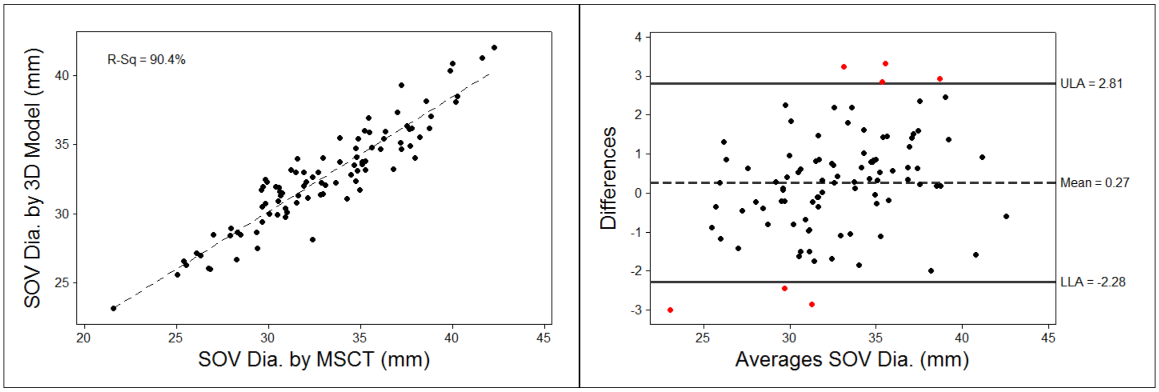
R-Sq = 90.4%
SOV Dia. by 3D Model (mm)
SOV Dia. by MSCT (mm)
20 25 30 35 40 45
Differences
Averages SOV Dia. (mm)
ULA = 2.81
Mean = 0.27
LLA = -2.28
-3 -2 -1 0 1 2 3 4

(e) (f)

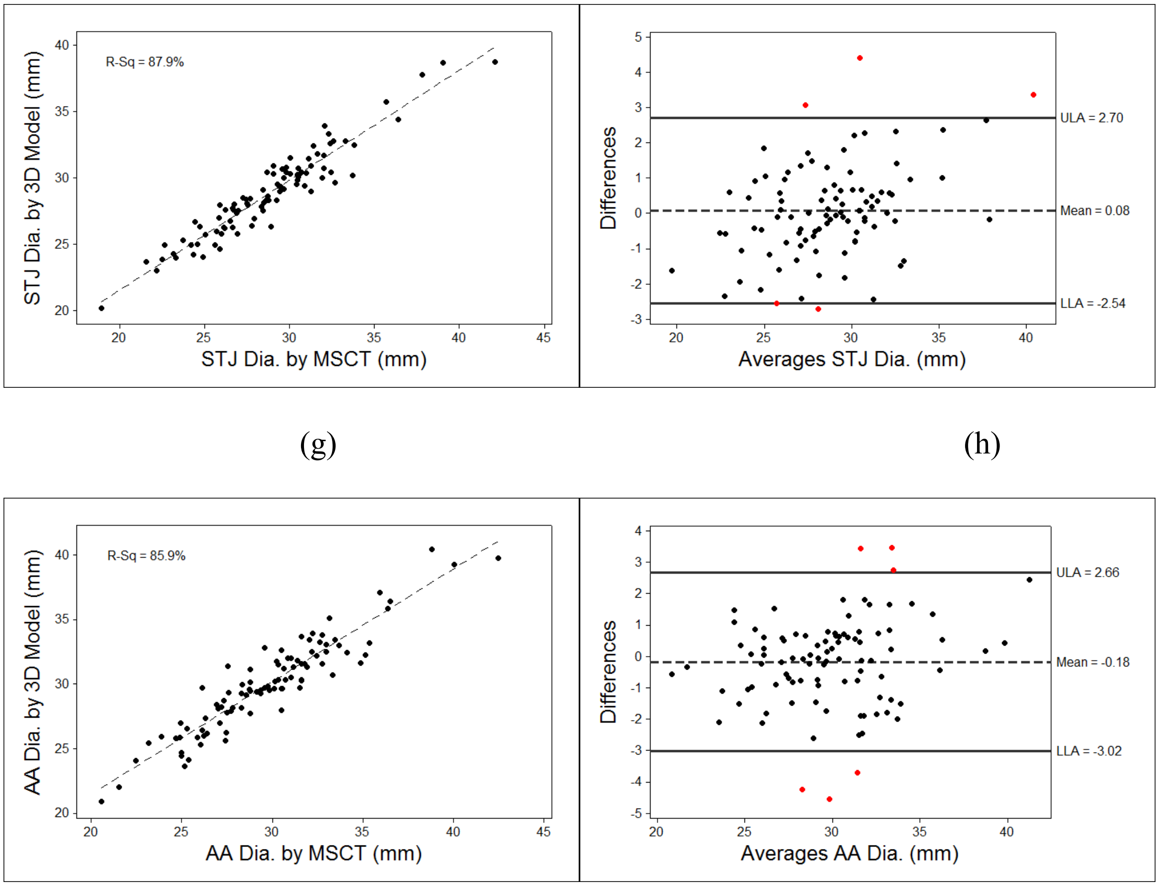

(g) (h)

(i) (j)

Figure 2.4 Correlations of aortic root measurements in short axes between 2D MSCT and 3D FE models by linear regression analysis and Bland-Altman analysis: (a) and (b) maximum aortic annulus diameter, (c) and (d) minimum aortic annulus diameter, (e) and (f) the sinus of Valsalva (SOV) diameter, (g) and (h) the sino-tubular junction (STJ), and (i) and (j) the ascending aorta (AA). The dash line in linear regression plots indicates the trendline. The middle dash line in Bland-Altman plots represents the mean, the upper line represents + 2 SDs, and the lower line represents - 2 SDs.

The difference between maximum and minimum aortic annulus diameters by 3D models and 2D MSCT was 5.1 mm and 5.3 mm respectively. Paired t test results showed that the maximum and minimum annulus diameters were significantly different from each other ($p < 0.001$), which confirmed an oval shape of the aortic annulus [110]. Additionally, intra-observer and inter-observer variability of the annulus diameter measurements using 3D models was 0.5 ± 0.8 mm and 0.4 ± 0.8 mm by examining 15 patients. It should be noted that observed findings in this chapter cannot be generalized to other institutions. Each institution has to assess its own intra/inter-observer variability.

2.3.3 Aortic Root Diameters Derived Using Perimeter Measurements on 3D Models

Aortic annulus diameters calculated from perimeters of 3D models as well as relevant studies in the literature were listed in Table 2.2. The 3D perimeter-derived aortic annulus diameter was 24.9 ± 2.6, which was slightly larger than the average annulus diameter of the maximum and minimum axes (24.3 ± 2.8 mm) (Figure 2.5a&b). The average annulus sizes are 24.9 mm, 24.8 mm, and 25.6 mm for < 50, 50 - 60, and 60 - 70 age groups respectively.

Table 2.2 Additional measurements of the aortic root geometry obtained in the present study and in the literature.

Aortic Root Characteristics	**Present Study**	**Tops [46]**	**Stolzmann [52]**	**Akhtar [113]**	**Messika-Zeitoun [114]**	**Schultz [115]**	**Delgado [116, 117]**
	(n = 94)	**(n = 150)**	**(n = 100)**	**(n = 25)**	**(n = 45)**	**(n = 75)**	**(n = 90)**
Diameter (mm)							
Annulus	24.9 ± 2.6 *	24.9 ± 2.6	23.0 ± 3.1	27.2 ± 4.0	24.6 ± 2.4	24.1 ± 2.6	25.5 ± 2.5
SOV	34.8 ± 4.3 *	32.3 ± 3.9	33.5 ± 4.2	36.7 ± 5.3	N/A	N/A	33.9 ± 3.3
STJ	28.8 ± 3.3 *	28.1 ± 3.1	25.9 ± 3.3	28.2 ± 4.7	N/A	N/A	29.1 ± 3.2
AA	30.0 ± 3.6 *	N/A	N/A	32.2 ± 5.8	N/A	N/A	N/A
Height (mm)							
NCS	23.4 ± 3.0	20.3 ± 3.1	N/A	21.4 ± 2.4	N/A	N/A	22.2 ± 3.2
LCS	22.2 ± 2.6		19.5 ± 2.9		N/A	N/A	N/A
RCS	22.6 ± 3.2		19.0 ± 2.9		N/A	N/A	N/A
Left CO	13.6 ± 2.9	14.4 ± 2.8	14.9 ± 3.2	15.7 ± 2.6	N/A	N/A	17.1 ± 2.5
Right CO	16.9 ± 3.1	17.2 ± 3.3	16.8 ± 3.6	15.6 ± 2.7	N/A	N/A	18.7 ± 2.8
SOV	15.9 ± 2.0	17.2 ± 2.7	N/A	N/A	N/A	N/A	11.3 ± 1.7
Annulus perimeter (mm)	78.2 ± 8.2	N/A	N/A	N/A	N/A	76.3 ± 6.6	N/A
SOV perimeter (mm)	109.3 ± 13.5	N/A	N/A	N/A	N/A	N/A	N/A
Annulus area (mm^2)	476.3 ± 98.7	N/A	N/A	670.0 ± 170.0	N/A	N/A	N/A

Footnote: ascending aorta (AA), sino-tubular junction (STJ), sinus of Valsalva (SOV), coronary ostia (CO), non-coronary sinus (NCS), left coronary sinus (LCS), right coronary sinus (RCS).

*Data were calculated from the perimeters of 3D measurement divided by π.

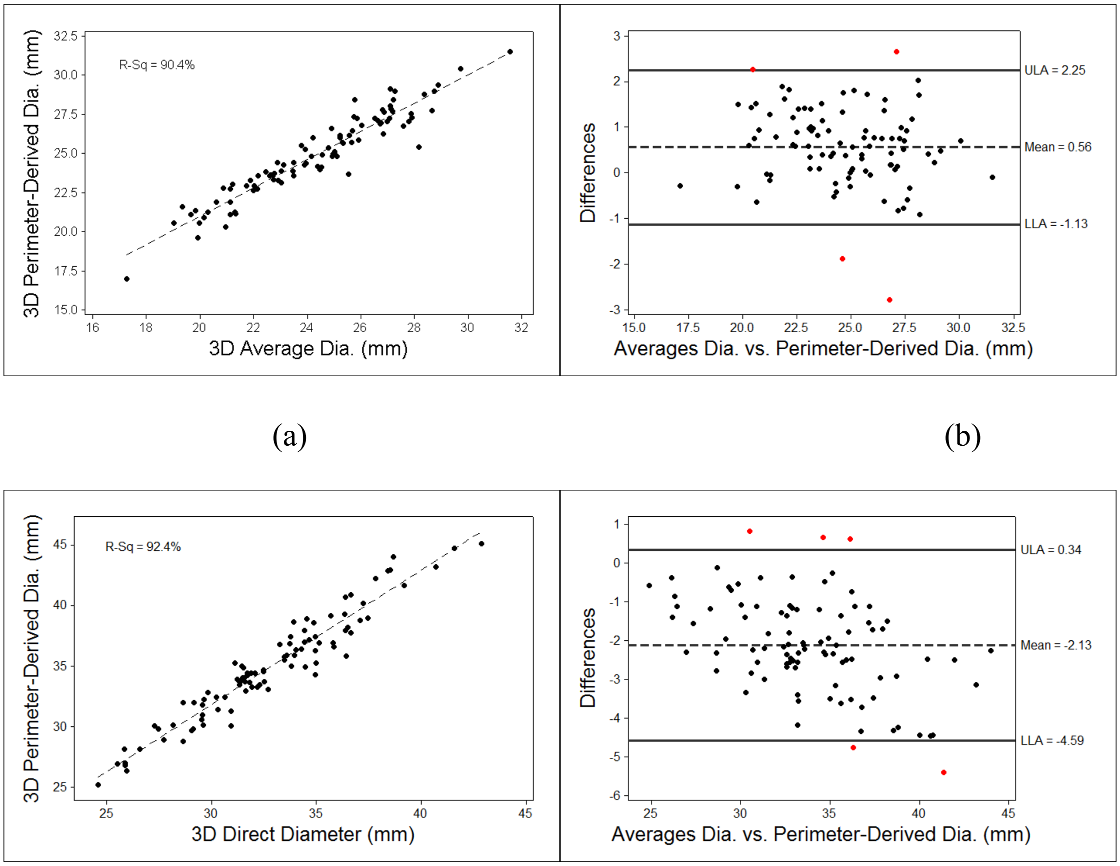

(a) (b)

(c) (d)

Figure 2.5 Correlations between the average aortic annulus diameter of maximum and minimum axes using 3D models and perimeter-derived aortic annulus diameter by (a) linear regression analysis and (b) Bland-Altman analysis. Correlations between the direct SOV diameter measurement using 3D models and perimeter-derived SOV diameter by (c) linear regression analysis and (d) Bland-Altman analysis. The dash line in linear regression plots indicates the trendline. The middle dash line in Bland-Altman plots represents the mean, the upper line represents + 2 SDs, and the lower line represents - 2 SDs.

In this study, the mean 3D perimeter-derived SOV diameter was 34.8 mm, which was larger than the short axis view measurement (32.7 mm) on 3D models (Figure 2.5c&d). The maximum (SDmax) and minimum (SDmin) diameters of the SOV (Figure 2.2c&d) were 36.7 ± 4.6 mm, 28.1 ± 3.1 mm, and 3D perimeter-derived STJ and AA diameters were 28.8 ± 3.3 mm and 30.0 ± 3.6 mm, respectively. One-way ANOVA test results showed that the maximum diameter (SDmax) of the SOV was significantly ($p < 0.001$) larger than those of the STJ and AA. Note that the cloverleaf geometry of the SOV was considered for the measuring of the SOV perimeter and diameter (Figure 2.2c and 2.2d).

2.3.4 CO Height and Sinus Height on 3D Models

Measuring from full 3D models, the mean heights of the NCS, LCS and the right coronary sinus (RCS) were 23.4 ± 3.0 mm, 22.2 ± 2.6 mm, and 22.6 ± 3.2 mm respectively. One-way ANOVA test results suggested that there was no statistically significant difference in height between sinuses ($p = 0.385$). In our patient cohort, 86% have a lower height of the left CO than that of the right CO. The mean heights of the left and right COs were 13.6 ± 2.9 mm and 16.9 ± 3.1 mm with ranges from 7.2 mm to 22.9 mm and from 10.2 mm to 24.9 mm respectively. Paired *t* test results showed that there was a significant difference ($p < 0.001$) in the distance from the annulus between left and right CO.

2.3.5 Spatial Location of Left CO

The spatial location of left CO with respect to the left aortic sinus was assessed using the 3D aortic root models. As shown in Figure 2.3c, the left CO was predominantly located in the upper right region (4 combined areas in the figure) of the LCS, which was adjacent to the NCS. In approximately 20-25 % of the patients, the locations of the CO were close to the commissures. For those patients, the possibility of the occlusion of the CO during the TAVI intervention might be higher.

2.4 Discussion

Imaging modalities such as 3D echocardiography and 2D MSCT scans, which allow a full 3D rendering of anatomic geometries, are being increasingly utilized as diagnostic tools. In this chapter, we presented, to our knowledge, the first dimensional analysis of the aortic root using full 3D models reconstructed from clinical 64-slice CT scans.

2.4.1 Comparisons of Aortic Root Diameter Measurements by 2D MSCT and 3D FE Models

Overall, the comparisons between 2D MSCT and 3D model suggested that the mean measurements for all variables had good correlations (Table 2.1 and Figure 2.4). However, Bland-Altman analysis showed the mean difference between the two methods ranged from 0.08 mm to 0.27 mm and the width of 95 % confidence interval was approximately 5 mm. The main source of bias between the two methods could be the orientation and position of the cutting planes chosen for aortic root measurements. The advantage of using 3D models was that anatomical features of the aortic root, such as the annulus, the prominent points of the sinuses, and the boundaries of the CO and sinuses, can be easily identified on a full 3D geometric model. This feature could help locate the cutting plane for a specific aortic root measurement.

2.4.2 Aortic Root Diameters Derived Using Perimeter Measurements on 3D Models

It is now well accepted that the aortic annulus in diastole is of an oval shape instead of a circular one [38]. However, the current TAVI devices, i.e., the Edwards SAPIEN valve and the Medtronic CoreValve devices, have a symmetric circular shape. Thus, for the TAVI sizing, the perimeter of the circular stent should match the perimeter of the elliptical annulus. To estimate the annulus perimeter, the averaged diameter from the coronal and sagittal views or the maximum and minimum axes was often used [115]. This study found that the 3D perimeter-derived aortic annulus diameter was slightly larger (0.56 mm) than the average annulus diameter of the maximum and minimum axes (Figure 2.5a&b). Even though the choice of perimeter vs. diameter in TAVI sizing remains speculative, the perimeter measured in 3D models should, in theory, provide more accurate and complete geometric measurements than the diameter measurements on 2D slice planes.

In this study, we observed several differences in the diameter of SOV between the results of our study and those of other studies. The differences in 3D and 2D measurement methods may explain these discrepancies. The long axis or short axis 2D view of the aortic root is usually used to measure the maximum diameter of SOV [110, 112]. However, as the three sinuses are about 120 degrees apart from each other, the long-axis 2D view plane can only cut through one sinus (see Fig. 3 of Tops et al. [110]). Therefore, a single 2D measurement of the diameter of the SOV in a long-axis view plane may be inaccurate and misleading. In addition, the largest diameter of the SOV in a short-axis 2D view must be interpolated from the review of multiple adjacent planes proximal and distal to the actual plane of the largest diameter. In our study, however, we can measure the SOV perimeter as well as maximum (SDmax) and minimum (SDmin) SOV diameters directly in 3D with the consideration of the cloverleaf geometry of the SOV (Figure 2.2c and 2.2d). In addition, it was observed that the shape of the STJ and AA was almost circular, which could explain the similarity between the current diameter measurements and those obtained in the 2D coronal view (Table 2.2).

For CO height measurement, Tops et al. [110] reported that the mean distances between the left and right COs and the annulus were 14.4 mm and 17.2 mm, respectively, which were slightly larger than our measurements. A wide variation in distance was also found in the study by Tops et al. [110], ranging from 7.1 to 22.7 mm. The left and right CO heights obtained in this study (Table 2.2) were lower than the values reported in other studies that used 2D MSCT techniques [52, 110, 112]. This discrepancy could be due to the fact that, compared to those studies where a single 2D long-axis plane was utilized to measure the distance between CO and aortic annulus, it was easier to detect the inferior boundary of the CO from the 3D reconstructed aortic valve models. Meanwhile, the heights of aortic sinuses measured in this study (Table 2.2) were higher than the values found in the literature [52, 110, 112]. Similarly, the superior borders of the aortic sinuses might be detected more easily from the 3D reconstructed aortic valve models than on a 2D long-axis plane.

2.4.3 Limitations

The aortic root geometry during systole was not considered. However, Tops *et al.* [110] and Kazui *et al.* [118] found that no significant differences in annulus diameter were observed between diastole and systole. Another limitation of the present study was that no patients with severe aortic stenosis or bicuspid aortic valve were incorporated. As a pilot study to use a 3D model, we chose to exclude the aortic stenotic and BAV patients to simplify our data analysis.

2.5 Summary

In this chapter, full 3D aortic root models reconstructed from clinical MSCT scans of 94 patients were used to perform dimensional analysis of the aortic root geometry in diastole. Similar dimensional measurements were obtained from the 3D models and 2D MSCT scans. The main source of differences between the two methods could be the orientation and position of the cutting planes chosen for aortic root measurements. Moreover, the 3D perimeter-derived annulus and SOV diameters were different from the direct diameter measurements on short axis views. It was noted that the perimeter measurements could account for the non-circular geometries of the annulus and the SOV, which might represent more accurate dimension estimations. This chapter also indicated that the left CO is predominantly located in the upper right region of the left coronary sinus. Since anatomical features of the aortic root can be easily identified on a full 3D geometric model, more complete information could be obtained.

CHAPTER 3

DEVELOPMENT OF A PATIENT-SPECFIC FE MODEL OF TAV DEPLOYMENT

In the previous chapter, multi-slice computed tomography (MSCT) was selected as the imaging modality for the reconstruction and measurement of the aortic root geometry due to its availability and spatial resolution. In this chapter, we explored the possibility of using aortic geometries reconstructed from MSCT scans to create computational models of TAV stent deployment. In order to determine the necessary anatomical structures that should be included into the models, three initial aortic root geometries were analyzed: (a) aortic root geometry directly reconstructed from MSCT scans, (b) aortic root geometry at the rapid right ventricle pacing phase, and (c) aortic root geometry with surrounding myocardial tissue.

Overall, the results of this chapter suggested that computational models could be used to quantify the biomechanical interaction between the transcatheter aortic valve (TAV) stent and the stenotic aortic valve during TAV intervention. The results of this chapter were published in [75].

3.1 Introduction

During TAVI intervention, the interventional cardiologist does not have direct access to the calcified aortic valve, and must rely on the interaction between the TAV stent and the host tissue to maintain proper device positioning and function. Many of the adverse effects [119-122] seen in clinical trials, such as impairment of coronary flow, cardiac tamponade, stroke, peripheral embolism, aortic injury, paravalvular leak and access site injury [40, 123], can be explained from the biomechanics perspective. For instance, excessive radial expansion force of the TAV stent may cause aortic injury, while insufficient force may lead to paravalvular leakage and device migration. Improper TAV positioning can also cause occlusion of the coronary ostia (CO). Thus, a quantitative understanding of the biomechanics involved in the TAV intervention is critical for the success of this procedure.

Due to the complex geometry, mechanical properties and contact between the TAV stent and the aortic root in TAV intervention, integrated experimental and computational methods are necessary to evaluate the biomechanical response. Finite element (FE) analysis has been utilized to study the biomechanics of the aortic root [83, 103, 124-126] or TAV devices [68-70, 127, 128] individually. However, the biomechanical interaction between the stenotic aortic valve and TAV stent has been largely unexplored, and therefore is the focus of the present chapter. Specifically, patient-specific FE models of aortic roots were reconstructed from multi-slice computed tomography (MSCT) scans, and stent expansion during TAV deployment was simulated. Contact force between the stent and aortic root, as well as stress and strain changes in aortic tissue due to the stent expansion were analyzed.

3.2 Methods

3.2.1 Patient-Specific Aortic Root Geometry

Full phase cardiac MSCT scans were collected from patients at Hartford Hospital (Hartford, CT). Institutional Review Broad approval to review de-identified images was obtained for this study. One stenotic patient with a tricuspid aortic valve and an aortic annulus size of 21 mm was identified from the database. Severe calcification was found in the leaflets of the patient. The MSCT examination was performed on a GE LightSpeed 64-channel volume computed tomography scanner. In general, a total of 2000 slices of images with thickness of 0.625 mm were collected for the whole cardiac cycle [45]. MSCT images in systole were imported into Avizo 6.3 software (VSG, Burlington, MA) for 3-dimensional (3D) reconstruction and evaluated using a window width of 950 and -50 Hounsfield units. Aortic root and left ventricle were identified and separated from the rest of the chest images to create a 3D representation. A FE mesh of the 3D aortic root model was generated using HyperMesh (Altair Engineering, Inc., MI) software (Figure 3.1). Three-dimensional solid elements (eight-node hexahedral C3D8I and four-node tetrahedral C3D4 elements) were used to model the aortic root, leaflets, and myocardium.

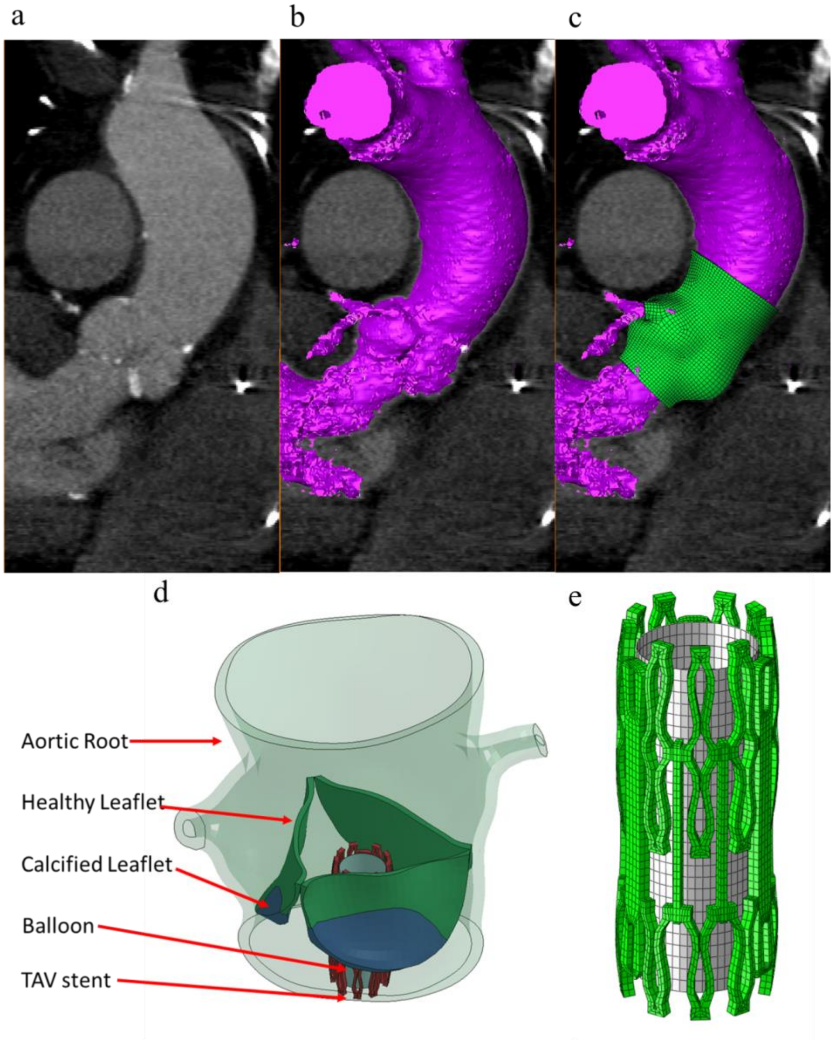

Figure 3.1 (a) MSCT images of the aortic valve in long-axis view overlapped with (b) automatic-segmented interior surface mesh of the aortic valve and (c) the final 3D finite element aortic valve model, (d) TAV stent deployment inside the aortic roots with AS, and (e) TAV stent and balloon.

In TAVI intervention, a rapid ventricular pacing is introduced during the TAV stent deployment [129], aortic pressure is thus reduced from 80-120 mmHg to 0-20 mmHg. Consequently, the aortic root geometry reconstructed from MSCT scans under normal aortic pressure is different from the aortic root geometry during rapid pacing. Previous studies on patient-specific aortic wall stress showed that neglecting existing stress in CT-reconstructed geometry could lead to inaccurate prediction of wall stress and deformation in FE simulations[130, 131]. Thus, to estimate the aortic root geometry at the rapid ventricular pacing, we utilized the pressure vs. diameter relationship obtained from in-house inflation tests of human aortic roots (described in the Appendix A and published in [64]); and determined that about 10% strain could be induced by inflating the aortic root from 0 mmHg to 80 mmHg (Figure 3.2). Therefore, we uniformly applied -10% strain to the CT reconstructed aortic root geometry to approximate the rapid ventricle pacing geometry, which resulted in an aortic root with an annulus size of 19.

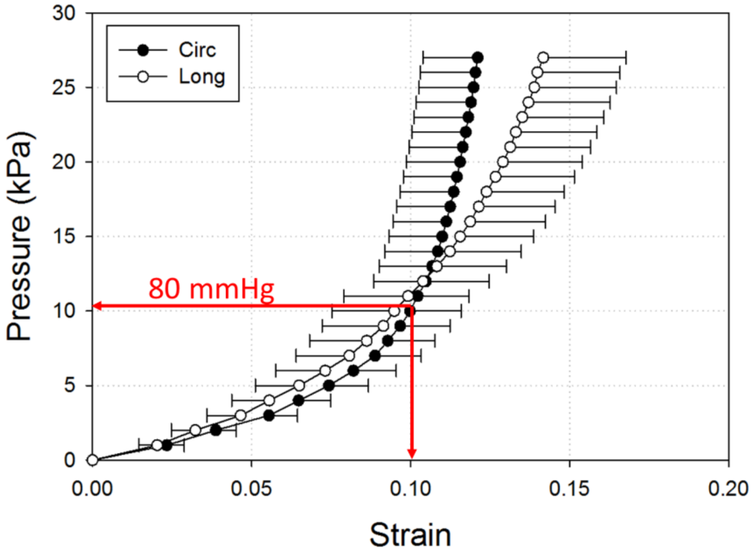

Figure 3.2 Pressure-strain data (mean and standard error) of human ascending aortas under 200 mmHg (27 kPa) in circumferential (Circ) and longitudinal (Long) directions.

Furthermore, it is known that the aortic root, in particular the aortic annulus, is the main component interacting with the TAV stent for its anchoring. The impact of the myocardium, affixed to the lower parts of the aortic sinuses of Valsalva, on the interactive force during TAV stent deployment is unclear. Thus, in this chapter, the myocardium surrounding the aortic root was included in the FE models to investigate whether the presence of myocardium would affect the biomechanical interaction between the aortic root and TAV stent (Figure 3.3b). In summary, we compared three initial geometries for the patient in this chapter: (a) aortic root geometry (size 21) directly reconstructed from MSCT scans, (b) aortic root geometry (size 19) at the rapid pacing phase, and (c) aortic root geometry (size 19) with surrounding myocardial tissue.

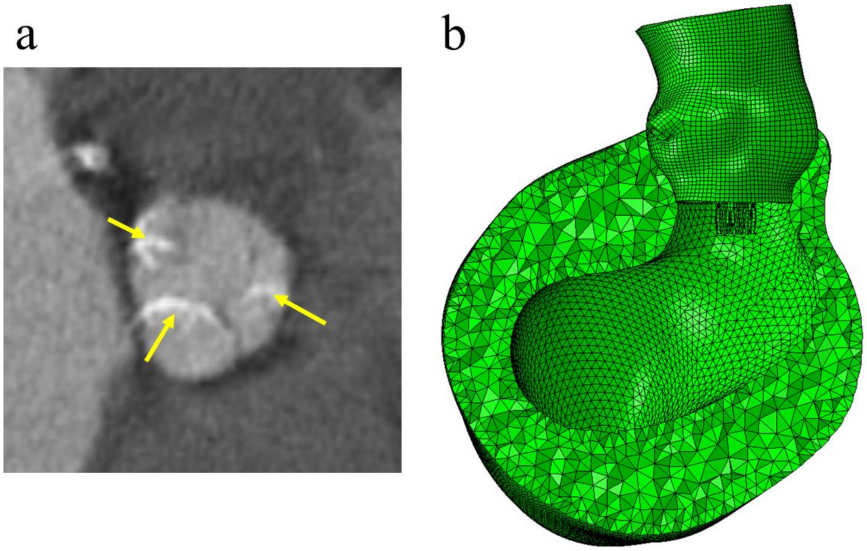

Figure 3.3 The presence and severity of aortic leaflet calcifications were evaluated on MSCT images: (a) extensive calcified spots (indicated by yellow arrows) in all leaflets. (b) Finite element models of the aortic roots with myocardium.

3.2.2 Patient Information

The patient with AS was a 77-year-old male. Aortic annulus diameters and CO height were measured from MSCT scans. The aortic valve annulus was defined at the lowest level of the insertion of the valve cusps into the aortic root (Figure 3.1a). The height of the CO was measured as the axial (vertical) distance from the inferior border of the coronary artery to the aortic annulus plane. For this patient, the maximum and minimum aortic annulus diameters before the TAV stent deployment were 23.6 mm and 17.7 mm respectively. The heights of left and right CO were 10.7 mm and 16.4 mm respectively. In one of our previous studies [45], a dimensional analysis of the aortic root geometry of 94 patients was performed using full 3D aortic root geometric models reconstructed from clinical MSCT scans. We found that the aortic root dimensions of the patient used in the current study fell in the typical range of the aortic measurement results obtained in the previous study, thus, this patient is representative in terms of his anatomic dimensions. The area of calcified leaflets quantified from the MSCT images was 127.3 mm^2. It was also observed from the MSCT images (Figure 3.3a) that for this patient, calcified tissue was at the bottom of all three leaflets in the vicinity of the leaflet attachment line.

3.2.3 TAV Stent Geometry and Material

Three-dimensional solid elements (eight-node hexahedral C3D8I) were used to model the TAV stent, while three-dimensional shell elements (four-node reduced quadrilateral S4R elements) were used to model the balloon (Figure 3.1e). The stent and the balloon were positioned such that the stent was coaxial with the aortic root and approximately one half of the stent was below the aortic annulus based on the manufacturer’s guideline for Edwards SAPIEN XT TAV device deployment [132]. The stent was modeled with the properties of cobalt-chromium [133] with a Young’s modulus of 243 GPa and a Poisson ratio of 0.3. The stent model had a height of 14.5 mm and a thickness of 0.5 mm. The TAV leaflets were not included in the model because the effects of TAV leaflets on biomechanical interaction between the TAV stent and native tissue during the stent expansion were negligible.

3.2.4 Constitutive Models of Aortic Tissue

An anisotropic hyperelastic material model was adopted to characterize mechanical behaviors of the aortic tissues (i.e., aortic leaflets, aortic sinus, ascending aorta and surrounding myocardium). The model is based on the fiber-reinforced hyperelastic material model proposed by Holzapfel et al. [99, 134], which has been shown to accurately capture the behavior of blood vessel inflation under internal pressurization. Briefly, the aortic tissues are assumed to be composed of a matrix material with two families of imbedded fibers, each of which has a preferred direction. The fiber directions (theta) can be mathematically described using two unit vectors. The strain invariant $\overline{I}_1$ is used to describe the matrix material; and the strain invariant $\overline{I}_{4i}$ is used to describe the properties of the fiber families. $\overline{I}_{4i}$ is equal to the squares of the stretches in the fiber directions. The strain energy function W can be expressed as

$$W = C_{10}\{\exp[C_{01}(\overline{I}_1-3)]-1\}+\frac{k_1}{2k_2}\sum_{i=1}^{2}\left[\exp\left\{k_2\left[\kappa\overline{I}_1+(1-3\kappa)\overline{I}_{4i}-1\right]^2\right\}-1\right]+\frac{1}{D}(J-1)^2 \text{ , } i=1,2 \qquad (3.1)$$

where, C_{10}, C_{01}, k_1, k_2 and D are material constants. C10 and C01 are used to describe the matrix material. D is the material constant that introduces the near incompressibility, while k_1 is a positive material constant with the dimensions of stress and k_2 is a dimensionless parameter. In addition, a dispersion parameter κ was used to describe the distribution of fiber orientation. When κ=0, the fibers are perfectly aligned (no dispersion). When κ=0.33, the fibers are randomly distributed and the material becomes isotropic. The anisotropic hyperelastic material model was implemented into Abaqus 6.10 (SIMULIA, Providence, RI) with a user sub-routine VUMAT. Local coordinate systems were defined for each leaflet, sinus, and myocardium to include fiber orientations for each region.

3.2.5 Material Parameters Obtained from Inverse FE Method

Load-controlled biaxial tests of healthy human aortic valve leaflets, aortic sinuses and ascending aorta (80-year-old female) were reported by Martin et al. [53]. In addition, an in-house load-controlled biaxial test of healthy human myocardium (79-year-old female) was used. Briefly, a square specimen (about 25 mm in length) of the posterior side below the coronary sinus of the left ventricle wall was cut out and sliced into three layers: endothelium, myocardium and epicardium. The thickness of the endothelium, myocardium, and epicardium are 1.99, 2.47 and 2.17 mm, respectively. In this chapter, the myocardium mechanical properties were generalized by obtaining only the myocardium layer to present the entire left ventricle wall. To determine the passive characteristics of the myocardium, the specimen was submerged and tested in a Ca2+-free saline solution with EGTA (a chelating agent with a high affinity for Ca2+) and 0.1M papaverine. Biaxial testing was carried out according to the methods presented in Sacks and Sun [135]. The longitudinal and circumferential axes were aligned with the apex to base and circumferential directions of the heart, respectively. The specimen was preconditioned for 20 cycles with a maximum load of 80g in each direction.

An inverse FE method was used to estimate the model parameters by comparing FE simulated tissue responses with the experimental data. Briefly, in this procedure, an equal-biaxial loading protocol was applied to a single solid element to simulate the responses of aortic tissue. The material parameters of the constitutive model of Eqn. (1) were obtained by iteratively minimizing the difference between stress-strain relationships extracted from the single element simulation and the experimental data. This process is automatically realized by using a Matlab code that executes the simulation, extracts data from simulation output files and performs optimization of the parameters.

3.2.6 Modeling of Calcified Leaflets

Leaflet calcification of the patient in this chapter had distinct and regional calcified tissue formations (Figure 3.3) that can be observed from the MSCT images. The focal calcified regions of the leaflets were modeled in the FE models according to their size, thickness, and location based on the MSCT images. Calcified tissues were modeled with the properties of hydroxyapatite with a Young's modulus of 60 GPA and a Poisson ratio of 0.3.

3.2.7 Boundary Conditions

A displacement-controlled deformation was prescribed to the balloon in its radial direction so that it expanded the TAV stent to an outer diameter of 23 mm. The displacement-controlled condition was utilized based on the clinical observation that most of the Edwards SAPIEN stents used remained circular in cross-section after deployment, even within heavily calcified native valves[136]. The top of the ascending aorta was constrained to allow only rotational degrees of freedom. Friction coefficients between TAV stents and stenotic aortic roots are currently unknown. Thus, in this chapter, frictional coefficient of 0.1 was assumed based on the study by Vad *et al.* [137] on a self-expanding endovascular stent-graft. To evaluate the effect of the mesh density on simulation results, a mesh sensitivity study was performed on the FE models.

3.3 Results

3.3.1 Material Models

The best-fitted material properties of aortic tissue as well as the corresponding biaxial test data are illustrated in Figure 3.4. The obtained material parameters are listed in Table 3.1. It can be seen in Figure 3.4 that there was very good correlation between simulation and biaxial results. From the biaxial results it can be seen that the sinus and aortic leaflet tissues had stiffer mechanical response in the circumferential direction, while the ascending aorta was stiffer in the longitudinal direction. This intrinsic material property was reflected in the material model by the angle (theta) between collagen fibers and the circumferential direction, which was larger for the ascending aorta in Table 3.1.

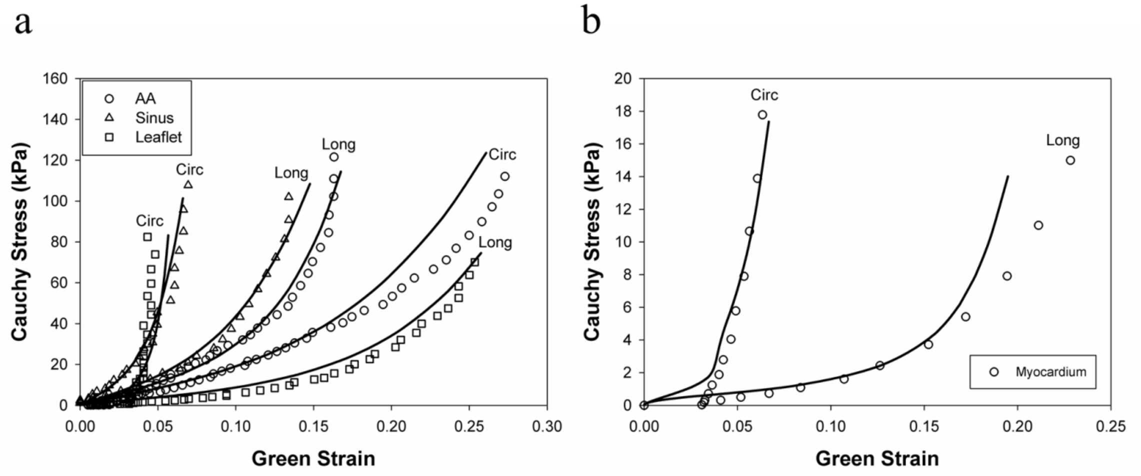

Figure 3.4 Equal-biaxial results (circles) of the (a) aortic sinus, ascending aorta, leaflet, (b) myocardium in circumferential (Circ) and longitudinal (Long) directions and their responses predicted by finite element simulations (lines).

Table 3.1 Material parameters of healthy human aortic sinus, ascending aorta, leaflet, and myocardium.

	C_{10}	C_{01}	K_1	K_2	κ	D	Theta (°)
Sinus	1.7553	13.7077	10.5507	80.3790	0.0006	0.0005	20.06
Ascending aorta	4.1755	3.4649	3.7711	15.9276	0.0864	0.0005	70.95
Leaflet	0.9627	6.3928	12.7250	48.6769	0.0711	0.0005	28.04
Myocardium	0.0374	15.3875	6.0798	98.3666	0.1440	0.0005	6.78

3.3.2 Simulation Results

The deformed leaflets and aortic root of the patient after the maximum stent deployment are shown in Figure 3.5 and Figure 3.6. Aortic leaflets were pushed behind the TAV stent. No severe leaflet overhanging or obstruction of CO was observed. The distance between the left CO and the leaflet free edge was found to be 3.6 mm (as indicated by the double-sided yellow arrow in Figure 3.6b). The maximum and minimum aortic annulus diameters after the TAV stent deployment were 24.6 mm and 23.1 mm respectively. Also, no significant change in CO heights was observed before and after TAV stent deployment.

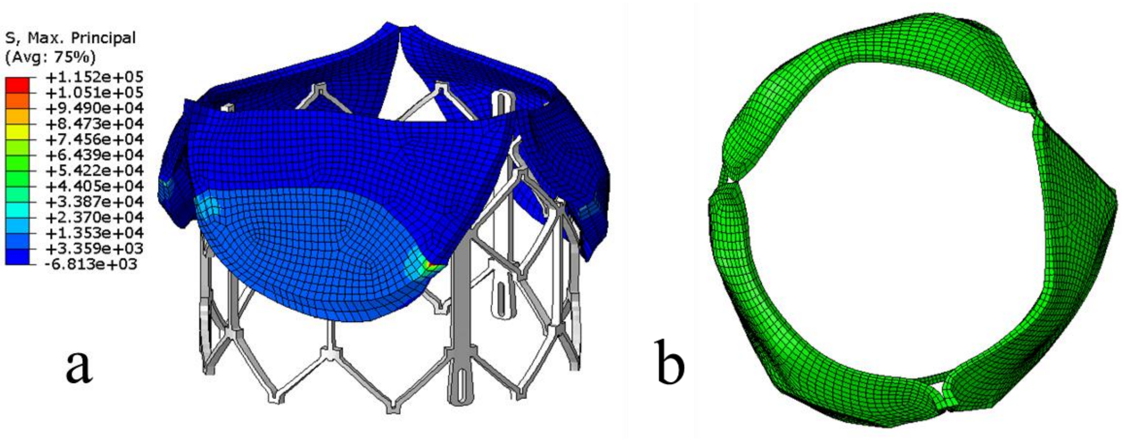

Figure 3.5 Side views (a) and top views (b) of deformed native valve leaflets of the patient after the maximum stent deployment.

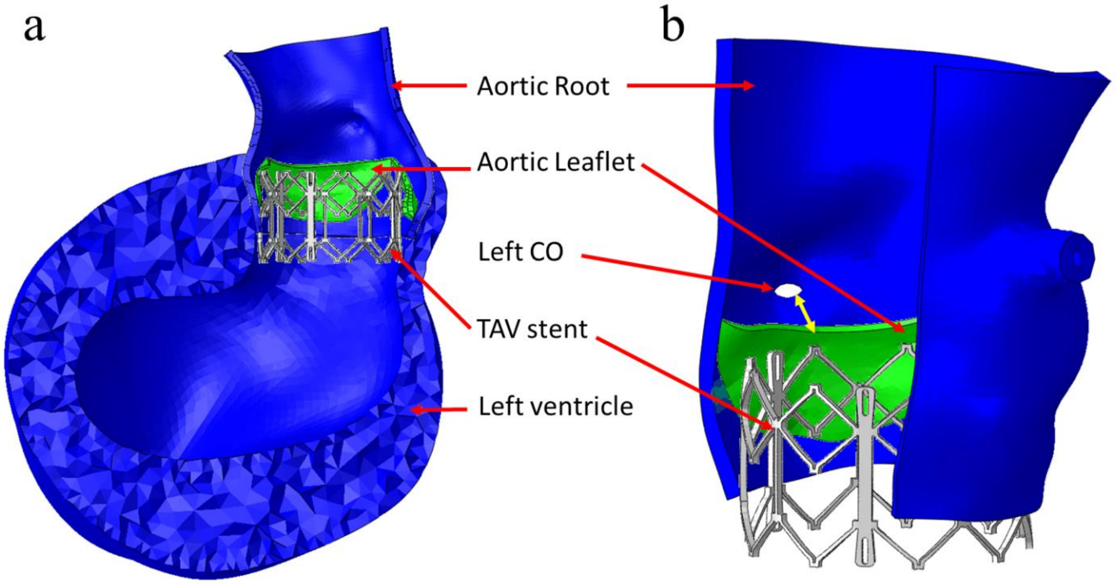

Figure 3.6 (a) Side view of deformed aortic root and left ventricle of the patient after the maximum stent deployment. (b) Double-sided yellow arrow shows the distance between the left CO and deformed leaflet free edge.

Contact forces between the stent and aortic root are listed in Table 3.2. Contact forces of the aortic root models reconstructed directly from MSCT scans (size 21) were significantly lower than those of the scaled aortic root models (size 19). Furthermore, contact forces increased slightly with the inclusion of myocardium to the model. Similarly, as listed in Table 3.2, maximum stresses and strains of the original aortic root models were lower than those of the scaled models. The presence of myocardium induced slightly higher stresses and strains in the aortic root.

Table 3.2 Mechanical responses of the aortic root at maximum TAV stent expansion.

Mechanical Responses	**Geometry**		
	#1	**#2**	**#3**
Contact normal force (N)	27.64	125.70	149.02
Contact shear force (N)	2.68	11.09	12.58
Peak MPS in the calcium deposit regions of leaflets (MPa)	115.2	564.1	641.2
Peak MPS in leaflet tissue within 1 mm vicinity of the calcium	5.37	36.49	44.41
Peak MPS in leaflet tissue beyond 1 mm vicinity of the calcium	3.51	13.03	13.03
Average MPS in leaflet tissue, excluding the calcium deposit	0.50	2.67	2.91
Average MPS in aortic sinus tissue* (MPa)	0.17	0.86	0.87

Footnote: #1 is the initial aortic root geometry (size 21) which is reconstructed directly from MSCT images, #2 is the scaled aortic root geometry (size 19) which represents the rapid pacing geometry, and #3 is the scaled aortic root geometry (size 19) with the addition of surrounding myocardium. * averaged over the aortic sinus elements below the commissures. MPS is the Maximum Principal Stress in the unit of MPa.

The stress distribution in the aortic leaflets, as well as the deformed leaflets and stent geometries, are shown in Figure 3.5 and Table 3.2. Generally, highest stresses were observed at the calcified spots of the leaflets as well as the transition region between calcified and native tissues (Table 3.2). High stress and strain was also observed at the leaflet-root attachment lines and at the aortic wall between leaflets where the aortic root contacted the stent struts. The top views of the deformed aortic root cross-sections at maximum stent deployment are shown in Figure 3.7. Due to the calcified leaflets, the deformed shape of the aortic annulus of the patient was not circular and thus, gaps can be seen between the stent and annulus, which indicated a potential of paravalvular leak.

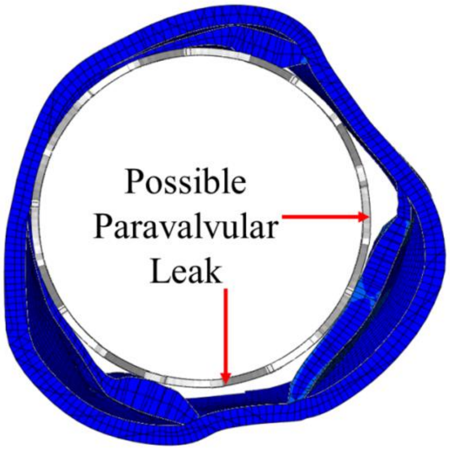

Figure 3.7 Sectional view of the deformed aortic roots of the patient at the maximum stent deployment showed the possible paravalvular leak locations.

3.3.3 Mesh Sensitivity Analysis

The element number of the aortic root and leaflets was increased from 5408 to 21632 to 86520. Mesh sensitivity was also conducted varying the number of elements of the stents from 735 to 5880. There was approximately 0.8 % difference in peak contact normal force between the original and finest mesh. The differences in average maximum principal stress and strain in the aortic root between the original and finest mesh were roughly 5.1% and 3.8% respectively.

3.4 Discussion

Successful TAV deployment and function are heavily reliant on the aortic root-TAV stent interaction. Since the human aortic valve has a large variation of anatomic structures, e.g. different annulus size, sinus height, CO location [46, 52, 138] and tissue stiffness [53], determination of appropriate interaction forces between the TAV and the native tissue using either in vivo or ex vivo measurements is a challenging task. In this chapter we conducted a FE analysis of one patient in TAV intervention and quantified the associated interactive forces, stresses and strains in this procedure.

Stress analysis of patient-specific vascular structures commonly assume that the reconstructed in vivo geometries derived from biomedical images are stress–free, although they are in a pre-deformed state due to the presence of arterial pressure [139]. In this chapter, the simulation results clearly demonstrated that there was a significant difference in stress, strain, and contact forces between the aortic root models directly reconstructed from MSCT scans (size 21) and the scaled aortic root models (size 19) for the rapid ventricular pacing phase, which underscores the importance of choosing an appropriate initial aortic root geometry in FE simulation. It is noted that our scaled aortic root geometry is a rough approximation and will not be accurate at a patient-specific level. Ideally, 3D imaging modalities such as CT scans may be performed at the rapid pacing phase such that an accurate estimation of the aortic root geometry at 0-20 mmHg can be obtained. Alternatively, an inverse FE method could be used to deduce the aortic root geometry at the rapid pacing using the approach by Zhou et al. [139]. In addition, in the FE models we did not consider the aortic wall residual stress [140]. For AS patients the aortic root is heavily calcified. The impact of such calcification on the arterial wall residual stress is currently unknown. However, the residual stress, if included in the FE model, should make the aortic root more compliant.

The simulation results also indicated that the surrounding myocardium contributed to the increase of the mechanical responses during TAV deployment. We noted that the passive myocardium tissue in the aged patients was much more compliant compared to the aortic root tissues. Thus, its contribution to the biomechanical interaction might be secondary. However, in our simulations the active contraction from myocardium was not considered, which, if considered, should increase the interactive forces imposed on the TAV stent during the cardiac cycle.

Calcified leaflets are removed during a surgical valve replacement procedure. In current TAV interventions, however, the leaflets are not removed, but rather pushed aside by the TAV stent. Whether these leaflets have any mechanical impact on the TAV intervention is currently unclear. It has been suggested that these calcified leaflets be removed prior to the TAV intervention by a separate minimally invasive means [141]. Our simulation results showed that high stress concentrations (Table 3.2) were seen around the calcified regions in the leaflets as well as at the attachment lines of leaflets and the aortic sinuses. These high stress concentrations indicated that the leaflets carried a substantial amount of loads, thus, helped secure the stent in position [142]. However, the high stress concentrations around the calcified regions also suggested a potential of tissue tearing and breakdown of calcium deposits in these regions, which might cause an increased risk of stroke [132].

3.4.1 Limitations

No rupture or damage mechanism has been incorporated into our FE model. The peak stresses observed in the calcified tissue are high enough to cause tissue tearing and breakdown of calcifications. Fracture of the calcification could reduce the overall stiffness of the aortic root and leaflets, thus, the radial force that the TAV stent exerted on the aortic root could decrease. The angle of collagen fiber orientation was assumed to be a constant; and was determined from optimization of material parameters against biaxial test data. Future work will be needed to obtain the collagen fiber orientation from histology analysis of aortic and left ventricle tissues. No study was found in the literature [143-145] on the material stiffness of aortic leaflet calcification. Therefore, we used the properties of hydroxyapatite to model the calcification rocks. Additional experimental data is required to verify our assumption and the values we used in our simulations.

3.5 Summary

Patient-specific FE models of stenotic aortic roots were reconstructed from MSCT scans; and TAV stent deployment was simulated. The results showed that mechanical responses of the aortic root model directly reconstructed from MSCT scans were significantly lower than those of the model at the rapid ventricular pacing phase. In addition, inclusion of the myocardium slightly increased the mechanical responses. It was observed that maximum stresses and strains were in the region of leaflet calcification, which could help secure the stent in position. Moreover, these elevated stresses during TAV stent deployment indicated a possibility of tissue tearing and breakdown of calcium deposits, which might lead to an increased risk of stroke. The potential of paravalvular leak or occlusion of coronary ostia can be evaluated from simulated post-deployment aortic root geometries. The developed computational models could be a valuable tool for pre-operative planning of TAV intervention and facilitate next generation TAV device designs.

CHAPTER 4

ANALYSIS OF A TAVI CASE WITH AORTIC ROOT RUPTURE

In the previous chapter, a computational methodology was developed to simulate TAV stent deployment process. In this chapter, the modeling techniques such as geometry reconstruction of detailed anatomical structures, fitting of the material parameters, and boundary conditions of the simulation, were further improved. Subsequently, the developed method was utilized to analyze the mechanism of a clinical adverse event associated with TAVI.

Aortic root rupture is one of the most severe complications of TAVI. The mechanism of this adverse event remains mostly unknown. FE simulations were used to obtain a better understanding of the biomechanical interaction between the tissue and stent for patients with a high risk of aortic rupture. We simulated the stent deployment process of a TAVI patient with high aortic rupture risk using finite element method. Simulation results were evaluated for the risk of aortic root rupture, as well as coronary artery occlusion, and paravalvular leak.

Overall, the results of this chapter suggested that since a systematic study of a large patient cohort of aortic rupture is currently not available (due to the low occurrence rate) to clearly understand underlying rupture mechanisms, case by case engineering analysis is recommended for evaluating patient-specific aortic rupture risk. The results of this chapter were published in [80].

4.1 Introduction

Despite the clinical success of the TAVI, there are still many complications associated with this procedure. One of the most severe complications of TAVI is aortic root rupture [31, 32, 146-149], which could lead to cardiac tamponade and subsequent fatal outcomes. Since aortic root rupture happens rarely (a reported risk of less than 2 % [31, 114, 150]), it is difficult to identify its predictors. As a result, the mechanism of this adverse event remains largely unknown; and a better understanding of the biomechanical interaction between the aortic root and prosthesis is essential to prevent aortic root rupture in TAVI. The purpose of this chapter was to perform an engineering finite element (FE) analysis of TAVI clinical cases, in order to obtain a better understanding of the biomechanical interaction between the tissue and stent for patients with a high risk of aortic rupture.

Computational analysis has been carried out to evaluate the aortic root – transcatheter aortic valve (TAV) interaction from an engineering perspective [72, 74-76, 151]. However, the validity of the simulation results was limited by the assumptions of material properties and boundary conditions. For example, no material failure criteria were incorporated in the previous models. Hence, the injury to aortic root tissue, such as aortic root rupture, was not investigated. Moreover, the balloon expansion process was simplified by either forcing uniform TAV stent expansion in the radial direction or applying constant pressure to the balloon interior. The mechanics between balloon and TAV stent could not be accurately characterized.

In this chapter, I simulated the stent deployment process of a TAVI clinical patient with high aortic rupture. The clinical case was a retrospective analysis of an actual TAVI aortic rupture case. Dynamic structural FE models were created using patient-specific geometries segmented and reconstructed from patient pre-operative CT scans, which incorporated aged human aortic material properties with material failure criteria obtained from mechanical tests. A surface-based fluid cavity method was utilized to simulate the fluid-filled TAVI balloon expansion process for the TAV stent deployment into patient-specific calcified aortic roots. Size 23 Edwards SAPIENT TAV stent, which is the currently approved device in the United States, was implanted in the patient.

Simulation results were evaluated for the risk of aortic root rupture, as well as coronary artery occlusion, and paravalvular leak.

4.2 Methods

4.2.1 MSCT Image Acquisition

The MSCT examination (Figure 4.1) at the Columbia University Medical Center (New York, NY) was performed on a Toshiba 320-channel volume computed tomography scanner. Prior to MSCT angiography, prospective calcium score acquisition was performed (collimation 25 × 3.0 mm, rotation time 375 ms, voltage 120 kV, and tube current 500 mA). The temporal window was set at 75% interval after the R wave for electrocardiographically (ECG) triggered prospective reconstruction.

For MSCT coronary angiography, a collimation of 25-30 × 0.25 mm and a rotation time of 375 ms were used resulting in a temporal resolution of less than 200 ms. The tube current modulation was automated to a maximum of 800 mA at 120 kV. Images were obtained with helical scanning and ECG gating. A timing bolus of 20 cc bolus of Ultravist 370 contrast (Bayer Healthcare Pharmaceuticals, NJ) was administered and followed by a 20 cc bolus of normal saline. A 1 s axial scan with a 1 s inter scan delay with a region of interest at the level of the ascending aorta was obtained until contrast density detected. 80 cc of Ultravist 370 contrast was administered via the antecubital vein at a flow rate of 5.0 ml per second using a Medrad Stellant dual headed injector (Medrad, Warrendale, PA). Data acquisition was obtained during an inspiratory breath hold of approximately 6-8 s with ECG gating. In general, a total of 9000 slices of images with thickness of 0.25 mm were collected for the whole cardiac cycle.

4.2.2 Case Presentation

A 94-year-old female patient with a tricuspid aortic valve and an annulus size of 19.6 mm was referred for TAVI procedure. Echocardiography revealed severe AS in the non-coronary leaflet as well as the interior of the aortic root; only the left coronary leaflet could open during cardiac cycles. The pre-procedural MSCT scans (Figure 4.1) showed heavy calcification on the non-coronary leaflet, and one large calcified spot on the interior of the left coronary sinus at the level between the ostium of the left main stem and the aortic annulus entering the myocardium. A size 23 Edward SAPIEN TAV was implanted. During TAVI procedure, aortic root tearing happened and visualized below the left main coronary artery.

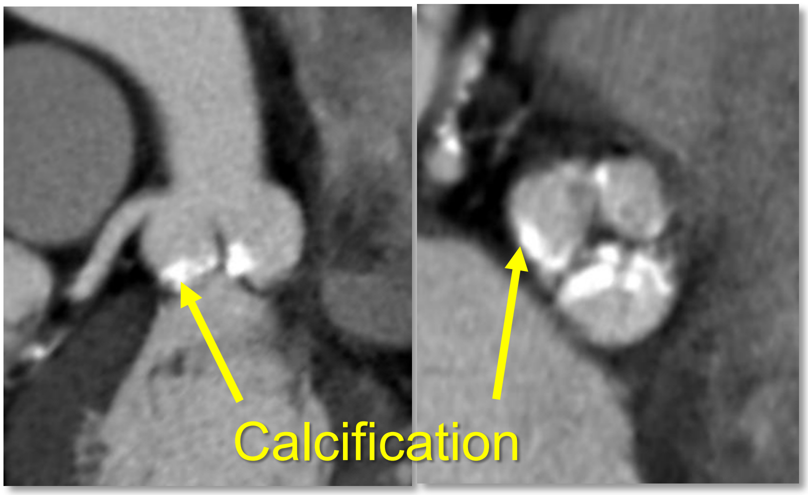

Figure 4.1 Computed-tomography images of a TAVI patient showing aortic calcification.

4.2.3 Patient-Specific Aortic Root Model

MSCT images in diastole were imported into Avizo 8.0 software (VSG, Burlington, MA) for 3-dimensional (3D) reconstruction and evaluated using a window width of 950 and -50 Hounsfield units. Aortic root was identified and separated from the rest of the chest images to create a 3D representation (Wang et al. 2011). HyperMesh software (Altair Engineering, Inc., MI) was used to generate FE mesh of the 3D aortic root model (Figure 4.2), which included aortic root, aortic leaflets, calcification, mitral-aortic intervalvular fibrosa, anterior mitral leaflet, fibrous trigones, and left ventricle. Three-dimensional solid elements (eight-node hexahedral C3D8I, six-node pentahedral

C3D6, and four-node tetrahedral C3D4 elements) were used to simulate the TAVI cases in ABAQUS explicit 6.13 (SIMULIA, Providence, RI) FE software. Calcification (Figure 4.2) was modeled such that the volume of 3D elements in HyperMesh was similar to that was quantified using the material statistics tool in Avizo. Calcification was quantified with density greater than 130 Hounsfield units.

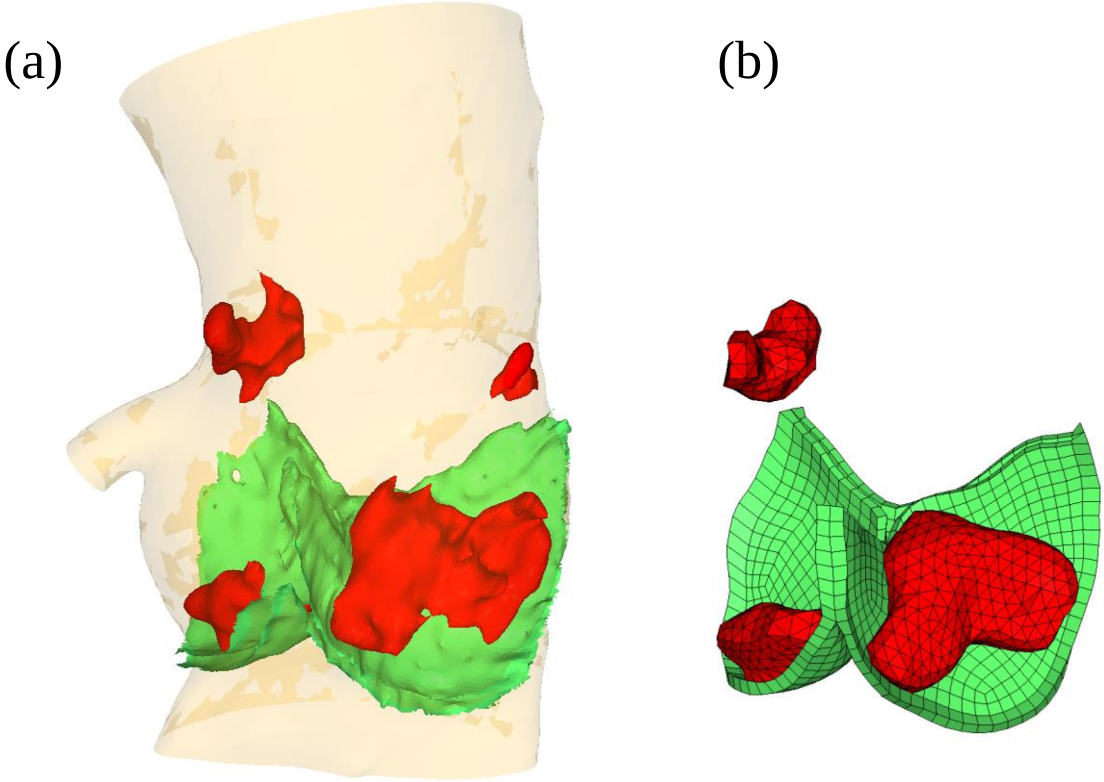

Figure 4.2 The development of an aortic root model: (a) initial image segmentation in Avizo, (b) reconstructed models of aortic leaflets and calcification. For illustration purposes, the yellow geometry in my FE models represents the aortic root, the green geometry represents non-calcified aortic leaflets, and the red geometry represents calcification.

4.2.4 Mechanical Testing of Heart Tissues

Details of the biaxial and uniaxial testing techniques were described in previous chapters. Briefly, in-house load-controlled biaxial tests of human aortic tissues were used to define the valve material properties. Biaxial testing was carried out according to the methods presented in Sacks and Sun [135]. The typical sample size in biaxial tests was 15 mm by 15 mm. Twenty continuous cycles of preconditioning were performed to reduce tissue hysteresis. Each sample was tested at the maximum load possible without causing tissue damage. Tissue samples were assumed to be incompressible and planar. Material properties of the human ascending aorta, sinus, and leaflet were mostly averaged over 10 biaxial test samples of each region.

Uniaxial tests (Figure 4.3) were conducted using dogbone-shaped samples of the aortic-mitral intravalvular fibrosa. The initial length and thickness of the sample was measured by a thickness gauge. The tests were carried out with the specimens submerged in saline solution at room temperature. To precondition the samples, 10 successive loading cycles were executed. Axial load was recorded during the entire test. The Cauchy stress was computed as axial load divided by the current cross-sectional area. The current transversal area was evaluated through the incompressibility condition. The strains were computed during the test by video tracking the displacements of the 2 optical markers placed in the center of the surface of the sample.

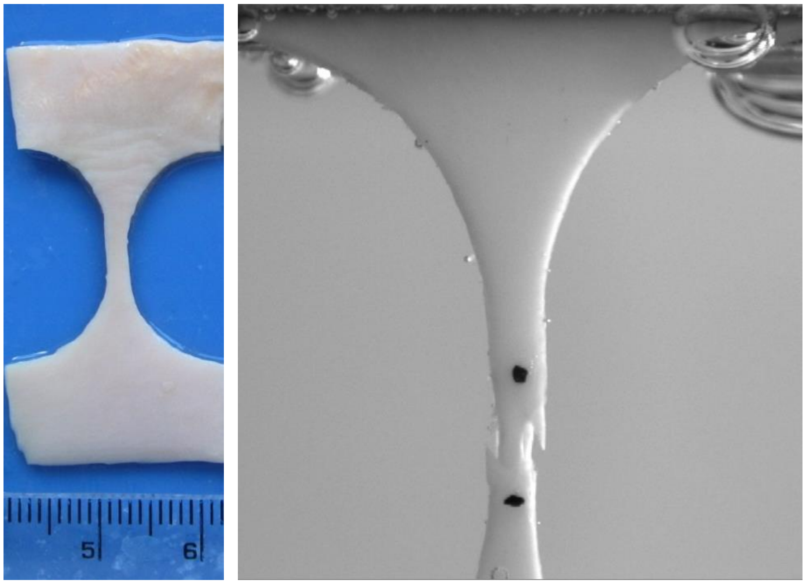

(a) (b)

Figure 4.3 (a) Uniaxial testing samples and (b) testing setup.

4.2.5 Material Models of Heart Tissues

The anisotropic hyperelastic Holzapfel-Gasser-Ogden material model [152] was adopted to characterize mechanical behaviors of the human heart tissues (i.e., aortic leaflets, aortic sinus, ascending aorta, mitral leaflet tissues, and myocardium). The details of the material models of the human heart tissues were described in the previous chapter. The biaxial test data of a human sinus sample and the best-fitted results using the two fiber model are shown in Figure 4.4.

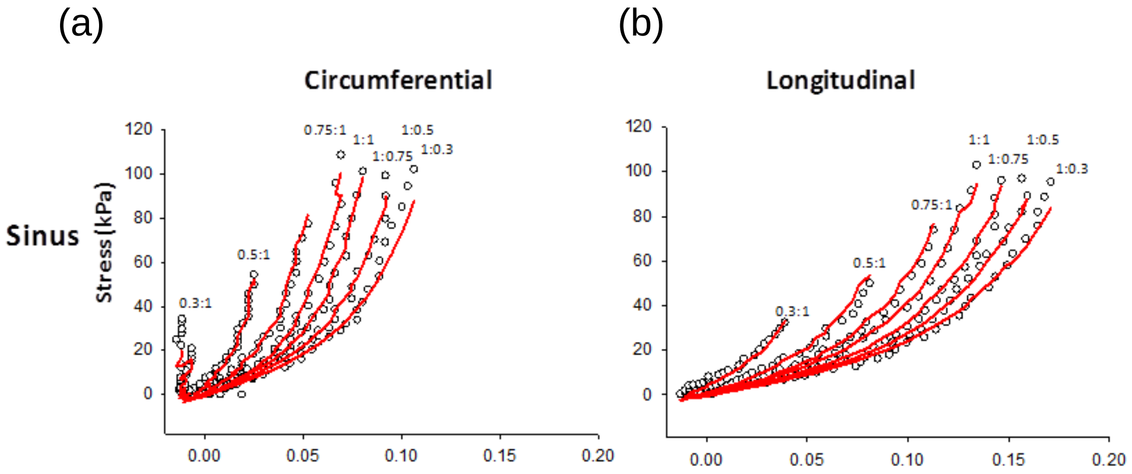

Figure 4.4 Experimental data (open circles) and curve-fitting results (red) of human (a and b) sinuses.

The isotropic hyperelastic Ogden material model [153] was used to characterize the mechanical properties of the human mitral-aortic intervalvular fibrosa and fibrous trigones obtained from uniaxial testing. Aortic valve calcification of the patients in this chapter had distinct and regional calcified tissue formations that can be observed from the MSCT images. Calcified tissues were assumed to be homogeneous and to have a Young’s modulus of 12.6 MPa [144] and a Poisson ratio of 0.3. To simulate the injury to the aortic root, material failure criterion was defined in the ABAQUS explicit user subroutine VUANISOHYPER by specifying a maximum principal stress limit of 2.5 MPa for the aortic sinuses. An element would be deleted from the FE model of the aortic root to simulate the rupture response, when the maximum principal stress was reached in all of the material points of the element. Details of the determination of material parameters for aged human heart tissues were described in previous publications [53, 54, 75]; and material parameters are listed in Table 4.1.

Table 4.1 Material parameters of non-calcified human aortic sinus, ascending aorta, leaflet, myocardium, anterior mitral leaflet, and mitral-aortic intervalvular fibrosa.

	C_{10}	**C_{01}**	**K_1**	**K_2**	**κ**	**D**	**Theta (°)**
Sinus	1.7553	13.7077	10.5507	80.3790	0.0006	0.0005	20.06
Ascending aorta	4.1755	3.4649	3.7711	15.9276	0.0864	0.0005	70.95
Leaflet	0.9627	6.3928	12.7250	48.6769	0.0711	0.0005	28.04
Myocardium	0.0374	15.3875	6.0798	98.3666	0.1440	0.0005	6.78
Mitral Leaflet	0.1245	13.6655	11.0069	84.8478	0.0800	0.0005	13.09
	μ_1	**α_1**	**μ_2**	**α_2**	**μ_3**	**α_3**	
Fibrosa	2069.4	12.5	94.8	12.5	3182.6	12.5	

4.2.6 TAV Stent Geometry and Material

The stent model had a height of 14.3 mm and a thickness of 0.5 mm, which was generated using the depictions in the literature to closely resemble the Edwards Sapien stent geometry (Figure 4.5). The stent was modeled with the properties of 316 stainless steel with a Young's modulus of 193 GPa , a Poisson ratio of 0.3, and initial yield stress of 340 MPa [73]. The TAV leaflets were not included in the model because the effects of the TAV leaflets on biomechanical interaction between the TAV stent and aortic tissues during the stent expansion were assumed to be negligible. This assumption was based on the fact that TAV leaflets do not have direct contact with the native aortic tissue. Also, material properties of the TAV leaflets are significantly more compliant than those of the stainless steel stent. The pre-deployment geometry of the stent (Figure 4.5) was obtained by applying a displacement field outside in the radial direction to crimp the stent to an outside diameter of 7.3 mm.

4.2.7 Modeling of Balloon Deployment and Simulation Setup

The mechanical response of a fluid-filled balloon expansion was modeled by a surface-based fluid cavity method in ABAQUS explicit, which was capable of simulating the coupling between the deformation of the balloon and the fluid inside with uniform properties and state. Three-dimensional membrane elements (M3D4) were used to model a fully enclosed balloon, which resembled the Edwards RetroFlex 3 balloon geometry. The outer diameter, thickness, and total length of the balloon were 22 mm, 0.06 mm, and 63 mm, respectively. The balloon had a Young's modulus of 600 MPa and a Poisson ratio of 0.4 [73]. The crimped balloon geometry (Figure 4.5) was obtained by applying a displacement field in the radial direction to a cylindrical crimper outside the balloon, to the extent that the balloon could fit inside the stent model. A total of 16 ml of water was used as the fluid to expand the balloon.

The dynamic balloon expansion process was simulated to complete in 1 second, which resulted in a constant flux rate of 16 ml/s. The top of the ascending aorta was constrained permitting only rotational degrees of freedom. Friction coefficient between TAV stents and stenotic aortic roots was assumed to be 0.1 based on the studies by Mummert et al. [65] and Vad et al. [137]. Contact force between the stent and aortic root was output from ABAQUS; and was calculated by summing the normal contact forces of the node set that represented the outside surface of the stent. Deformed geometry of the aortic root was used to examine the possible complications, such as aortic root rupture, coronary artery occlusion, and paravalvular leak.

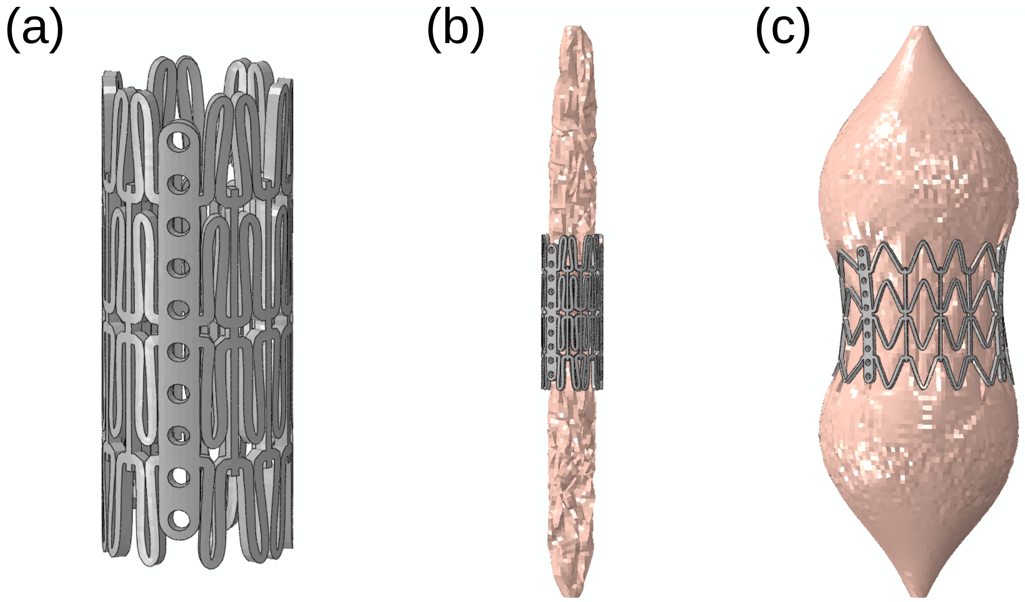

Figure 4.5 (a) Transcather aortic valve stent and (b) a realistic balloon used to simulate (c) fluid controlled balloon deployment.

4.3 Results

The deformed aortic root after the maximum stent deployment is shown in Figure 4.6. The simulation of the TAVI procedure revealed that asymmetric distribution of the aortic calcification lead to asymmetric expansion of the TAV stent with respect to the center of the aortic root. The TAV stent in the non-coronary sinus region was partially expanded, compared to fully expanded stent in the less calcified left coronary sinus region. The calcified spot on the interior of the left coronary sinus was displaced by the TAV stent (Figure 4.6), causing stress concentration at the bottom of the left coronary sinus (Figure 4.7) and consequently the aortic rupture. High stress and strain were generally observed at the aortic tissue where it contacted the calcification and stent struts. Contact radial force between the TAV stent and aortic root reached 109 N, when the stent was fully deployed. Rupture of the aortic root at the bottom of the left coronary sinus occurred at roughly 94 % of the balloon volume. The balloon pressure at full deployment was 3.5 atm. Rupture location in the simulation was the same as that in the clinical case.

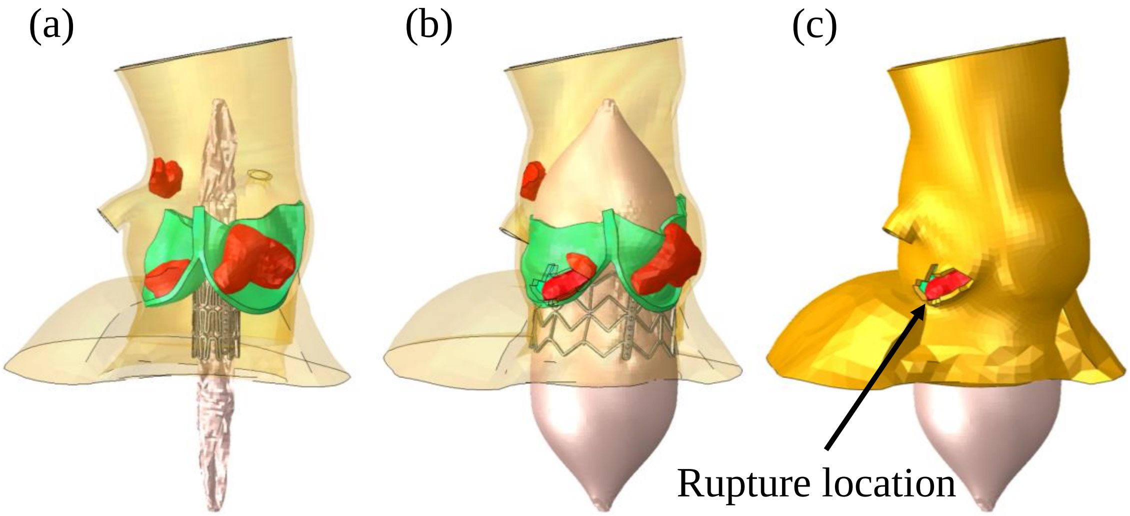

Figure 4.6 (a) Pre- and (b) post-deployment geometries of the aortic root of Case 1. (c) Full and (d) local views of the deformed the aortic root and balloon deployment indicates annulus tearing under the left coronary ostium due to dislodgement of calcification into the vulnerable part of the aortic sinus.

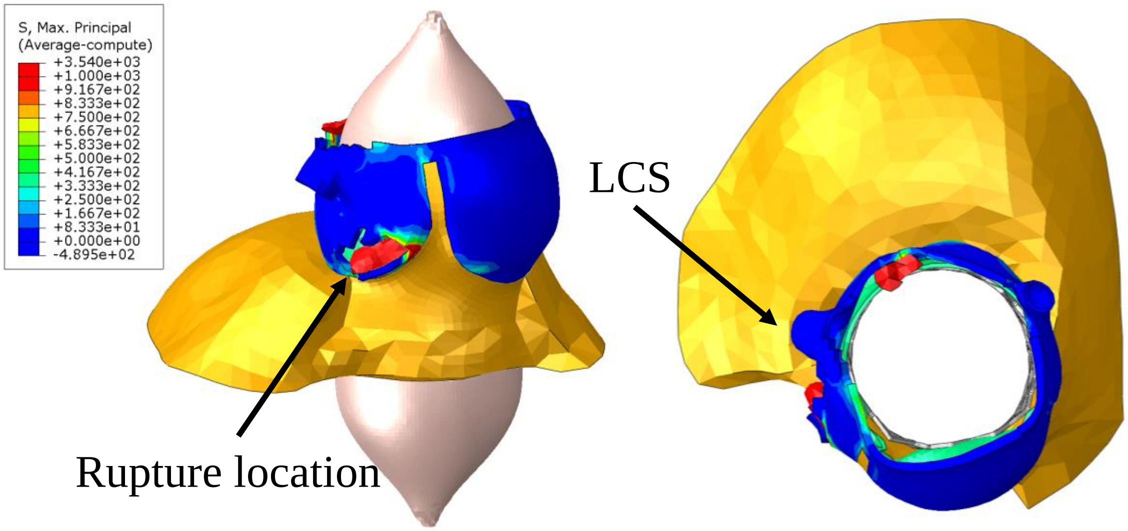

Figure 4.7 Side (a) and top views (b) of the deformed native valve leaflets of Case 1 after the maximum stent deployment showed high stress at location of tearing. Stress (in kPa) contour plot was created for the aortic sinuses.

4.4 Discussion

4.4.1 Potential Mechanisms of the Aortic Root Rupture

The common practice of oversizing of the TAV stent, which is used to reduce the risk of the paravalvular leak [154, 155], could lead to the aortic root rupture. In other studies [31, 32], heavily calcified aortic annulus, LVOT, and leaflets, a narrow or calcified aortic root, enhanced oval shape of the annulus were also identified as anatomical factors that could be responsible for aortic rupture. In the study by Hayashida et al. [147], it was hypothesized that the epicardial fat segment might be a vulnerable area, since this part of the aortic annulus is not covered by cardiac structures and is directly adjacent to the epicardial fat and pericardial cavity. Therefore, it was conjectured that annulus rupture was caused by forceful expansion of the TAV stent, and subsequent dislodgement of calcification into the vulnerable part of the sinus which lacked support of cardiac structure.

In our study, one large calcification was observed on the interior of the left coronary sinus under the left coronary ostium, which was similar to the rupture cases described by Hayashida et al.[147]. By using FE analysis to virtually replicate and visualize the TAV stent expansion process, it can be clearly seen that the large calcified spot on the interior of the left coronary sinus between coronary ostium and the aortic annulus was pushed by the stent, causing the aortic rupture. Thus, the aortic root rupture could be caused by a combination of two factors: (a) the large calcified spot on the interior of the left coronary sinus and near the aortic annulus, and (b) the asymmetric distribution of the aortic calcification due to a significantly large calcification on the non-coronary leaflet. However, multiply patient factors and/or a combination of them could be the cause of aortic root rupture. The patient factors could include the individual patient aortic tissue geometries and material properties, as well as calcification volume, shape, location, and orientation.

TAV sizing directly affects contact forces between the stent and the calcified aortic root. TAV sizing has been identified as one of the key indicators of aortic rupture [31, 32]. Indeed, in the study by Barbanti et al. [31], rupture happened even when aortic valve was under-sized (Patient 18 of the study had a relative area oversizing of -2.58%, while Patient 5 and Patient 19 only had roughly 2% oversizing). Clearly, TAV sizing should be evaluated with patient-specific anatomic features and calcification configurations, which underscored the importance of patient-specific analysis of complicated, rare clinical TAVI cases of aortic rupture.

4.4.2 Limitations

There are many assumptions and limitations in this chapter. Our simulation results should be interpreted with the consideration of these assumptions and limitations. First, only one TAVI clinical cases were investigated in this paper, more prospective clinical cases are needed to validate our modeling methods. In the model setup, we assumed that the TAV stent was deployed at the optimal height and implantation angle. The impact of different stent deployment heights and implantation angles will be studied in the future. There is a lack of studies on the material properties of the aortic valve calcification [143-145]. Therefore, a parametric study may be necessary to investigate the effects of calcification stiffness on biomechanical interaction during TAVI. Similarly, there is a lack of the data on the material properties, including ultimate tensile strength (UTS), of human aortic sinuses in the literature. Based on our preliminary data from uniaxial tests on aortic tissue, the UTS of the aortic sinuses was found to be in the range from 2.3 to 3.1 MPa. A maximum principal stress limit of 2.5 MPa was used as the material failure limit for the aortic sinuses. Since material properties of human aortic tissues could be different even among patients with same age and gender, in order to provide a confidence interval for the simulation results, more material tests on human aortic root tissue should be conducted in future studies. Furthermore, experimental tests will be performed to validate the fluid controlled balloon model. No blood flow was considered in the current study. Therefore, paravalvular leak and coronary occlusion were evaluated by examining the deformed geometries of the stent and tissue.

4.5 Summary

In this chapter, we presented patient-specific FE models of a TAVI clinical case, which incorporated human aortic tissue material properties with material failure criteria, and balloon expansion process using a surface-based fluid cavity method. Simulation results indicated that aortic rupture mechanism was complicated, and could be different among patients. We demonstrated that the engineering analysis could provide additional information to help clinicians evaluate complicated, high risk aortic rupture cases. Since a systematic study of a large patient cohort of aortic rupture is currently not available (due to the low occurrence rate) to clearly understand underlying rupture mechanisms, case by case engineering analysis is recommended for evaluating patient-specific aortic rupture risk.

CHAPTER 5

FE SIMULATION OF TAVI USING ANIMAL MODELS

In previous chapters, a methodology was described to simulate the stent-tissue interaction during the TAVI deployment. However, direct validation of the FE models was limited due to the availability of the in vivo TAVI patient material properties and biomechanical measurements. In this chapter, we tried to validate our modeling approach by simulating the stent expansion process in animal models, which have been used in TAVI clinical feasibility studies.

Micro-computed tomography scans of the porcine and ovine hearts were obtained to reconstruct initial geometries. Biaxial and uniaxial tests were conducted to determine the material properties of the animal heart tissues. The TAV stent deployment inside the animal aortic roots was simulated. The radial contact forces and stent pullout forces were compared to the experimental data in our previous study, where in-house self-expandable Nitinol stents were deployed inside porcine and ovine hearts to measure interactive forces. The comparison of tissue-device contact forces between computational and experimental data demonstrated that the finite element simulations of TAV expansion in animal models could mimic the mechanical responses of the in vitro structural experiments. Also, our results showed that 2 years old porcine hearts had higher structural stiffness than 1-2 years old ovine and 6-9 months old porcine hearts.

Overall, the results of this chapter suggested that our modeling methodology could be potentially utilized to create accurate computational models of TAV deployment.

5.1 Introduction

Several detailed computational models [72, 74-77, 79-81, 151] have been developed to simulate TAVI procedure and to unravel its biomechanics. However, since it is very challenging to obtain in vivo material properties and biomechanical parameters from clinical TAVI patients, there is a lack of direct validation of the computational models. The limited comparison was mostly completed using general clinical observations, echocardiogram, angiogram, and the deformed stent geometries acquired from the post-TAVI CT scans (post-TAVI CT scans are currently not formally recommended as routine follow-up studies in the US). Moreover, animal models, such as porcine and ovine, have been used in TAVI clinical feasibility studies [156-158]. Difference between animal models and human include the presence of aortic calcification and tissue stiffness. As a result, adverse events such as PVL and stent migration were observed in TAVI clinical feasibility studies using animal models. While porcine model is considered to be a substitute of healthy human tissues, there is a need to quantify the discrepancy in the mechanical properties between various animal models at the structural level.

Therefore, the objective of this chapter was to validate the computational modeling methodology that we developed in our previous research for clinical TAVI patients [75, 80, 81] by comparing simulations and experiments of the stent deployment process in animal models. We also attempted to compare the difference in structural mechanical responses between various animal models during TAVI deployment. Specifically, micro-computed tomography (Micro-CT) scans were obtained for the porcine and ovine hearts with an aortic annulus size of 21 mm to reconstruct initial geometries. Animal hearts of the similar age and weight were dissected for the biaxial and uniaxial testing to determine the material properties of the heart tissues. The TAV stent deployment inside the finite element (FE) models of the porcine and ovine aortic roots was simulated in Abaqus/Explicit 6.13 (SIMULIA, Providence, RI). The simulation results (especially the radial contact forces and pull-out forces) were compared to the structural experimental data in a previous study [65], where in-house self-expandable Nitinol stents were deployed inside porcine and ovine hearts to measure interactive forces between the device and tissue. Additionally, TAV deployment simulation results were compared among the different animal models.

5.2 Methods

The overall design of the study is illustrated in Figure 5.1.

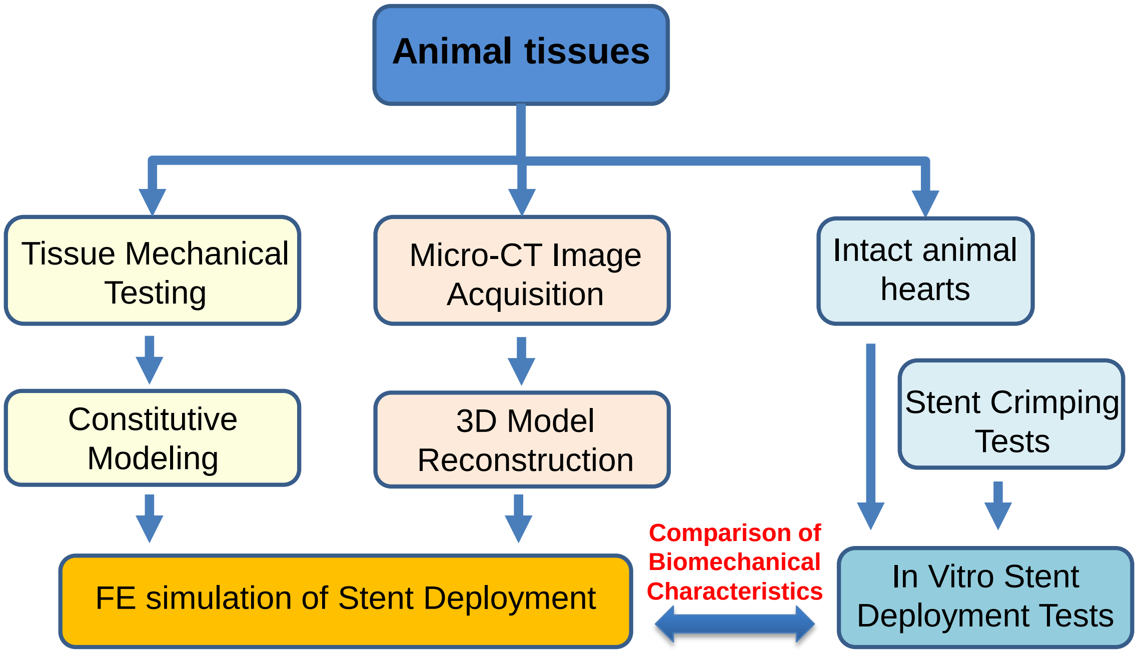

Figure 5.1 Study design for finite element analysis of transcatheter aortic valve implantation using animal models.

5.2.1 Specimen Preparation

Fresh animal hearts (1-2 years old ovine, 6-9 months and 2 years old porcine hearts) were obtained from Animal Technologies Inc. (Tyler, TX USA) and stored in a −80 °C freezer for a maximum of 3 weeks before testing. Prior to testing, each frozen heart was kept at room temperature (20°C) for 30 minutes and then thawed in a 37°C water bath. The hearts were weighed and the aortic annulus size was measured with aortic sizers (Edwards LifeSciences, Irvine, CA). Three animal hearts, i.e., a 1-2 years old ovine (408 g), a 6-9 months old porcine heart (447 g), and a 2 years old porcine heart (750 g), with an aortic annulus size of roughly 21 mm were selected for geometry reconstruction. The left ventricles of the hearts were dissected approximately 10 mm below the aortic annulus plane (Figure 5.2). Extra tissues on the surface of the aortic sinuses were carefully trimmed from the specimens. Each specimen included aortic root, aortic leaflets, mitral-aortic intervalvular fibrosa, anterior mitral leaflet, fibrous trigones, and left ventricle.

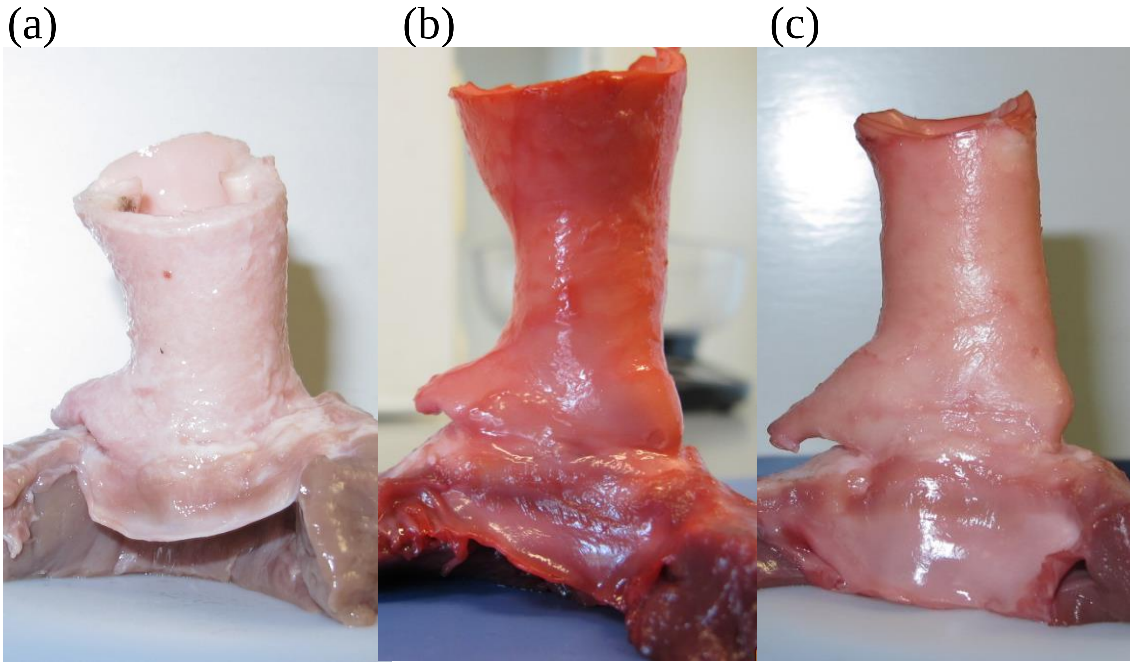

Figure 5.2 (a) Dissected 1-2 years old ovine, 6-9 months and 2 years old porcine hearts.

5.2.2 Micro-CT Image Acquisition and Geometry Reconstruction

The three dissected specimens were imaged using a SIEMENS Inveon micro-CT scanner (SIEMENS, Munich, Germany), which has maximum field of view of 10cm and is capable of imaging live animals and specimens at 20-100um voxel resolutions. Micro-CT images of animal aortic roots (Figure 5.3) were imported into Avizo 8 software (VSG FEI, Hillsboro, OR) for 3-dimensional (3D) reconstruction. The outer and inner surfaces of the aortic root were identified to create a 3D representation (Figure 5.4). HyperMesh software (Altair Engineering, Inc., MI) was used to generate FE mesh of the 3D aortic root models (Figure 5.4), where 3D solid elements (4-node tetrahedral C3D4 elements) were used in Abaqus FEA. The initial geometries of the three aortic roots were slightly scaled to the same annulus size in order to eliminate the error introduced by annulus sizing. Details of the methodology of FE model development were described in previous publications [75, 80].

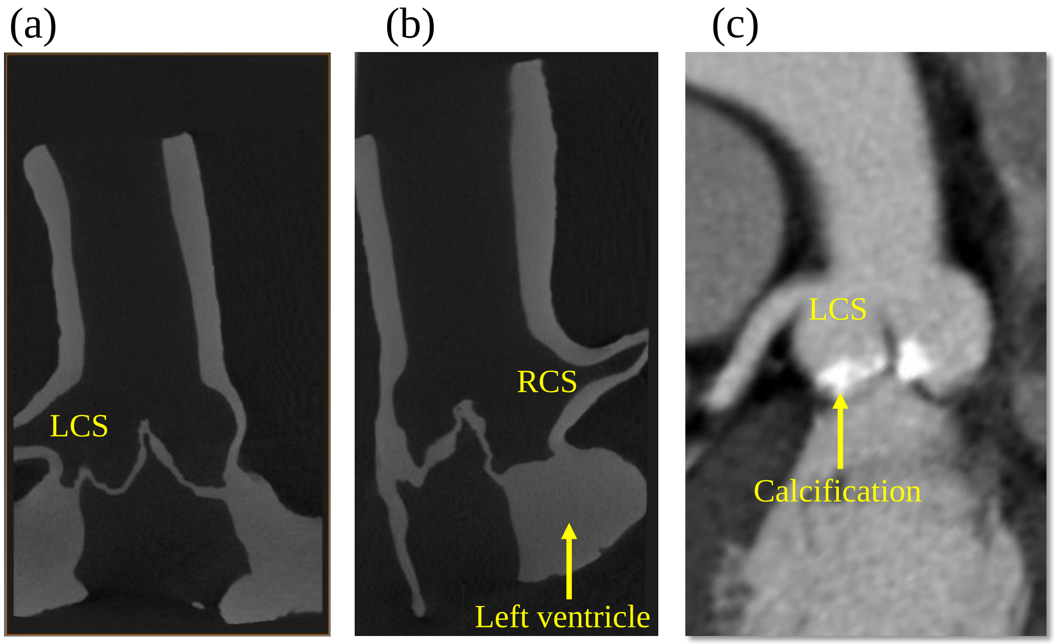

Figure 5.3 Micro-CT scan of the root showing the aortic valve leaflets with (a) left coronary artery and (b) right coronary artery, and (c) clinical CT image of a TAVI patient showing left coronary artery and aortic calcification.
LCS = left coronary sinus, RCS = right coronary sinus

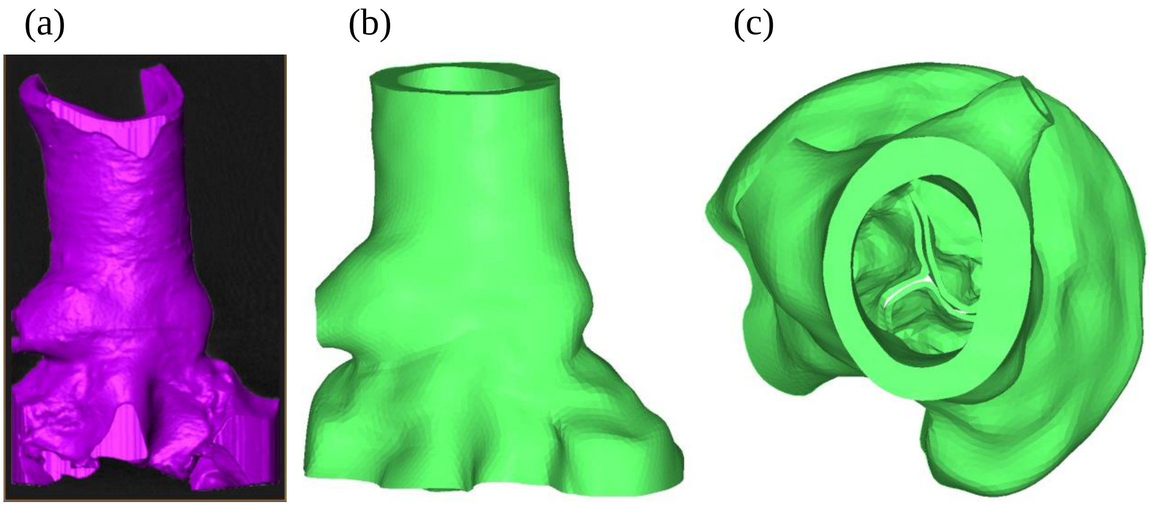

Figure 5.4 (a) Automatic-segmented 3D surface mesh of the aortic root overlapped with the micro-CT image, (b) side and (c) top views of the final finite element model of the 2 years old porcine aortic root.

5.2.3 Planar Biaxial and Uniaxial Mechanical Testing

Details of the biaxial and uniaxial testing techniques were described in previous chapters. Briefly, in-house load-controlled biaxial tests of ovine and porcine aortic tissues were used to define the valve material properties. Biaxial testing was carried out according to the methods presented in Sacks and Sun [135]. The typical sample size in biaxial tests was 15 mm by 15 mm. Twenty continuous cycles of preconditioning were performed to reduce tissue hysteresis. Each sample was tested at the maximum load possible without causing tissue damage. Tissue samples were assumed to be incompressible and planar. Material properties of the ovine and porcine ascending aorta, sinus, and leaflet were mostly averaged over 10 biaxial test samples of each region.

Uniaxial tests were conducted using dogbone-shaped samples of the aortic-mitral intravalvular fibrosa. The initial length and thickness of the sample was measured by a thickness gauge. The tests were carried out with the specimens submerged in saline solution at room temperature. To precondition the samples, 10 successive loading cycles were executed. Axial load was recorded during the entire test. The Cauchy stress was computed as axial load divided by the current cross-sectional area. The current transversal area was evaluated through the incompressibility condition. The strains were computed during the test by video tracking the displacements of the 2 optical markers placed in the center of the surface of the sample.

5.2.4 Material Models of Heart Tissues

The anisotropic hyperelastic Holzapfel-Gasser-Ogden material model [152] was adopted to characterize mechanical behaviors of the animal heart tissues (i.e., aortic leaflets, aortic sinus, ascending aorta, mitral leaflet tissues, and myocardium). Briefly, the heart tissues are assumed to be composed of a matrix material with two families of embedded fibers, each of which has a preferred direction. The isotropic hyperelastic Ogden material model [153] was used to characterize the mechanical properties of the mitral-aortic intervalvular fibrosa and fibrous trigones obtained from uniaxial testing. The best-fitted material parameters of the animal aortic tissues are listed in Table 5.1.

Table 5.1 Material parameters of the animal aortic tissues.

Specimen			**C_{01}**	**K_1**	**K_2**	**C_{10}**	**κ**	**Theta (°)**	**D**
Species	**Age**	**Tissue**							
Ovine	1-2yo	Aorta	0.6267	2.2290	0.4252	13.4067	0.3333	0.0001	0.0005
Ovine	1-2yo	Sinus	0.8019	1.4952	0.3390	8.6251	0.1696	10.5777	0.0005
Ovine	1-2yo	Leaflet	11.5241	11.6636	41.2337	0.3602	0.1065	29.3247	0.0005
Porcine	6-9mo	Aorta	1.0156	1.2185	2.0183	15.9920	0.3333	0.0001	0.0005
Porcine	6-9mo	Sinus	1.2654	0.8909	2.2239	9.0375	0.3333	0.0001	0.0005
Porcine	6-9mo	Leaflet	11.1375	34.6759	74.2008	1.5021	0.3333	0.0999	0.0005
Porcine	2yo	Aorta	2.0084	0.2646	11.0050	5.5707	0.3333	0.0002	0.0005
Porcine	2yo	Sinus	1.1239	1.0727	0.7509	5.3232	0.3333	0.0011	0.0005
Porcine	2yo	Leaflet	7.9921	4.8561	24.6861	1.1111	0.0396	0.0473	0.0005

5.2.5 Simulation Setup

The stent model had a height of 14.3 mm and a thickness of 0.5 mm, which was generated using published data in the literature to stimulate the Edwards SAPIEN stent geometry (Figure 5.5). The stent was modeled with the properties of 316 stainless steel with a Young's modulus of 193 GPa, a Poisson ratio of 0.3, and initial yield stress of 340 MPa [73]. The mechanical response of a fluid-filled balloon expansion was modeled by a surface-based fluid cavity method in Abaqus/Explicit, which was capable of simulating the coupling between the deformation of the balloon and the fluid inside with uniform properties and state. The valve was positioned such that the aortic annulus bisected the stent. The dynamic balloon expansion process was simulated to complete in 1 second, which resulted in a constant flux rate of 16 ml/s. Friction coefficient between TAV stents and aortic roots was assumed to be 0.1 based on the studies by Mummert et al. [65] and Vad et al. [137]. Contact radial and shear forces between the stent and aortic root were output from Abaqus FEA; and were calculated by summing the normal and shear contact forces of the node set that represented the outside surface of the stent.

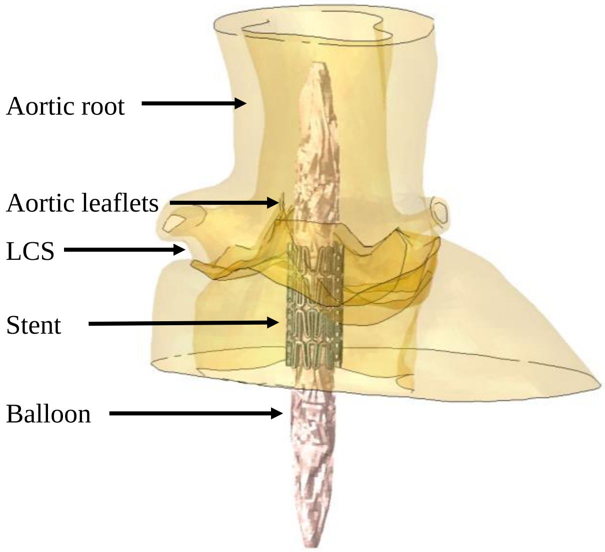

Figure 5.5 Finite element simulation setup for the balloon-expandable stent expansion inside the 1-2 years old ovine aortic root.

5.2.6 In Vitro Structural Experiments

In vitro structural experiments [65] were conducted previously in our lab to quantify the stent radial expansion force, pullout force and coefficient of friction at the stent-tissue contact interface. Self-expanding Nitinol stents were fabricated using Nitinol wires obtained from Memry Corporation, Bethel, CT (meets ASTM F2063-05). The shape of the stent was cylindrical with a height of 16 mm and a diameter of 26 mm. The stent had 4 strut cells in the axial and 12 in the circumferential directions. The stent geometry was set by using a heat treatment of 8 minutes at 500°C. Stent crimp tests (Figure 5.6) were performed on a Tinius Olsen uniaxial testing apparatus (Model H50K-S, Horsham, PA) to quantify the relationship between the stent diameter and the radial expansion force of the Nitinol stents.

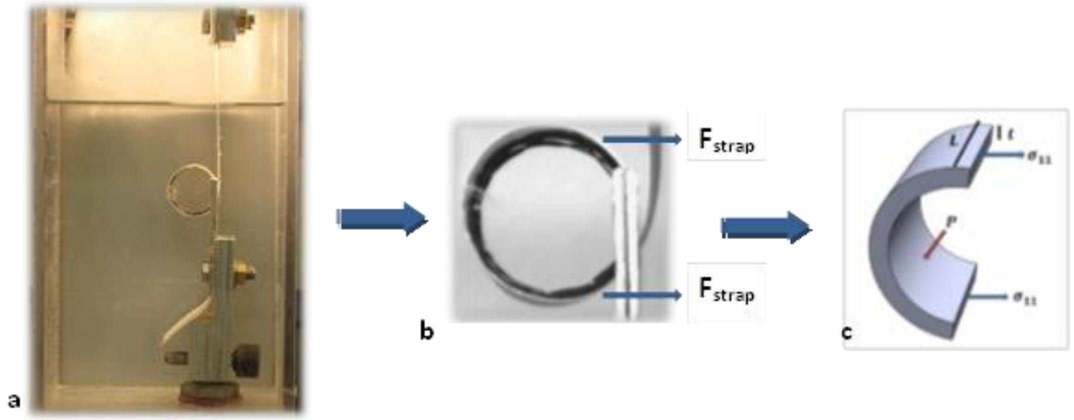

Figure 5.6 (a) Stent crimp experimental setup to measure hoop force at body temperature (37°C). (b) Hoop force exerted on transcatheter valve stent from Dacron strap. (c) Free body diagram of stent cross-section [65].

Then, 6–9 months old porcine and 1-2 year old ovine hearts with an aortic annulus size of 21 mm were obtained for the stent deployment tests and submerged in a clear-sided tank filled with a Ca2+-free and glucose-free Tyrode solution. A Nitinol TAV stent was deployed into the aortic root so that the aortic annulus was approximately aligned with the middle of the TAV stent height (Figure 5.7). The stent diameter was measured by an ultrasound probe (75L60EA Ultrasonic Transducer, Mindray Bio-Medical Electronics Co.), which could capture 2-dimensional cross-sectional images of the TAV stent deployed inside the aortic root at the tissue-stent contact equilibrium position. The final diameter of the deployed stent was used to deduce the radial force based on the experimental data of the stent-crimping tests. Additionally, the TAV stent was then pulled out of the intact valve and the pullout force was recorded. The results from stent pullout tests were also used to calculate frictional coefficient between the stent and tissue. The structural experimental data (especially the radial contact forces and pull-out forces) were compared to the results of TAV deployment simulations using animal models.

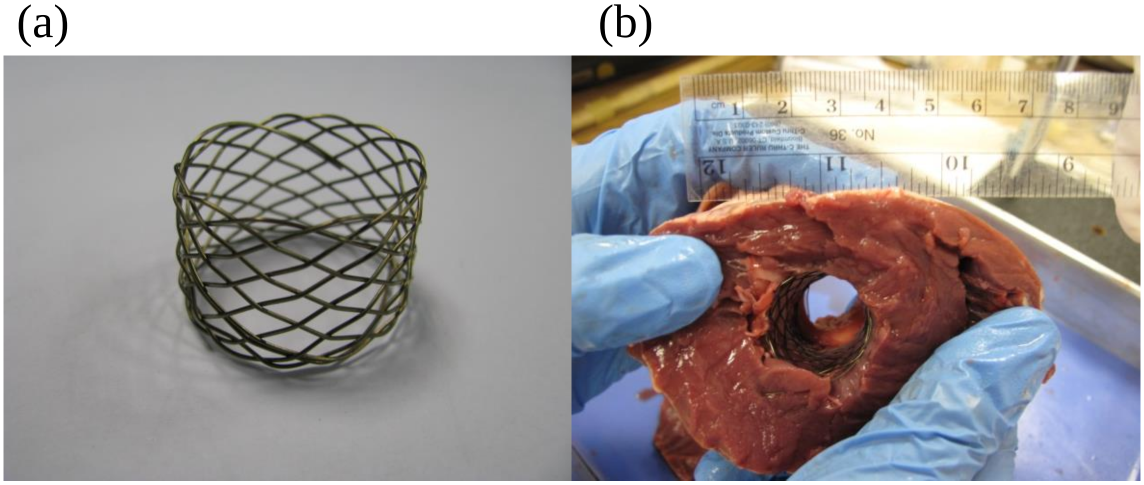

Figure 5.7 (a) A Nitinol TAV stent and (b) stent deployment inside a porcine aortic root.

5.3 Results

5.3.1 Anatomic Features of the Animal Aortic Roots

An examination of the specimens was performed before the micro-CT scan to evaluate the anatomic structures of the 1-2 years old ovine, the 6-9 months and the 2 years old porcine aortic roots. A short coronary ostium height (from 4 to 8 mm) was observed in all three aortic roots. Compared to the 1-2 years old ovine and the 6-9 months porcine aortic roots, the sinuses of the 2 years old porcine aortic root have a more distinct bulging shape. The sinotubular junction of the 1-2 years old ovine and the 2 years old porcine aortic roots is smaller than the aortic annulus, while the sinotubular junction diameter in human hearts is consistently larger than annulus diameter [45, 46, 52, 113, 117]. Thicker left ventricular wall was found in the three animal hearts compared to human hearts. Moreover, the right coronary leaflet is attached to the left ventricle in ovine and porcine hearts (Figure 5.3), as opposed to the bottom of the right coronary sinus in human hearts. The coronary artery lumen diameter of the ovine and porcine aortic roots gradually increases as the coronary artery connects to the sinus (Figure 5.3), whereas in human the lumen diameter is more constant (Figure 5.3).

5.3.2 Simulation Results of TAVI Procedure Using Animal Models

The deformed aortic roots at the maximum stent deployment are shown in Figure 5.8a, Figure 5.8b, and Figure 5.8c for the 1-2 years old ovine, the 6-9 months and the 2 years old porcine hearts, respectively. Degree of ellipticity of the annulus was evaluated for each model by calculating the ratio of minimum annulus diameter to maximum annulus diameter. The degree of ellipticity of the aortic annulus (0.99, 0.96, and 0.96) was approximately 1 for all three animal models, which suggested that the stent was expanded uniformly in the radial direction inside the aortic roots. Although the deformed leaflet free edges of the three models were generally higher than the corresponding coronary ostia, due to the large funnel-shaped coronary artery lumen, no coronary obstruction was observed. When the balloon was filled with the defined volume of fluid, the average diameters of the deformed stent were 22.8 mm, 23.0 mm, and 23.1 mm for the 1-2 years old ovine, the 6-9 months and the 2 years old porcine hearts, respectively.

Contact forces in the radial direction were 60 N, 65 N, and 75 N for the 1-2 years old ovine, the 6-9 months and the 2 years old porcine hearts, respectively. Contact forces in the axial direction were 5.4 N, 5.8 N, and 6.4 N for the three animal models.

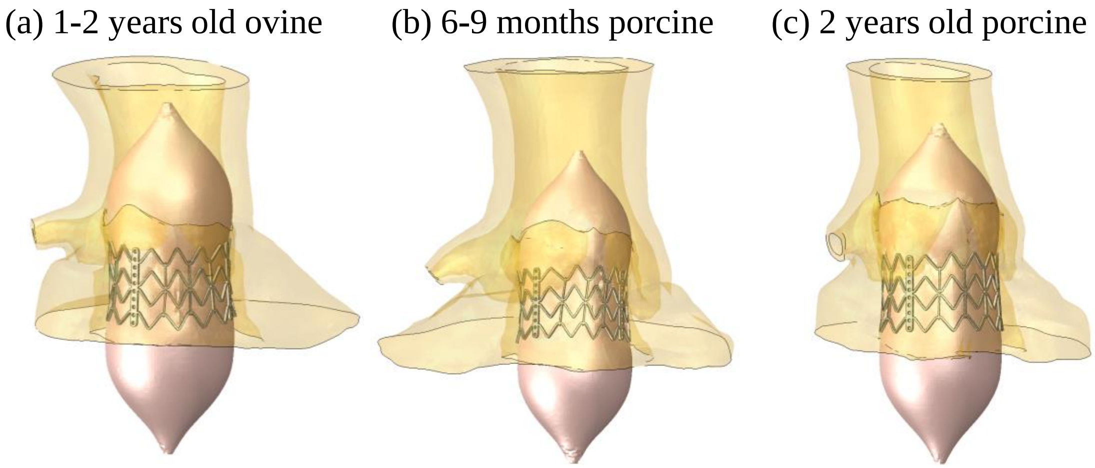
(a) 1-2 years old ovine
(b) 6-9 months porcine
(c) 2 years old porcine

Figure 5.8 The deformed aortic roots of (a) the 1-2 years old ovine, (b) the 6-9 months, and (c) the 2 years old porcine hearts at the maximum stent deployment.

5.3.3 Results of In Vitro Structural Experiments

A stent crimp experiment was performed to quantify the radial expansion force of the Nitinol stents. Subsequently, the aortic root tissue response was obtained from the aortic root-stent expansion tests of porcine and ovine hearts. During the stent expansion process, the aortic root exhibited nonlinear responses, becoming less compliant with increased dilation. The 6-9 months porcine samples demonstrated similar deformation and radial forces to 1-2 years old ovine samples. When 6-9 months porcine aortic roots with an annulus of 21 mm were dilated into a diameter of 23 mm, the radial expansion force was approximately 60 N (Figure 5.9). Whereas, when 1-2 years old ovine aortic roots with an annulus of 21 mm were dilated into a diameter of 23 mm, the radial expansion force was roughly 58 N. Furthermore, stent pullout tests showed that when the stents were deployed inside the aortic roots with an annulus of 21 mm, the force to dislodge the stent in the axial direction was in the range of 4.9-6.3 N.

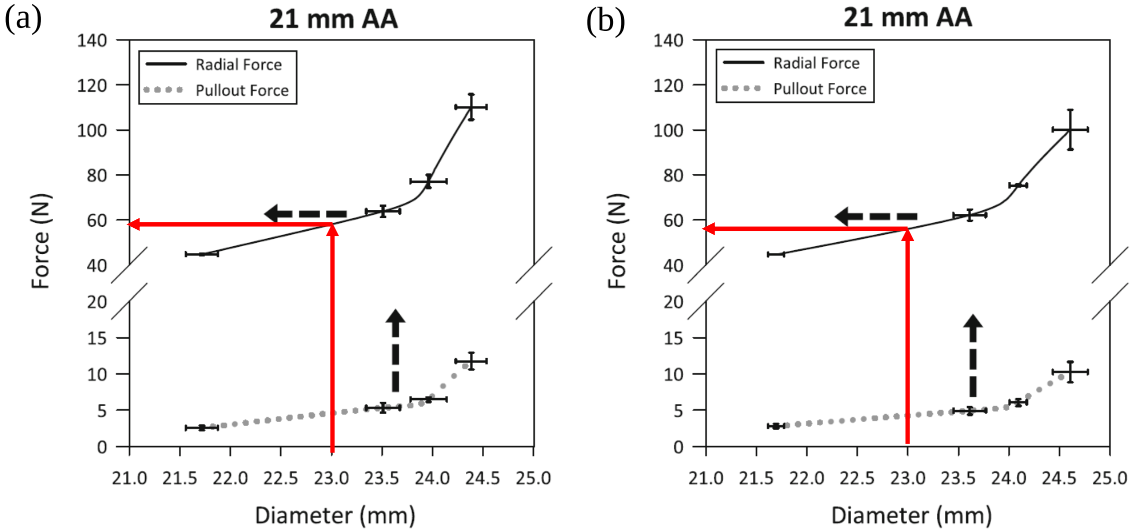

Figure 5.9 Biomechanical tissue behavior of the aortic root tested in (a) porcine and (b) ovine tissue grouped according to aortic annulus (AA) diameter sizes 21 [65].

5.3.4 Comparison between FE Simulations and In Vitro Experiments

Simulations of TAV stent deployment inside the porcine and ovine hearts demonstrated that the contact radial forces extracted from FE models were similar (60 N vs. 58 N for the 1-2 years old ovine hearts, 65 N vs. 60 N for the 6-9 months old porcine hearts) to the in vitro experimental results. When the frictional coefficient determined from in vitro experiments was used in the simulations, contact shear forces of the aortic root FE models were also comparable to those in the structural experiments. In addition, for the in vitro structural experiments, ultrasound images of the deployed stent inside porcine and ovine aortic annulus revealed that the deformed stents at different height levels were highly circular. Similar circularity was also observed in the deformed stent profiles from the simulations.

5.4 Discussion

5.4.1 Validation of the FE Modeling Method of TAVI Procedure Using Animal Models

Even though significant experience has been gained on the TAVI, there are still severe adverse events associated with the procedure. Currently, there is no available tool to predict and prevent these adverse events. Successful TAV deployment and function depend heavily on the tissue-TAV interaction. Thus, a reliable prediction of the biomechanical interaction between native calcified tissue and device in TAVI is essential for the success of this procedure. Although computational models have been used to investigate the biomechanics of the TAVI procedure, the validation of the models was limited due to the availability of the direct in vivo biomechanical measurements from TAVI patients. Therefore, the main purpose of the study was to use FE simulations of TAVI procedures in animal models to validate the methodology that was established in our previous research [75, 80, 81].

Comparisons between the simulations and in vitro experiments using 1-2 years old ovine and 6-9 months old porcine hearts showed that the simulations of TAV deployment in animal models could quantitatively replicate the realistic biomechanical interaction in terms of tissue-device contact forces and ellipticity of the deformed annuli. It should be noted that tissue-prosthesis interaction forces were quantified when the diameters of the simulated and in vitro aortic annuli (hence the overall aortic structural deformation) were approximately the same. As a result, the correlation between the two different types of stents used in the study, i.e. self-expandable Nitinol stents for the in vitro structural experiments vs. balloon-expandable stainless steel stents for TAVI simulations, was established based on the deformed tissue response. The validation results showed in this chapter indicated that our FE modeling methodology of TAV deployment might be potentially utilized to create accurate FE models of TAV deployment and might generate useful information for pre-procedural planning of TAVI.

5.4.2 The Use of Animal Models in TAVI Clinical Feasibility Studies

Although several animal models have been used in the TAVI clinical feasibility studies, the detailed quantification of mechanical properties of the different models was inadequate to determine which substitute could best approximate clinical TAVI patients. Accordingly, this chapter attempted to compare the difference in structural mechanical responses during TAV deployment among various common animal models.

Our results showed that based on the contact radial forces and stent pullout forces from both the in vitro experiments and simulations, the structural compliance of the aortic annuli of the 1-2 years old ovine and 6-9 months old porcine hearts were comparable, whereas the annuli of the 2 years old porcine hearts exhibited stiffer mechanical properties than the other two animal groups. The shear force between the stent and tissue, which was the resistance of the stent from migrating into the aorta or left ventricle, was in the range of 4.9-6.4 N determined from both the in vitro experiments and simulations. To prevent stent migration, the shear force should be higher than the retrograde force (approximately 6 N) acting on the closed valve, which was quantified in the studies by Dwyer et al. [83] and Sun et al. [70]. Clinical feasibility studies using juvenile animal models [156, 158] showed that stent migration occasionally occurred during the stent deployment. This adverse event was thought to be caused by the fact that animal annulus was highly elastic and not calcified, while the irregular surface of the aortic valve calcification could help anchor the valve in clinical TAVI patients. Furthermore, the examination of the anatomic features of the animal aortic roots showed that they generally had low coronary ostium heights, which could contribute to the occasional coronary obstruction in the clinical feasibility studies. Consequently, when the stent was positioned relatively low to avoid coronary obstruction in animal aortic roots, supra-skirtal regurgitation was frequently noted in those studies.

Since 2 years old porcine hearts had stiffer material properties and more developed anatomical structures than the other 2 groups, they could be a closer approximation to real TAVI patients. The use of the 2 years old porcine hearts in the clinical feasibility studies might reduce the rate of the aforementioned adverse events. Moreover, our findings in this chapter with regards to the difference in the mechanical properties between commonly-used animal models were generally consistent with biaxial and aortic root inflation testing results [53, 54, 64, 159, 160] that were in the literature.

5.4.3 Comparison of Animal Models to Clinical TAVI Patients

Biomechanical characteristics between tissue and prosthesis in clinical TAVI patients were previously reported in our studies [75, 80, 81]. The contact normal and shear forces of the TAV deployment inside animal models were lower than those of the clinical TAVI patients, while the maximum principal stresses of the aortic tissue were also lower in animal models. Additionally, due to the presence of aortic calcification in the TAVI patients, their annuli displayed a more elliptical shape than those of the animal models.

5.4.4 Limitations

It was challenging to preserve the aortic tissue due to the length of time of the micro-CT scanning. Damage and permanent deformation to the aortic wall and leaflets was usually observed after stent deployment tests. Consequently, aortic tissues from the same heart were not reused for the in vitro structural experiments, micro-CT imaging, and mechanical testing. Moreover, material parameters used for the FE models were averaged properties over 10 biaxial test samples in lieu of specimen-specific material properties. Since there is a lack of experimental data, the material properties of left ventricle obtained from our previously study [75] was used for all the simulations. Although frictional coefficient between the stent and tissue could depend on the stent design and material, same coefficient was assumed for the in vitro experiments and FE simulations.

5.5 Summary

The objective of this chapter was to validate the FE modeling method that was developed in our previous research by using FE simulations of TAVI procedures in animal models and in vitro structural experiments. The comparison of tissue-device contact forces between computational and experimental data demonstrated that the FE simulation of TAV expansion in animal models could reproduce the mechanical response of in vitro structural experiments, which indicated that our FE modeling methodology might be potentially utilized to create accurate FE models of TAV deployment and generate useful information for pre-procedural planning of TAVI. Also, this chapter attempted to quantify the discrepancy in the mechanical properties between various animal models at the structural level. Our results showed that 2 years old porcine hearts might be a closer approximation to clinical TAVI patients compared to 1-2 years old ovine and 6-9 months old porcine hearts.

CHAPTER 6

PARAMETRIC STUDIES OF TAV DEPLOYMENT STRATEGIES

In previous chapters, a methodology was developed to model TAVI stent deployment at a patient-specific level. However, it is still unknown how reliable the simulations results are and how sensitive the models are to the input parameters. Furthermore, the clinical application of the current research is to use simulation-based analysis to find optimal TAVI implantation strategies and to minimize TAV deployment-related complications. For example, the fluid volume information obtained from the balloon expansion simulation could be used to adjust injection volume to avoid adverse events such as PVL and aortic rupture. Similarly, different stent deployment heights could be easily simulated before the procedure is completed.

Therefore, in this chapter, parametric studies were conducted to examine the influence of the model input such as material properties, balloon volume, stent deployment height, calcification location, and different methods to simulate balloon inflation on TAVI simulation results and subsequently the potential clinical complications such as PVL, annular rupture, and coronary artery occlusion.

6.1 Introduction

The TAVI case with aortic rupture that was described in Chapter 5 was used as the baseline model. The model input was perturbed to represent the potential scenarios in clinical TAVI settings. The TAV deployment was simulated and compared to clinical observations of the baseline case. The simulation results that were used to quantify the changes due to different input parameters were biomechanical characteristics such as the deformed aortic root and stent geometries, contact forces in radial and axial directions, and stress.

6.2 Methods

6.2.1 Biomechanical Characteristics of TAVI Simulation

Based on the potential failure modes of the TAV observed during clinical trials [161-167], the following performance measures are devised to evaluate the aortic root-TAV interaction:

i) Interactive contact forces between the TAV stent and the aortic root. This is an important measure, since elevated radial contact force may cause tearing of the aortic wall and low radial force can cause paravalvular leakage. Insufficient axial contact force, when it is smaller than the migration/distraction force (i.e., the peak aortic pressure multiplied by valve orifice area) [168], may result in device migration. The radial and axial forces are denoted by RF and AF respectively, and expressed as: $RF = \sum_{i=1}^{n_s} rf_{i,post}$ and $AF = \sum_{i=1}^{n_s} af_{i,post}$, where ns is the total number of nodes of the stent and $rf_{i,post}$ and $af_{i,post}$ are the radial and axial contact forces at each stent node after TAV deployment.

ii) Peak stresses in the aortic root wall. Elevated peak stress in the vessel wall may trigger tissue growth and remodeling, and lead to tissue degeneration or aortic dilatation. It has been shown that bioprosthetic heart valve leaflet structural deterioration and calcification are correlated with regions of high stresses [169, 170].

iii) Coronary ostia occlusion index. This index is used to evaluate how close the aortic leaflet/TAV stent is to the coronary ostia following TAV deployment. As clinically observed, impairment of coronary flow can lead to myocardial infarction. The coronary ostia occlusion index (COOI) is defined as $COOI = (X_{L,post} - X_{CO,post})/D_{CO}$ where $X_{L,post}$ and $X_{co,post}$ are the height of the center of the leaflet free edge and the height of the coronary ostium after TAV deployment, respectively (Figure 6.1). $X_{L,post}$ will be measured as the axial (vertical) distance from the center of the leaflet free edge to the aortic annulus plane. $X_{co,post}$ will be measured as the axial (vertical) distance from the inferior border of the coronary ostium to the aortic annulus plane. D_{co} is the diameter of the coronary artery lumen. This equation calculates the minimal distance between leaflet and coronary arterial ostia. When COOI > 0, one coronary ostium has the potential of being blocked by a leaflet.

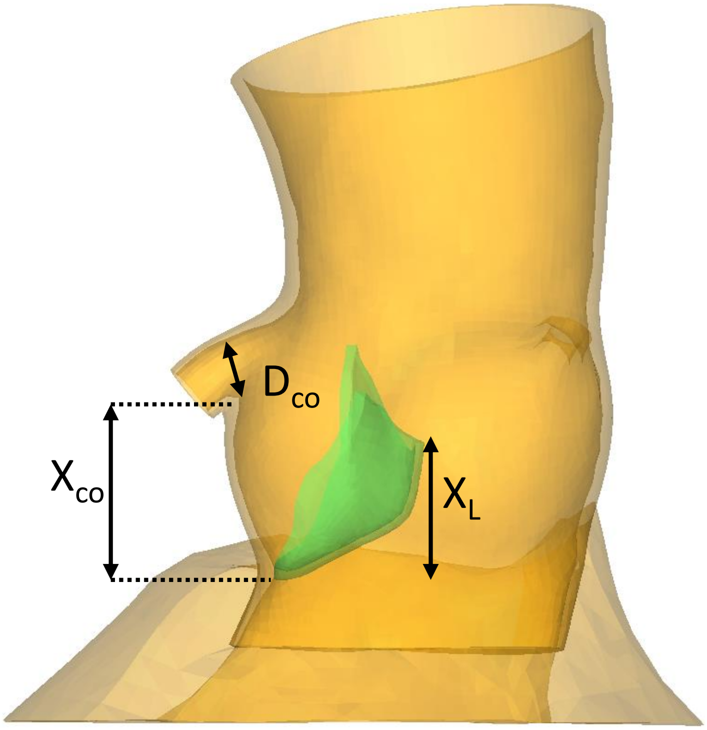

Figure 6.1 Calculation of coronary ostia occlusion index COOI.

iv) Paravalvular leak index. Due to heterogeneity of the stenotic aortic root, a deployed TAV may not be entirely in contact with the patient's root wall, especially when regions of calcification exist. To quantify the gap between the TAV stent and the root, the paravalvular leak index (PVLI) will be used, which is defined as: $PVLI = (A_{root,post} - A_{stent,post})/A_{stent,post}$, where, $A_{stent,post}$ is the cross-sectional area of the region bounded by the stent's outer perimeter at the aortic annulus; and $A_{root,post}$ is the cross-sectional area of the aortic annulus after TAV deployment (Figure 6.2). When PVLI > 0, there is a potential of paravalvular leakage.

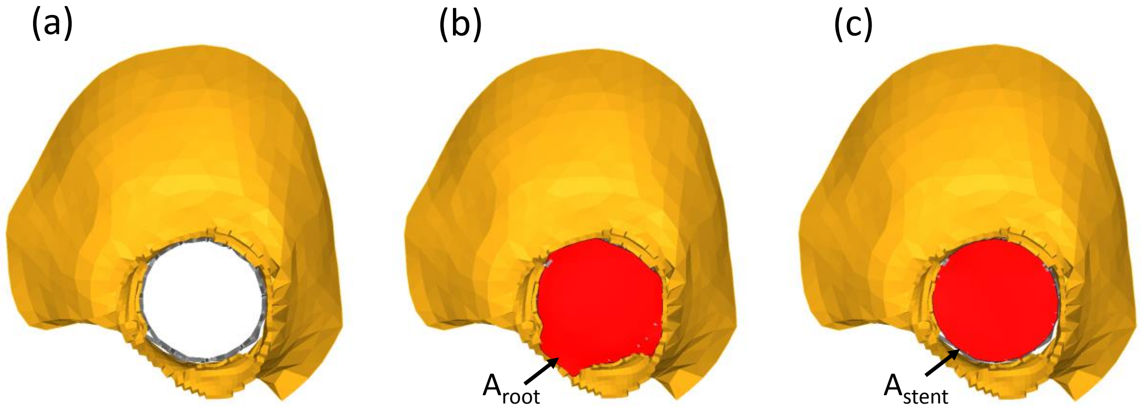

Figure 6.2 Calculation of paravalvular leak index PVLI (a) post deployment aortic root geometry (b) cross-sectional area (in red) of the deformed aortic annulus and (c) cross-sectional area (in red) of the deformed stent.

6.2.2 Impact of the TAVI Deployment Variables

The effects of the model input parameters on the TAV deployment simulation results and the eventual clinical outcomes were investigated in parametric studies. The model inputs that were examined in this section are (i) material properties of the human heart tissue, (ii) the balloon inflation volume, (iii) the TAV stent implantation depth, (iv) calcification location, and (v) methods of balloon expansion simulations.

i) For the baseline model, load-controlled biaxial tests of healthy human aortic valve leaflets, aortic sinuses, ascending aorta and mitral leaflets obtained from a 96-year-old female cadaver heart were conducted. It was assumed that the material properties of the biaxial-tested human heart tissue were similar to those of the 94-year-old female TAVI patient. However, since material properties of human aortic tissues could be varied even among patients with same age and gender due to different health conditions and life styles, material properties of human aortic root tissue from other cadaver hearts (an 80-year-old female and an 88-year-old female) tested in our lab were used to investigate the sensitivity of FE simulations to material parameters. The material parameters of the 3 patients used in the study are listed in Table 6.1 and shown in Figure 6.3.

Table 6.1 Material parameters of the human heart tissues.

Specimen			**C_{01}**	**K_1**	**K_2**	**C_{10}**	**κ**	**Theta (°)**	**D**
Patient	**Age**	**Tissue**							
Patient 1	96-yo	Aorta	22.8094	0.1393	117.4753	0.6549	0.0000	0.0001	0.0005
		Sinus	34.5907	146.1744	61.5390	0.6559	0.1459	37.5053	0.0005
		AL	40.5289	83.6776	86.2279	0.3258	0.3333	32.9131	0.0005
		AML	77.9131	23.8401	150.1645	0.2955	0.3333	89.9998	0.0005
Patient 2	88-yo	Sinus	18.7420	4.8089	34.7871	1.0202	0.0337	0.1127	0.0005
		AL	43.0389	81.5896	30.7071	0.4183	0.3333	40.3099	0.0005
		AML	67.7875	42.8614	100.0000	0.5719	0.0000	89.9999	0.0005
Patient 3	80-yo	Aorta	4.4270	0.4098	23.0293	3.6276	0.3333	89.9999	0.0005
		Sinus	15.0206	10.8731	44.0452	1.6029	0.0000	0.0012	0.0005
		AL	74.3880	16.5630	99.8700	0.0572	0.1485	21.4358	0.0005
		AML	18.7048	7.8689	24.4632	0.0359	0.1109	29.0297	0.0005

Footnote: AL = aortic leaflet, AML = anterior mitral leaflet

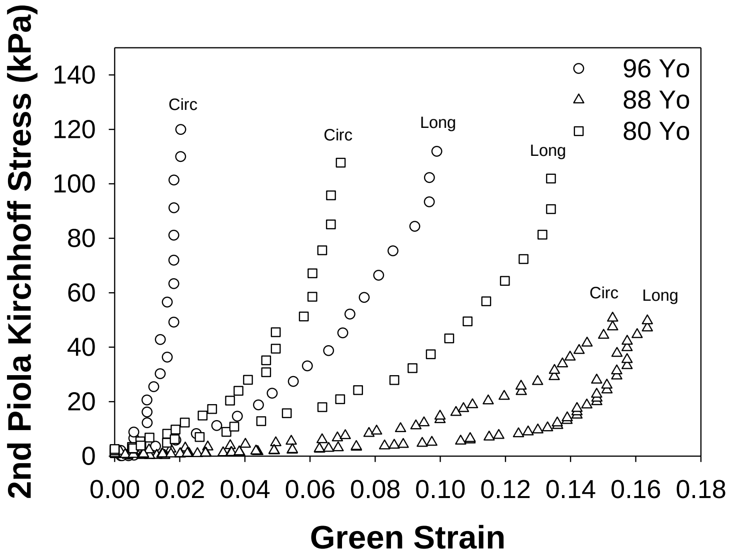

Figure 6.3 Material properties of the human aortic sinuses for the parametric study

ii) For TAVI patients with high risk of aortic annulus rupture like the baseline case described in Chapter 5, special care should be taken to avoid aggressive and full balloon dilatation. In this section, besides the nominal volume (16 cc), the balloon inflation with nominal volume ±1 cc and ±2 cc was simulated to find the proper degree of balloon expansion for the TAVI procedure.

iii) Positioning the valve prosthesis too high or low may result in embolization, coronary obstruction, or PVL. Since it is challenging to precisely control the TAV stent implantation depth relative to the annulus during the deployment, parametric study of the FE model could provide useful information on how much the variation in the stent implantation depth could affect the final deployment results. The baseline height was defined as 50% of the stent height above the annulus plane. Moreover, the simulations with 10% and 90% of the stent height above the annulus plane were completed. The results from the additional simulations were compared to the baseline model to examine the effects of boundary conditions.

iv) To investigate the impact of spatial distribution of calcification on the aortic root rupture potential, the FE model of this patient was perturbed, and two additional aortic root geometries (Figure 6.4) with different calcification locations and distributions were analyzed and compared in this chapter. Thus, we had: Scenario A - the original calcification condition obtained from MSCT images. Scenario B - the calcification spot on the interior of the left coronary sinus was removed. We wanted to evaluate if the aortic root rupture was associated with that calcification spot, i.e., if the rupture could still occur without the calcification. Scenario C – with the Scenario B condition, a calcification spot was added to the interior of the right coronary sinus, which was in a similar volume and location to the calcification in left coronary sinus; at the level of the right coronary sinus between the ostium of the right main stem and the aortic annulus entering the myocardium. With Scenario C, we wanted to examine if there was a difference in the rupture potential when the calcification was placed at either left or right coronary sinus.

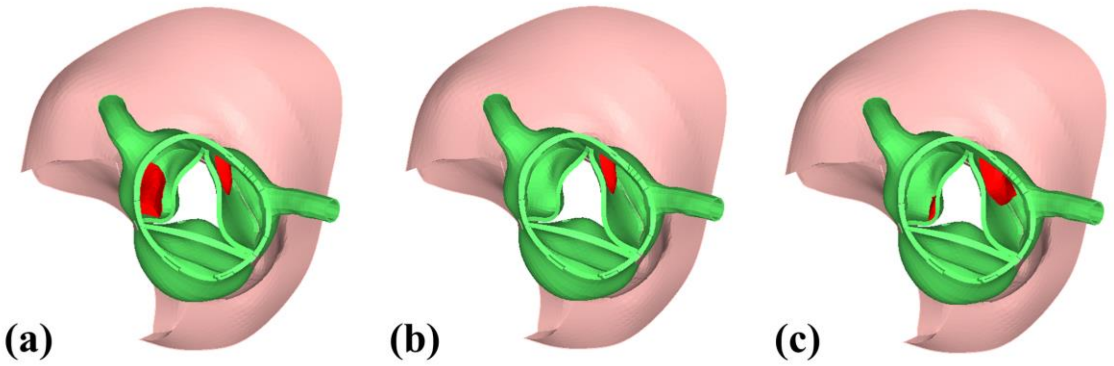

Figure 6.4 Top views of the 3 aortic root initial geometries with different calcification locations and distributions (red elements indicate calcification).

v) FE analysis has been used as a tool to simulate the TAVI procedure and investigate the mechanics during TAV deployment [74-76]. However, previous studies have not assessed the interaction between the aortic root and stent due to transient non-uniform balloon expansion. The common methods of simulating the balloon expansion process were to prescribe displacement field or to apply uniform balloon internal pressure. The assumption of the displacement control method was that the balloon-expandable stent is almost uniformly expanded and circular in shape, whereas the reality is that the deformed stent geometry could still vary with the aortic calcification distribution [171]. By applying uniform pressure inside the balloon, the phenomenon of stent foreshortening and dogboning shapes could be produced. However, since the annulus size and aortic calcification volume are different for individual patients, it is challenging to determine the magnitude of the ultimate internal pressure that is used to deploy the stent to a designed diameter. Therefore, the realistic balloon expansion behavior might not be characterized due to the assumptions used in the aforementioned methods.

To determine the effects of loading conditions on simulation results, three balloon expansion methods (Figure 6.5) were used in this chapter: (a) fluid controlled, (b) displacement controlled, and (c) pressure controlled balloon expansion. For the fluid controlled simulation, the balloon expansion process was regulated by a constant flux rate of 16 ml/s. For the displacement controlled simulation (Figure 6.5a), a displacement field was prescribed to a cylinder in its radial direction so that it could expand the TAV stent to an outer diameter of 23 mm. For the pressure controlled simulation, the same balloon and TAV stent initial geometry as the fluid controlled simulation was utilized. A linear pressure input with a peak value of 3.5 atm, which equaled the peak pressure at the end of the fluid controlled simulation for this patient, was applied to the interior of the balloon.

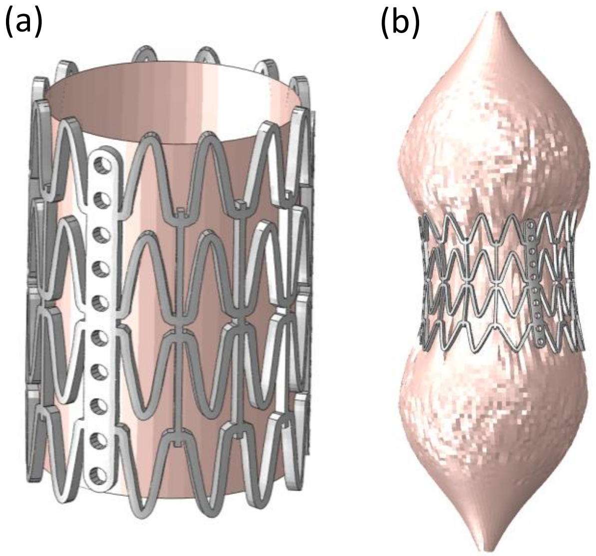

Figure 6.5 (a) Finite element model of the TAV stent and a simplified balloon for the displacement controlled method. (b) Finite element model of the TAV stent and balloon deployment for the surface based fluid cavity and pressure controlled methods.

6.3 Results

6.3.1 Baseline Case Presentation

As described in Chapter 5, a 94-year-old female patient with a tricuspid aortic valve and an annulus size of 19.6 mm was referred for TAVI procedure. Echocardiography revealed severe AS in the non-coronary leaflet as well as the interior of the aortic root; only the left coronary leaflet could open during cardiac cycles. The pre-procedural MSCT scans showed heavy calcification on the non-coronary leaflet, and one large calcified spot on the interior of the left coronary sinus at the level between the ostium of the left main stem and the aortic annulus entering the myocardium. A size 23 Edward SAPIEN TAV was implanted. During TAVI procedure, aortic root tearing happened and visualized below the left main coronary artery.

6.3.2 Simulation Results of the Baseline Case

The results of the baseline simulation are listed in Table 6.2. The simulation of the TAVI procedure revealed that asymmetric distribution of the aortic calcification lead to asymmetric expansion of the TAV stent with respect to the center of the aortic root. The TAV stent in the non-coronary sinus region was partially expanded, compared to fully expanded stent in the less calcified left coronary sinus region. The calcified spot on the interior of the left coronary sinus was displaced by the TAV stent, causing stress concentration at the bottom of the left coronary sinus and consequently the aortic rupture. High stress and strain were generally observed at the aortic tissue where it contacted the calcification and stent struts. Contact radial force between the TAV stent and aortic root reached 109 N, when the stent was fully deployed. Rupture of the aortic root at the bottom of the left coronary sinus occurred at roughly 94 % of the balloon volume. The balloon pressure at full deployment was 3.5 atm. Rupture location in the simulation was the same as that in the clinical case. Both the coronary ostia occlusion index COOI and paravalvular leak index PVLI were 0, which suggested low potential occurrence of the 2 adverse events.

6.3.3 Simulation Results of Parametric Study on Material Parameters

The results of parametric study on material parameters are listed in Table 6.2. It should be noted that although patient specific material properties were used in this chapter, they were not necessarily representative of the trend of aging human material properties. As shown in Figure 6.3, material properties of the 88-year-old female and 80-year-old female were the more compliant than those of the 90-year-old patient. Consequently, no rupture was observed for the simulations with those two patients. In addition, the coronary ostia occlusion index COOI and paravalvular leak index PVLI, and the contact forces between the stent and root at the maximum expansion were similar among the three simulations.

6.3.4 Simulation Results of Parametric Study on Balloon Volume

The results of parametric study on balloon volume are listed in Table 6.2. When the balloon was under-inflated below the nominal volume, the deformed stent had a more circular shape at the aortic annulus. On the other hand, the deformed stent had an elliptical shape due to the heavy calcification on non-coronary leaflet, when the balloon was inflated to the nominal volume. As a result of under-inflation, the cross-sectional area of the deformed stent was smaller than the aortic root at the annulus, there was a small potential of PVL when the injected fluid volume was 14 or 15 cc. However, when the balloon was under-inflated by 2 cc, no rupture was observed at the left coronary sinus. The peak stress on the aortic wall gradually increased when the injected fluid volume in the balloon was increased from 14 cc to 16 cc. The slight decrease in peak stress on the aortic root when the balloon volume was 17 and 18 cc could be explained by the fact that over-expansion of the balloon caused elevated stress and subsequently high-stress elements were deleted from the model. Additionally, as the injected fluid volume increased for the balloon, there was an increase in contact forces between the stent and tissue in both the radial and axial directions.

6.3.5 Simulation Results of Parametric Study on Stent Height

The results of parametric study on stent height are listed in Table 6.2. In either case where 90 % or 10 % of the stent height was above the aortic annulus when the stent was deployed, the contact forces between the stent and tissue, peak stress on aortic wall, and the risk of coronary ostium occlusion and PVL were comparable to those of the baseline case. The only noticeable change for the different stent deployment heights was that the aortic rupture was more extensive when the stent was deployed higher, which lead to the stent over-expansion in the softer aortic sinus region compared to the stiffer annulus region.

Table 6.2 Summary of the simulation results of parametric studies on TAV deployment strategies.

	Radial Contact Force (N)	**Axial Contact Force (N)**	**Peak Stress (MPa)**	**COOI**	**PVLI**	**Rupture Location**
Baseline	109	10	3.30	0.0	0.0	LCS
Material Parameters						
80 YO Female	110	10	3.22	0.2	0.0	No Rupture
88 YO Female	113	10	2.38	0.3	0.1	No Rupture
Balloon Volume						
14 cc	33	3	1.48	0.0	0.1	No Rupture
15 cc	64	6	2.15	0.2	0.1	LCS
17 cc	197	17	3.28	0.3	0.0	LCS and RCS
18 cc	265	22	2.16	0.2	0.0	LCS and RCS
Stent Height						
High	115	10	2.53	0.3	0.0	LCS and RCS
Low	114	10	2.78	0.3	0.0	LCS

6.3.6 Simulation Results of Parametric Study on Calcification Location

For Scenario B, the deformed aortic root of the patient after the maximum stent expansion is shown in Figure 6.5. Similar asymmetric expansion of the TAV stent inside the aortic root was observed as a result of the calcification in the non-coronary and right coronary leaflets. However, the aortic root did not rupture at the bottom of the left coronary sinus. Contact force between the stent and aortic root at full TAV stent deployment was comparable to that of the original geometry.

For Scenario C, deformation of the TAV stent inside the aortic root was similar to the results from Scenario A and B. However, aortic root rupture was observed at the bottom of the right coronary sinus (Figure 6.6), due to the displacement of the calcified spot on the interior of the right coronary sinus. Contact force between the stent and aortic root was also comparable to that of the original geometry at the full expansion.

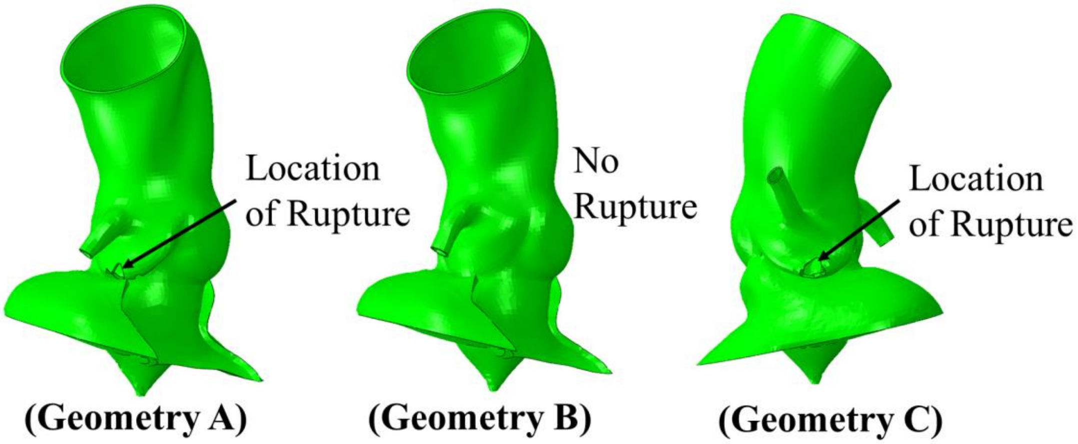

Figure 6.6 Deformed aortic roots after TAV implantation procedure showed possible aortic ruptures due to different locations and distributions of aortic calcification.

6.3.7 Simulation Results of Parametric Study on Balloon Expansion Methods

i) Deformed TAV Stent Geometry. The top views of the deformed TAV stents obtained from the three different balloon expansion methods are illustrated in Figure 6.7. For the fluid controlled method, the TAV stent was deformed asymmetrically with respect to the axis of the aortic root due to the unequal distribution of the aortic calcification. The TAV stent was partially expanded in the non-coronary sinus region, while it was fully expanded in the other regions. For the displacement controlled simulation, a uniform radial expansion along the stent height was observed. The deformed stent geometry from the pressure controlled simulation was similar to that from the fluid controlled simulation, which also exhibited a slight dogbone shape.

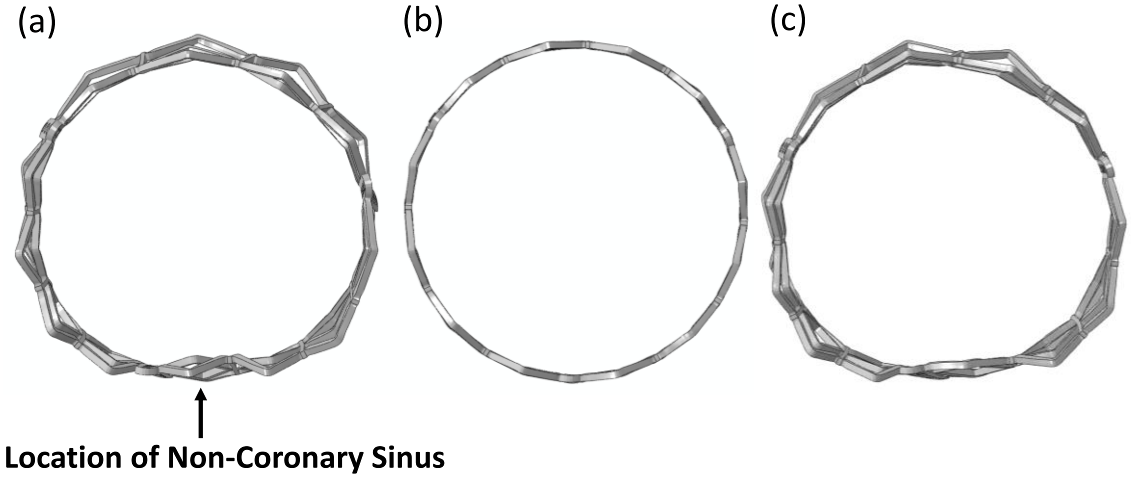

Figure 6.7 Top views of the deformed shapes of the TAV stent obtained from the (a) fluid controlled, (b) displacement controlled, and (c) pressure controlled balloon expansion methods.

ii) Deformed Aortic Root Geometry. The deformed geometries of the aortic root obtained from the three different balloon expansion methods are plotted in Figure 6.8. For the fluid controlled simulation, the calcified spot on the interior of the left coronary sinus was displaced by the TAV stent, causing stress concentration at the bottom of the left coronary sinus. High stress and strain were generally observed at the aortic tissue where it contacted the calcification and stent struts. Rupture location in the simulation was the same as observed clinically. For the displacement and pressure controlled simulations, more extensive rupture was found at the bottom of both the left and right coronary sinuses.

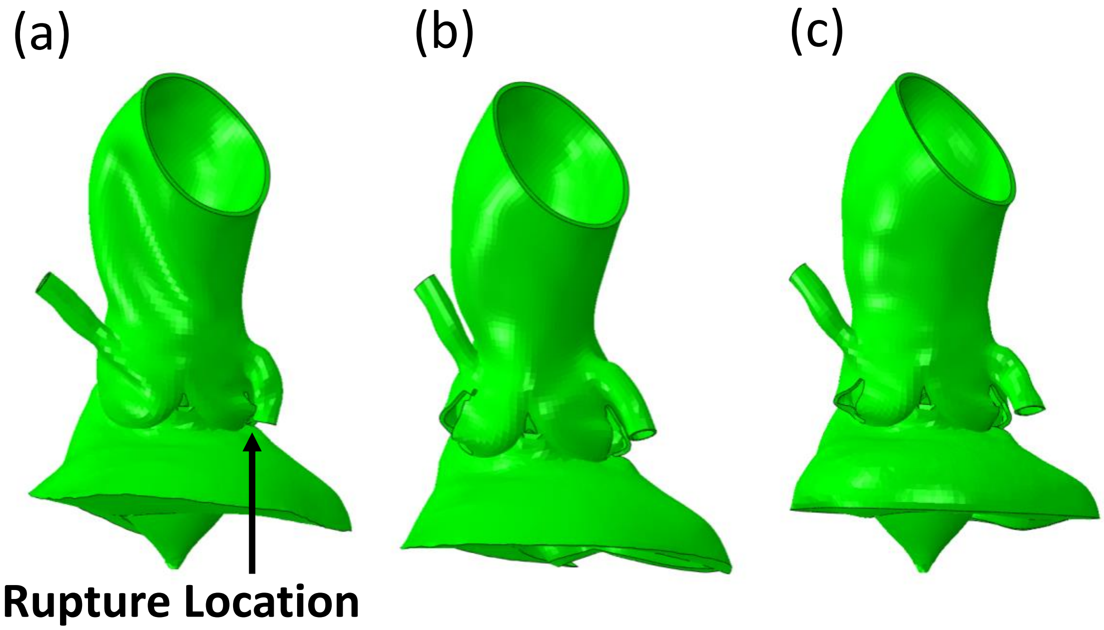

Figure 6.8 Deformed shapes of the aortic root obtained from the (a) fluid controlled, (b) displacement controlled, and (c) pressure controlled balloon expansion methods.

iii) Contact Force between the TAV Stent and Aortic Root. Contact force between the stent and aortic root, which was calculated by summing the normal contact forces of the node set that represented the outside surface of the stent, was output from the simulation. Contact forces between the TAV stent and aortic root for the fluid, displacement, and pressure controlled simulations were 109 N, 253 N, and 121 N, respectively.

iv) Computational Time. Different computational time was consumed by the three balloon expansion methods. The surface-based fluid cavity balloon expansion method was more computationally expensive than the other two methods. Computational time of TAV deployment of the patient using 32 CPU cores on a HPC cluster were 81 hrs, 25 hrs, and 28 hrs, for the fluid, displacement, and pressure controlled simulations respectively.

6.4 Discussion

The TAV implantation cases reported in the literature as well as our simulation results of the baseline case showed that the combined presence of calcification on the interior of aortic sinus and asymmetric distribution of the aortic calcification might be critical in leading to aortic rupture during TAV implantation procedures. In such calcification configuration, special care should be taken, and aggressive and full balloon dilation should be avoided.

The results of the parametric study on the TAV deployment strategies showed that an optimal combination of the balloon injection volume and stent deployment height could be found using FE simulations to minimize the potential risk of the aortic rupture and PVL. Parametric study on material parameters demonstrated that although biomechanical characteristics are generally consistent among simulations using different patient-specific material properties, the extent of the rupture was sensitive to varied material parameters. Currently, there is a lack of human aortic properties in the literature. More material testing should be done in the future to obtain the range and distribution of the aged human aortic tissue properties for different gender and age groups; and aortic rupture potential could be presented as a probability factor.

Additionally, parametric study on balloon expansion simulation methods was conducted. *i)* Surface-Based Fluid Cavity Balloon Expansion Method. During the clinical TAVI procedure, an inflation device is filled with a defined volume of fluid to achieve desired stent expansion. The entire volume in the inflation device is injected into the balloon independent of the pressure. The simulation results showed that the fluid controlled method could replicate the aortic rupture of the clinical TAVI case. Additionally, the realistic stent foreshortening and dogboning shapes were replicated by the fluid controlled simulation. The time history of the balloon pressure during expansion was extracted from the simulation and plotted in Figure 6.9, which shows the non-linear increase of the balloon pressure. However, the computational time to complete the fluid controlled simulation for the patient in the study was nearly three times of the other two methods.

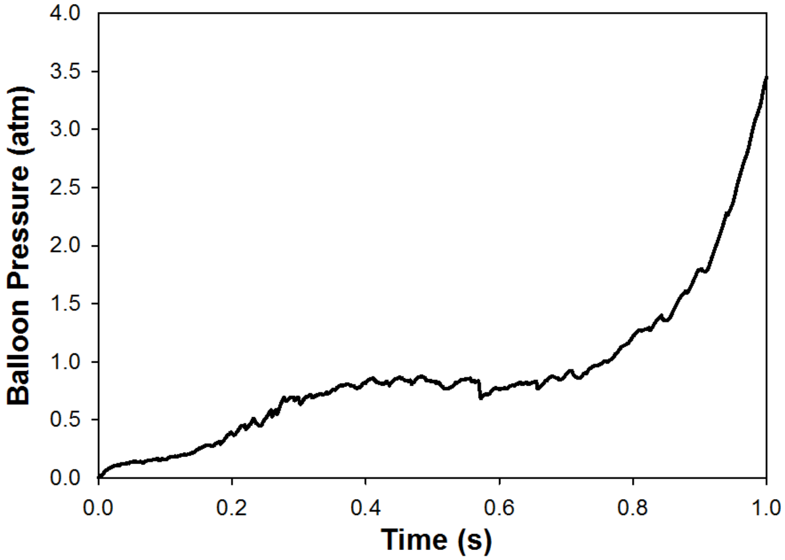

Figure 6.9 Time-dependent pressure inside the TAV balloon during expansion obtained from the surface based fluid cavity simulation.

ii) Displacement Controlled Balloon Expansion Method. Using uniform radial displacement could precisely deform the stent to a target diameter. However, the deformation of the stent was not realistic, since the deformed shaped could vary with the patient-specific calcification distribution. The simulation results showed that the stresses of the sinuses and the contact force between the TAV stent and aortic root, predicted by the displacement controlled method, were significantly higher than the other two methods. Also, the extent of the aortic rupture was more severe that the clinical observations. These results suggested that displacement controlled simulation overestimated the biomechanical interaction between the TAV stent and tissue.

iii) Pressure Controlled Balloon Expansion Method. One limitation of implementing the pressure controlled method was the selection of the applied pressure, due to the fact that patients with different annulus size, calcification volumes and distribution would require various pressure inputs that could precisely expand the stent to a desired diameter. In this chapter, for the sake of comparison, the final pressure value from the fluid controlled simulation was output and utilized as the input for the pressure controlled simulation. Although the final deformed shapes of the balloon and stent were similar, side by side comparison of the beginning stages of the expansion process revealed discrepancies between the two methods (Figure 6.10). While the balloon expansion generated by the fluid controlled simulation was gradual and continuous due to the input of the constant flow rate, a sudden volume increase was noticed between 0.4 s and 0.5 s during the balloon expansion generated by the pressure controlled simulation. This artificial kinetic energy caused by the abrupt balloon movement might contribute to the slightly higher contact force and more rupture area compared to the fluid controlled method.

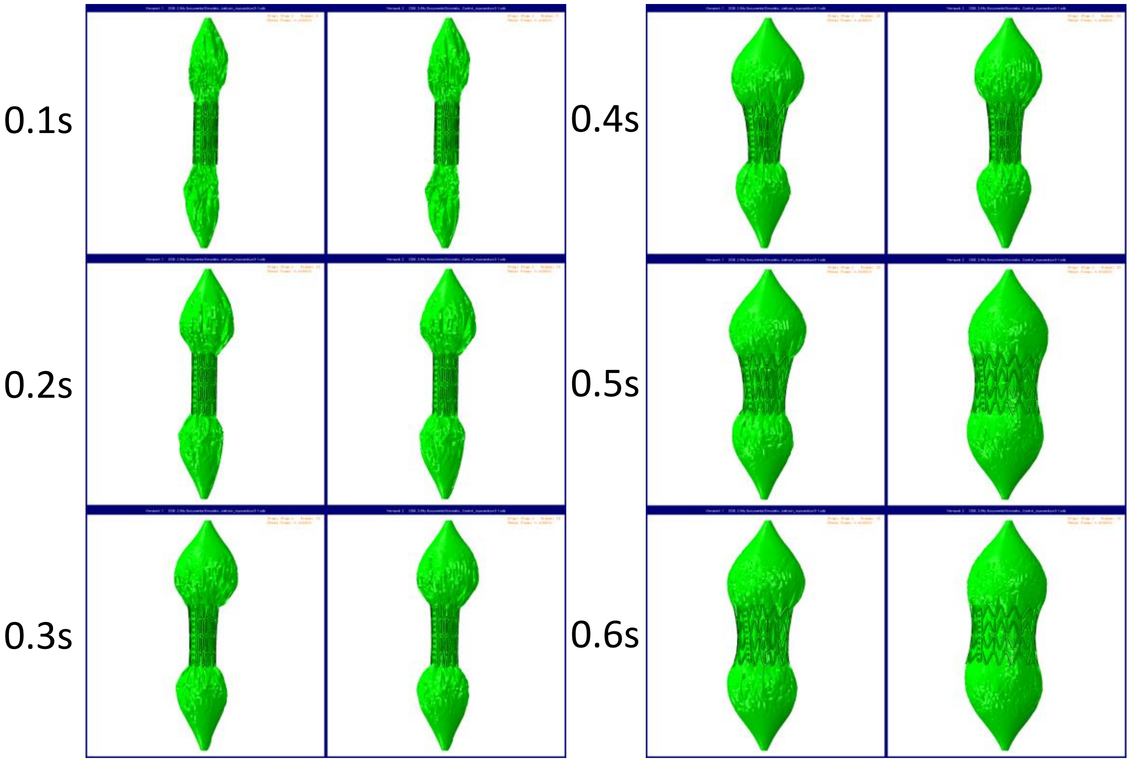

Figure 6.10 Side by side comparison of the TAV stent deployment process for the fluid controlled (left) and pressure controlled (right) balloon expansion methods.

The comparison of three different methods to simulate balloon expansion in TAVI procedure was presented. The aortic rupture site that is same as the clinical observations was reproduced by the surfaced based fluid cavity method, whereas it is the most computationally expensive. The displacement controlled method might overestimate the biomechanical interaction between the TAV stent and tissue. TAV stent and aortic root deformation that was similar to the fluid simulation could be obtained by using a linear pressure time history as input for the pressure controlled simulation. However, it is difficult to define the pressure input for the pressure controlled simulations due to patient-specific tissue compliance. The study of the three balloon expansion methods over one TAVI case demonstrated that the surfaced based fluid cavity could be the most accurate method notwithstanding the higher computational cost.

6.5 Summary

Despite the increased global experience with transcatheter aortic valve replacement (TAVR), there remain 3 major adverse events. Aortic rupture, coronary artery obstruction, and paravalvular leakage (PVL) may occur with valve implantation. Oversizing or excessive radial expansion force with the TAVR stent may cause aortic rupture, while insufficient dilatation may lead to PVL and device migration. During TAVR implantation, native leaflet material may produce occlusion of the coronary ostia. A reliable prediction of the biomechanical interaction between native tissue and device in TAVR is critical for the success of this procedure. The results of the parametric studies in this section demonstrated that FE simulations of the TAV deployment could be utilized to find the optimal deployment strategies, and thus could be utilized as a pre-procedural planning tool to virtually predict device performance for TAVR and improve clinical outcomes.

CHAPTER 7

CONCLUSIONS

7.1 Summary

Since the first procedure in 2002, there has been an explosive growth in TAVI. By the end of 2012, a total of about 90,000 TAVI had been performed worldwide. Despite the increased global experience with TAVI, severe adverse events associated with TAVI have been extensively documented, including annulus rupture, coronary occlusion, PVL, pacemaker implantation, vascular complications and stroke. Currently, there is no effective method to pre-operatively predict and prevent these adverse events.

Successful deployment and function in TAVI is heavily reliant on the biomechanical interaction between the calcified aortic root and TAV device, which requires correct TAV sizing as well as optimal positioning and expansion of the device. For instance, oversizing or excessive radial expansion force of the TAV stent may cause aortic rupture, while insufficient dilatation may lead to PVL and device migration. During TAVI implantation, the native leaflet material may cause occlusion of the coronary ostia, while positioning the TAV stent too deep into the left ventricle may cause atrio-ventricular block. A reliable prediction of the biomechanical interaction between native tissue and the device in TAVI is critical for the success of this procedure.

To assist clinicians with diagnostic and preventative strategies to prevent these clinical adverse events, I used FE method to simulate the deployment of a TAV device into an individual patient aortic root and evaluate the tissue-device biomechanical interaction. The simulation output may be used as guidelines for proper TAV sizing and positioning, appropriate and desired TAV deployment strategies inside a patient's aortic root to avoid the abovementioned adverse events.

In this chapter, we will summarize main findings of the previous chapters. Then we will propose some of the areas for the future studies and present some of preliminary works that have been done in those directions.

Chapter 2 presented a methodology to reconstruct full 3D aortic root geometric models from clinical multi-slice computed tomography scans and measure accurate dimensions of anatomical characteristics of the aortic root that is needed for pre-procedural planning of many valve procedures and development of novel valve intervention devices. Landmark points were placed on anatomic feature locations of each aortic root model for the measurement of aortic root dimensions. Diameters of the annulus, sinus of Valsalva (SOV), sino-tubular junction, and ascending aorta were compared with traditional 2D measurements.

In Chapter 3, aortic geometries reconstructed from MSCT scans were used to create computational models of TAV stent deployment and simulate the biomechanical interaction between the TAV stent and native tissue. The model incorporated aged human aortic material properties obtained from biaxial testing results.

Chapter 4 focused on the further improvement of the modeling techniques such as geometry reconstruction of detailed anatomical structures, fitting of the material parameters, and boundary conditions of the simulation. Subsequently, the developed method was utilized to analyze the mechanism of a clinical adverse event associated with TAVI.

In Chapter 5, we tried to validate our modeling approach by simulating the stent expansion process in animal models, which have been used in TAVI clinical feasibility studies. Micro-computed tomography scans of the porcine and ovine hearts were obtained to reconstruct initial geometries. The TAV stent deployment inside the animal aortic roots was simulated. The radial contact forces and stent pullout forces were compared to the experimental data in our previous study, where in-house self-expandable Nitinol stents were deployed inside porcine and ovine hearts to measure interactive forces. The comparison of tissue-device contact forces between computational and experimental data demonstrated that the finite element simulations of TAV expansion in animal models could mimic the mechanical responses of the in vitro structural experiments.

In Chapter 6, parametric studies were conducted to examine the influence of the model input such as material properties, balloon volume, stent deployment height, calcification location, and different methods to simulate balloon inflation on TAVI simulation results and subsequently the potential clinical complications such as PVL, annular rupture, and coronary artery occlusion.

Major contributions of the thesis are:

i) Developed a methodology to reconstructed 3D aortic root FE models from patient-specific multi-slice CT images

ii) Incorporated detailed anatomical structures of the human aortic roots with aortic stenosis that are necessary for the simulations of TAVI deployment process

iii) Implemented aged human aortic tissue properties with material failure criteria

iv) Simulated realistic dynamic balloon expansion process using surface-based fluid cavity method

v) Examined the biomechanical interaction between the tissue and stent for patients with a high risk of clinical adverse events.

7.2 Clinical Implications of This Research

7.2.1 Use of 3D Models for Aortic Root Measurements

In TAVI procedure, sizing is generally defined as the process where a specific prosthesis size is selected from all the available sizes to best accommodate the patient's aortic root. Optimal sizing is essential for anchoring a sutureless stent, and thus, is one the most important predictors of a successful TAVI procedure. In TAVI, the prosthesis size selected is usually slightly larger than the native annulus, which is crucial to prevent

PVL. In contrast, excessive oversizing could cause aortic annulus rupture, conduction disturbances and subsequent permanent pacemaker insertion. However, the estimated extent of oversizing strongly depends on the measurement used for annular sizing.

Depending on the imaging modality and the direction where the measurement is taken, the diameter of the aortic root could vary considerably. The aortic annulus mostly represents the narrowest part of the aortic root, and is defined as a virtual ring with 3 anatomical anchor/hinge points at the base of each aortic leaflet attachment line. In TAVI, the aortic annulus offers the first resistance and anchoring force to the sutureless prosthesis.

Traditionally, 2D echocardiograms have been used for the measurements of the aortic annulus. Due to the increased understanding of the aortic valve anatomy, a single-dimension measurement of the aortic annulus on 2D echocardiograms is not sufficient to represent the complex structure of the aortic root, and subsequently no longer accepted as the sole determinant of TAV sizing. Additionally, given the difficulty of locating the level of basal attachment or hinge points of the aortic valve cusps using 2D echo images, oblique measurements are usually taken, which could lead to over-estimation of the annular dimensions.

Over the past few years, due to the increased availability, MSCT has been integrated into clinical practice; and has become the preferred imaging modality for providing detailed and reliable description of the complex 3D aortic root geometry in patients undergoing TAVI. Clinical studies have shown that MSCT measurements of the aortic annulus have close correlation with direct surgical measurements; and are more reproducible then 2D echocardiography measurements. Despite the increased accuracy as a result of the improved spatial resolution compared to 2D echo images, aortic root measurements are still taken on a reconstructed 2D plane. Therefore, it might be difficult to identify the hinge points and align the virtual annular plane for patients with heavy aortic calcifications. Also, when a disproportionately large leaflet is present, using leaflet hinge points to reconstruct the annular plane could result in oblique measurements in relation to the central axis of the LVOT. Furthermore, as TAVI procedure was increasingly used in off-label ways, reconstructing 2D plane for the aortic annulus could be a challenge for bicuspid aortic valve patients.

In Chapter 2 of this thesis, we proposed to use full 3D aortic root geometric models from clinical MSCT scans and measure dimensions of anatomical characteristics of the aortic root. The main advantage of using 3D aortic models is that, when the cross-sectional cutting plane is reconstructed, the whole geometrical structure instead of the 2D images is visualized. Therefore, it is easier to identify the cutting plane where the aortic root measurements are taken (Figure 1.12). As a result, more accurate and reproducible measurements could be obtained for TAV sizing, especially for patients with heavy aortic calcifications or bicuspid aortic valves. Additionally, landmark points could be easily identified and placed on the 3D aortic root surfaces; and they could be used to gather important information for pre-procedural planning, such as the location and height of the coronary arteries.

7.2.2 Use of TAVI Deployment Simulations for Device Selection

Minimally invasive TAVI procedure is accepted as standard of care for patients with inoperable severe aortic stenosis; and is non-inferior to surgical replacement for high risk patients. This revolutionary therapy also has the potential to treat medium-risk patients, with the advantages of less trauma and shorter recovery time, and thus may fundamentally change the current paradigm of surgical valve replacement. Since the first procedure performed in 2002, there has been an explosive growth in TAVI. By the end of 2013, it is estimated that more than 100,000 TAVI have been performed worldwide. Despite the increased global experience with TAVI, severe clinical adverse events associated with TAVI have been extensively documented, including PVL, annulus rupture, coronary occlusion, pacemaker implantation, vascular complications and stroke.

Currently, there is no effective method to pre-operatively predict and prevent these adverse events.

Currently there are 8 TAVI devices which have received the CE mark. The balloon-expandable Edwards SAPIEN device has been used commercially in the US since November 2011. Self-expandable Medtronic CoreValve device was recently approved for commercial use in the US on Jan 17, 2014. One additional device, Edwards SAPIEN XT, received US FDA approval in the July 2014. These devices have distinct design and function features. Individualizing an optimal device for use should increase patient safety. However, this is not a trivial task and is complicated further by the existing, unresolved challenges of determining the correct sizing, positioning and expansion of the devices.

To assist clinicians with diagnostic and preventative strategies to mitigate TAVI-associated adverse events and increase patient safety, the novel simulation-based approach that was proposed in this thesis could help clinicians select an optimal TAVI device from SAPIEN, CoreValve and SAPIEN XT, by virtually simulating and predicting the in vivo performance of each device. Our TAVI simulations could be particularly useful to appropriately size borderline cases or patients with abnormal aortic geometries. The simulation output, i.e., biomechanical characteristics mentioned in Chapter 6, could provide clinicians with critical information for appropriate device selection, proper TAVI sizing and positioning, and desired TAVI expansion inside a patient’s aortic root to avoid the many TAVI adverse events.

7.2.2.1 Modeling of the Medtronic CoreValve

FE models of the stents are generated using the depictions in the literature to closely resemble the Medtronic CoreValve TAV geometry (Figure 7.1). The CoreValve system is available in 3 sizes (26, 29, and 31 mm) and can be implanted in native annuli with diameters ranging from 20 to 29 mm.

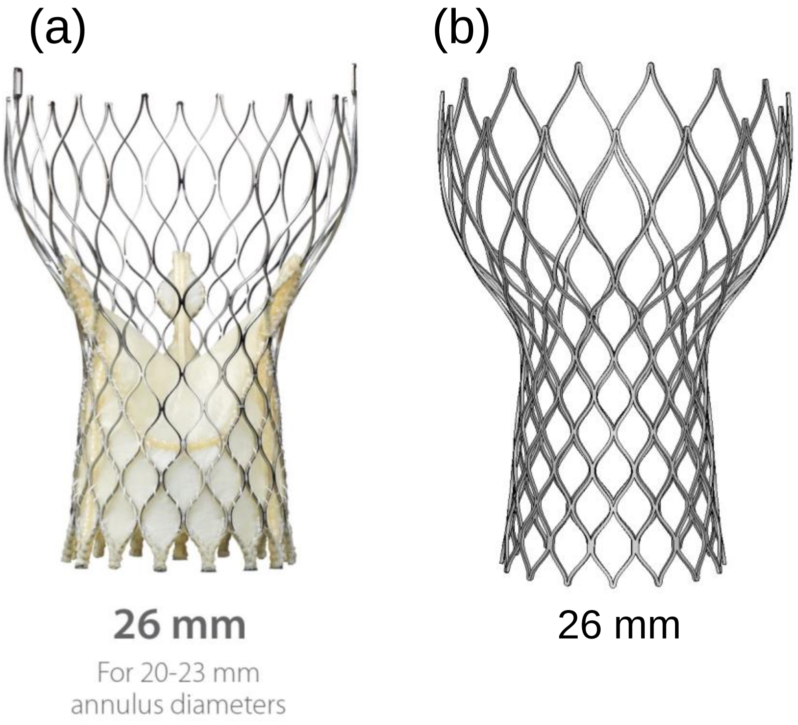

Figure 7.1 Medtronic CoreValve and finite element model of the size 26 CoreValve

The solid linear hexahedron element (C3D8I) with 4-element across the strut width and thickness and 4-element across a 90 degree arc are used to mesh the stent model to capture local peak stress/strain with high accuracy and efficiency. The stent material is Nitinol (NiTi), which is known for its superelasticity or the thermo-elastic phase transformation, the ability to transform between austenite (A) and martensite (M) phases with change in temperature. The NiTi is modeled with the phenomenological super-elastic constitutive model based on the formulation developed by Auricchio [172]. The material parameters were obtained from Tzamtizis et al. [73] with EA = 50kN/mm2; vA = 0.3; EM = 25 kN/mm2; vM = 0.3; σ_s^{AS} = 380 N/mm2; σ_f^{AS} = 400 N/mm2; σ_s^{SA} = 250 N/mm2; σ_s^{SA} = 220 N/mm2; ε_L= 7%; T0 = 37° C.

CoreValve model is crimped into a smaller size delivery catheter by radially displacing the crimper, which is modeled as a cylindrical tube. The deployment of the stent into the aorta root is initially achieved by advancing the catheter housing and the crimped stent towards a desired aortic root and at the center of leaflet coaptation lines. The catheter is aligned with the annulus and perpendicular to the basal plane (Figure 7.2 and Figure 7.3). The friction coefficient between the stent and catheter is 0.1 during release based on the studies by Mummert et al. [65] and Vad et al. [137]. The stent deployment is achieved by slowly retracting the catheter into the ascending aorta. Upon retracting the catheter, the proximal (inflow) portion of the stent that houses the valve will first flare out then the distal supra-annular region (Figure 7.4 and Figure 7.5).

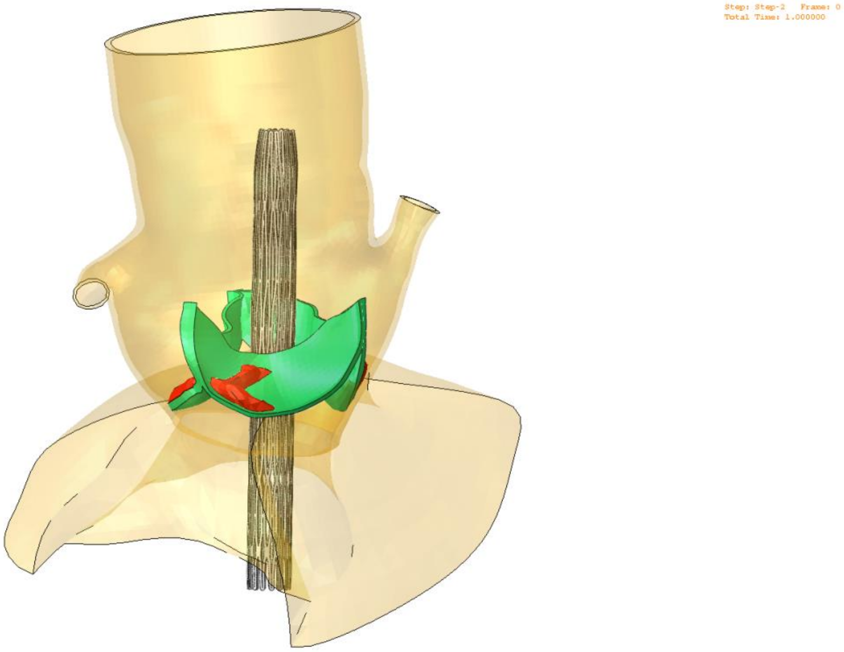

Figure 7.2 Side view of the crimped CoreValve device inside a TAVI patient before deployment

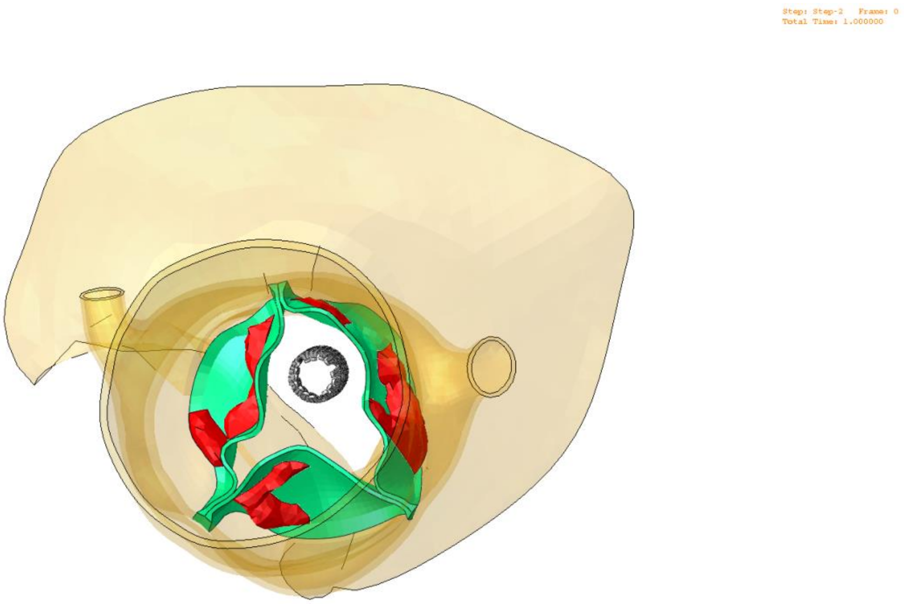

Figure 7.3 Top view of the crimped CoreValve device inside a TAVI patient before deployment

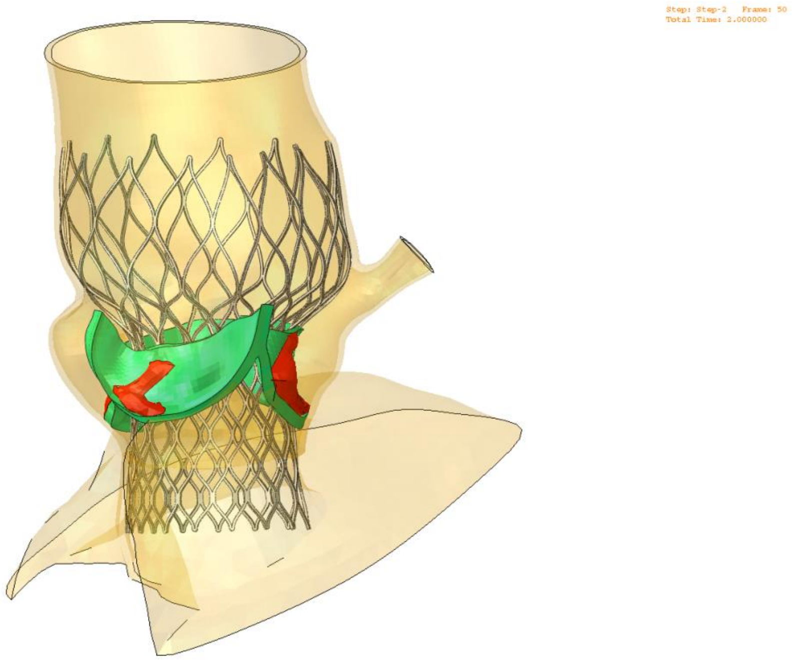

Figure 7.4 Side view of the crimped CoreValve device inside a TAVI patient after deployment

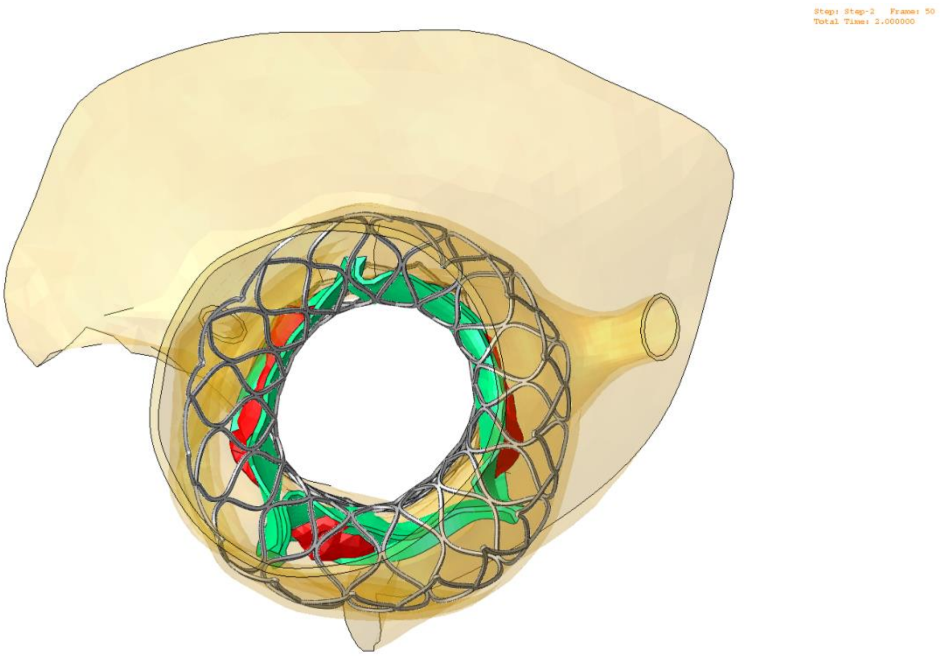

Figure 7.5 Top view of the crimped CoreValve device inside a TAVI patient after deployment

7.3 Future Directions

7.3.1 Computational-Based Preoperative Planning

Patient-specific preoperative planning using computational tools could potentially mitigate the likelihood of adverse events associated with the TAVI procedure. While the feasibility of patient-specific engineering analysis has been demonstrated through numerous studies, the main caveat preventing clinical implementation is the lack of model validation. Several groups have shown qualitative agreement between their simulation results and clinical outcomes, but in order to more rigorously validate these models more complete post-TAVI clinical data is needed, and this data is typically not collected as part of the standard-of-care.

There are also the existing issues regarding the accurate modeling of human aortic tissue properties. Currently, many groups still simplify the mechanical behavior of the aortic tissues by assuming homogenous and isotropic tissue properties. However, tissue property heterogeneity and anisotropy play important functional roles. For instance, the local increased stiffness around the aortic annulus has a sizeable effect of aortic root deformation under clinical conditions [151]. Even when the aortic tissue properties are defined by mechanical parameters fitted to human tissue testing data, these tissue properties are not patient-specific. The human tissue properties can vary greatly from patient to patient, and the impact of using different tissue properties in the existing TAVI models has not been assessed. Ideally, a patient's unique aortic tissue properties could be determined from noninvasive preoperative imaging data using inverse FE or other methods. Inverse FE methods have been successfully applied for the stress analyses of blood vessels [139, 173, 174], but not for valve tissues.

The accuracy of the TAVI computational models presented here is also limited by the lack of fluid structure interaction (FSI) analysis. FSI simulation of even native valve function is challenging. Currently, there are few heart valve FSI models, and those in the literature adopt idealized aortic geometries and tissue properties [175-180]. Therefore, FSI simulation of patient-specific TAV deployment may not be realistic at this time, but further development of these techniques could improve model accuracy in the future.

It is important to note however that there is a trade-off between model accuracy and efficiency. In order for computational-based preoperatively planning to be realistic in the clinical setting, novel methods to improve computational efficiency should be explored. TAVI computational models with varying levels of complexity should be systematically tested and validated to determine the most computationally efficient while preserving accuracy.

While it was not the focus of this thesis, we have applied the FE modeling approach to several clinical TAVI patients. Presented here were the preliminary results of the application of the pre-procedural planning of TAVI procedure. A total of 6 TAVI cases were examined. First 5 cases were retrospective studies, including 1 annular rupture case, 3 successful cases, and 1 successful valve-in-valve case. For Case 6, our FE analysis was performed before the scheduled TAVI; and simulation results were presented and discussed in the pre-procedural meeting.

Case Presentation. The 6 TAV implantation cases examined in the current study are listed in Table 1. Tricuspid aortic valve (Figure 7.6) was present in all 6 patients, where size 23 mm Edwards Sapien TAV valve was used. *Case 1:* Echocardiography revealed severe AS in the non-coronary leaflet as well as the interior of the aortic root; only left coronary leaflet could open during cardiac cycles. The pre-procedural MSCT scans (Figure 7.6) showed heavy calcification on the non-coronary leaflet, and one large calcified spot on the interior of the left coronary sinus at the level between the ostium of the left main stem and the aortic annulus entering the myocardium. During TAVI procedure, tearing happened and visualized below the left main coronary artery. *Case 2, 3, and 4:* A normal appearing percutaneously placed TAV was present in the aortic position. There was trivial or no central aortic insufficiency. The post-procedural mean transaortic valvular gradient was normal. *Case 5:* The implantation height of the first TAV was suboptimal, as the native leaflet insertion point was adjacent to the lower edge of the stent. PVL was present after the deployment of the first TAV. Subsequently, a second TAV was deployed inside the first one, in an attempt to correct the complication due to suboptimal valve positioning. Post-TAV implantation mean transaortic valvular gradient was 12 mmHg after the deployment of the second TAV. There was no aortic insufficiency. *Case 6:* Small and narrow left sinus of Valsalva was observed. Porcelain aorta was also present in the patient. Based on initial screening, the patient could be considered as a candidate to TAV implantation. FE analysis was performed before the scheduled TAV implantation; and the simulation results were presented and discussed in the pre-procedural meeting. The patient was prepared and catheterized in the hybrid operating room; and was further evaluated using echocardiography and angiography. On-site imaging assessments suggested potential high risk for the complication of coronary artery occlusion and annulus rupture, which agreed with FE simulation results. The TAV implantation procedure was cancelled.

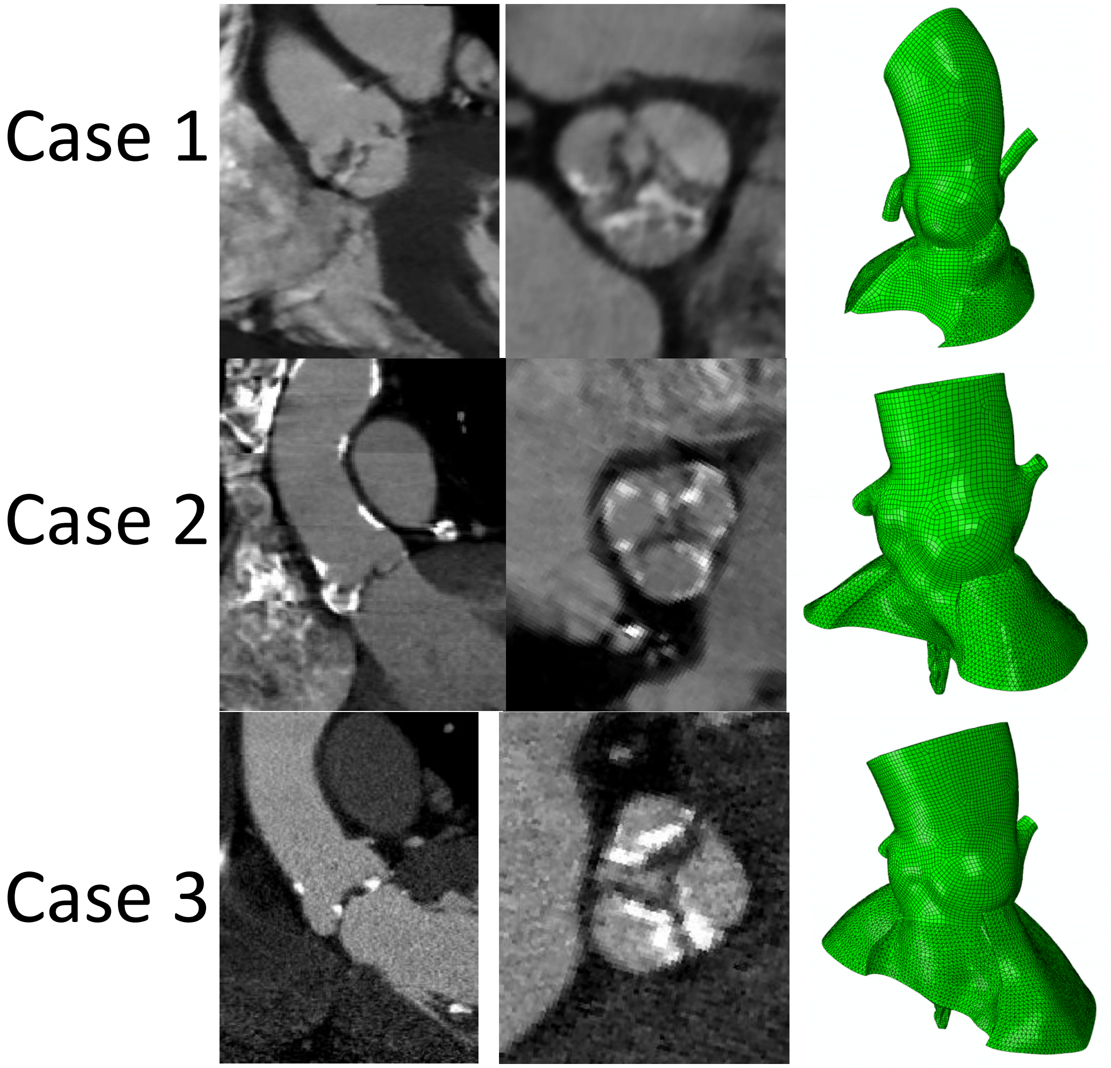

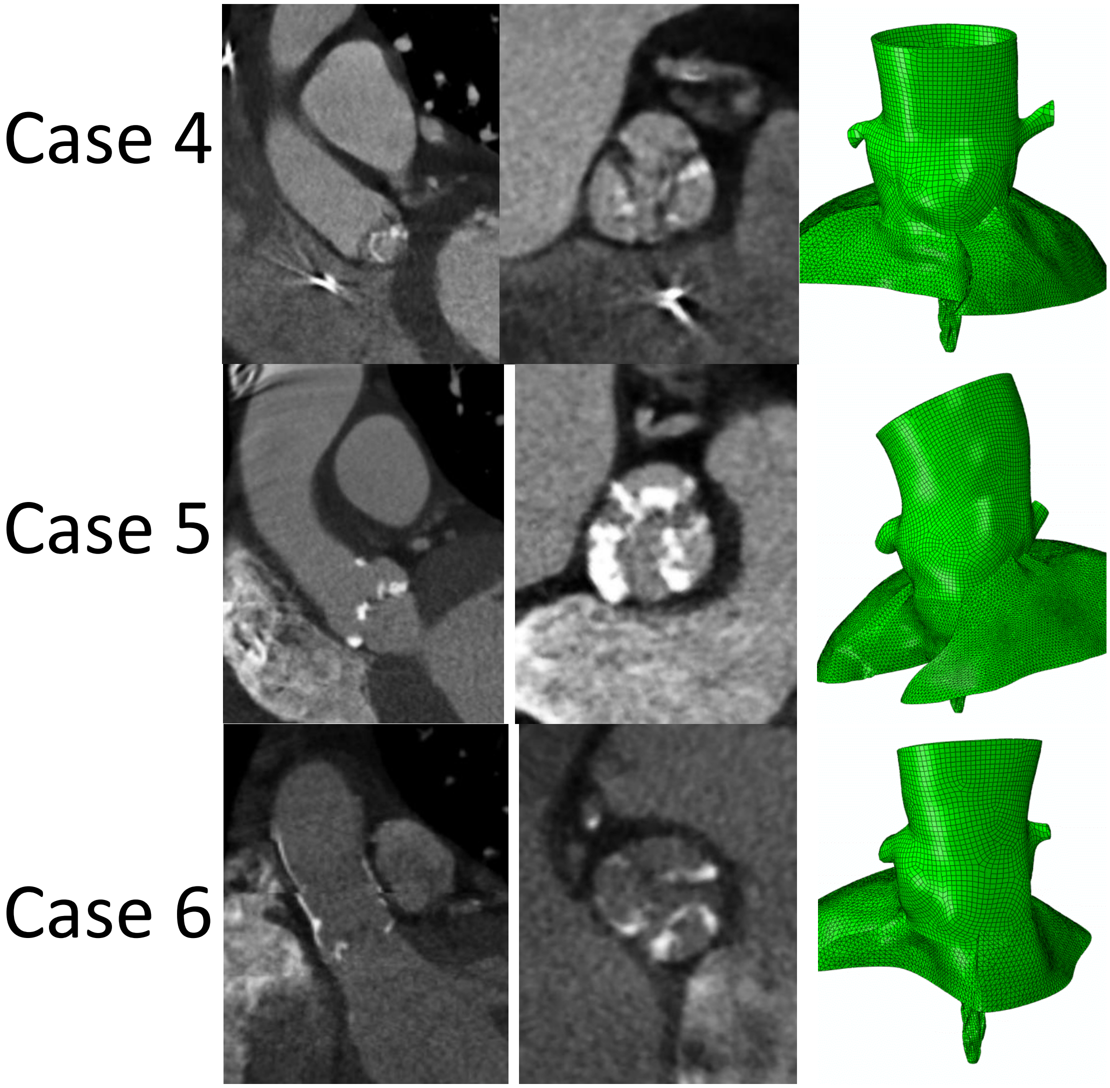

Figure 7.6 Multi-slice computed tomography images of the stenotic aortic valve in long-axis and short-axis views, and reconstructed patient-specific finite element aortic root models.

Simulation Results. Our simulation results of TAV deployment were generally in good agreement with clinical observations and the angiogram and echocardiogram of the 6 patients. The angiogram images and deformed cross-sectional geometry of aortic root FE model of Case 2 (Figure 7.7a) before, (Figure 7.7b) during, and (Figure 7.7c) after balloon expansion are shown in Figure 7.7. Side views of the deformed aortic root after the maximum stent deployment were used to evaluate the potential coronary artery occlusion (Figure 7.8); and top views of the TAV stent inside the deformed native leaflets were utilized to assess the possible PVL (Figure 7.9).

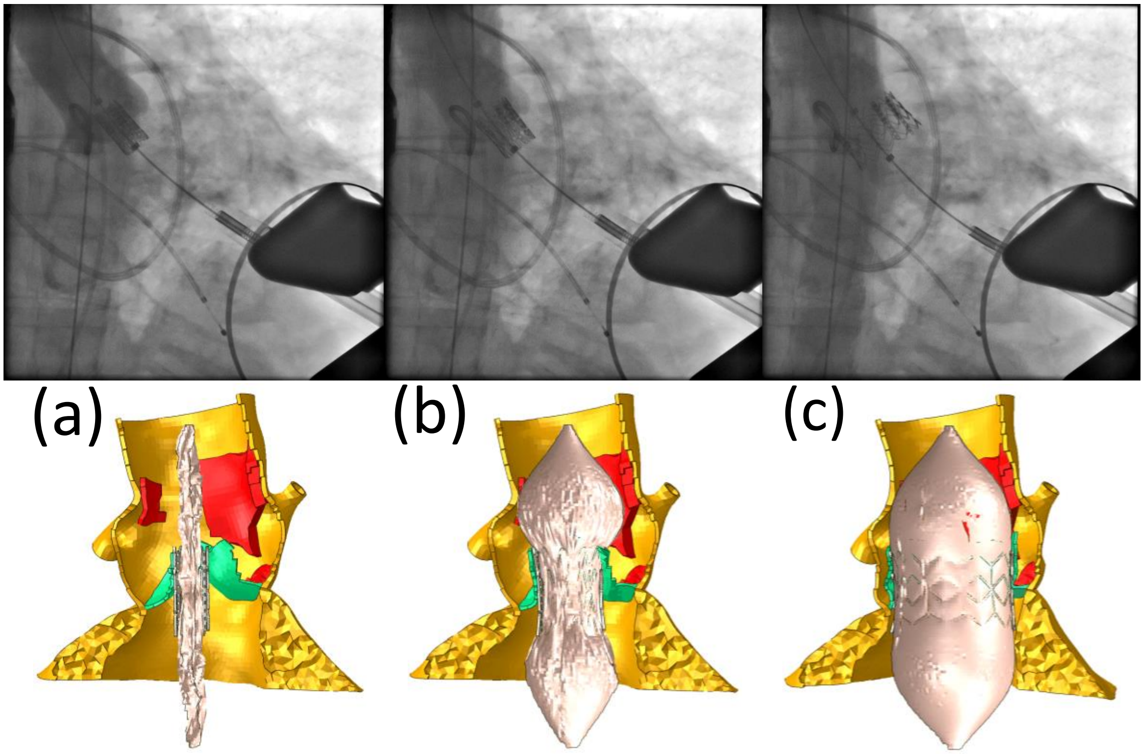

Figure 7.7 The angiogram images and deformed cross-sectional geometry of aortic root FE model of Case 2 (a) before, (b) during, and (c) after balloon expansion.

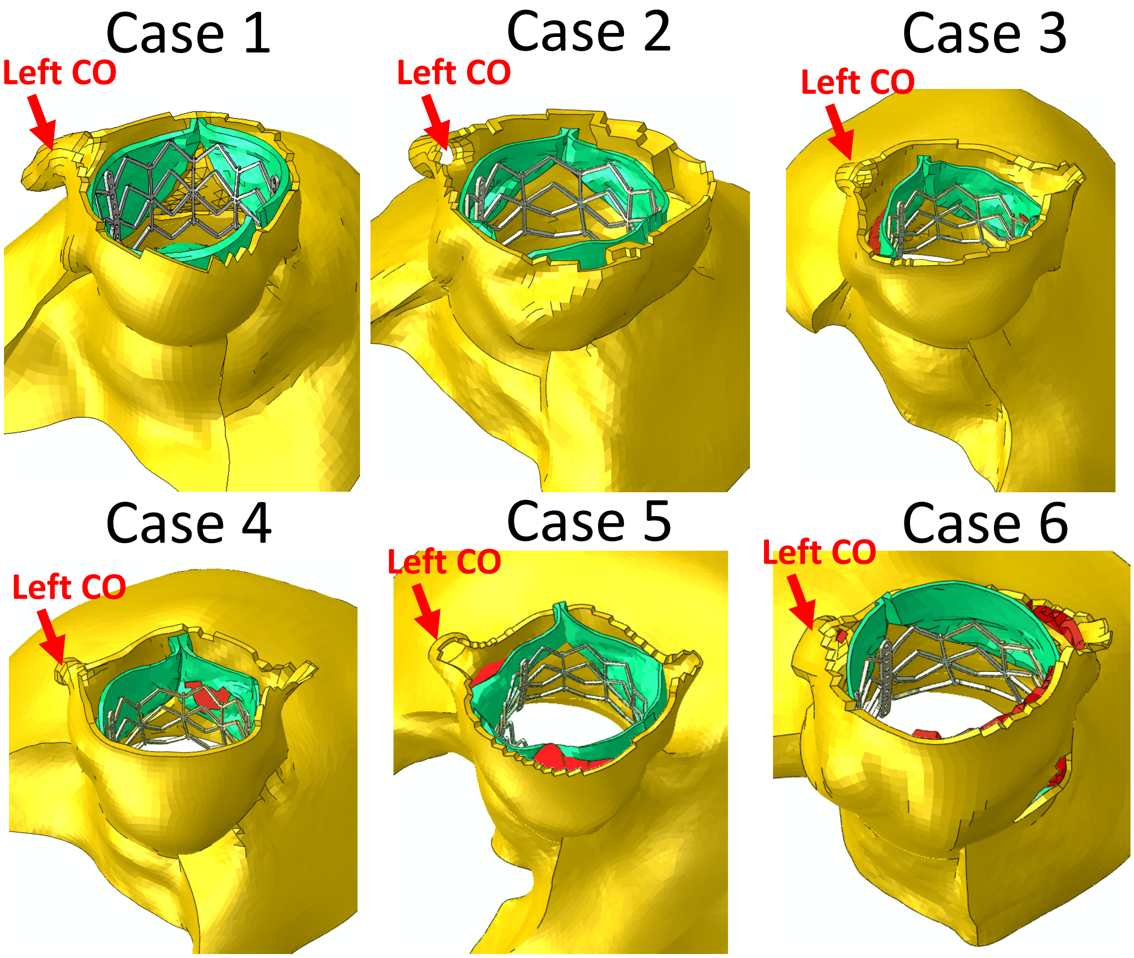

Figure 7.8 Side views of the deformed aortic root after the maximum stent deployment were used to evaluate the potential coronary artery occlusion.

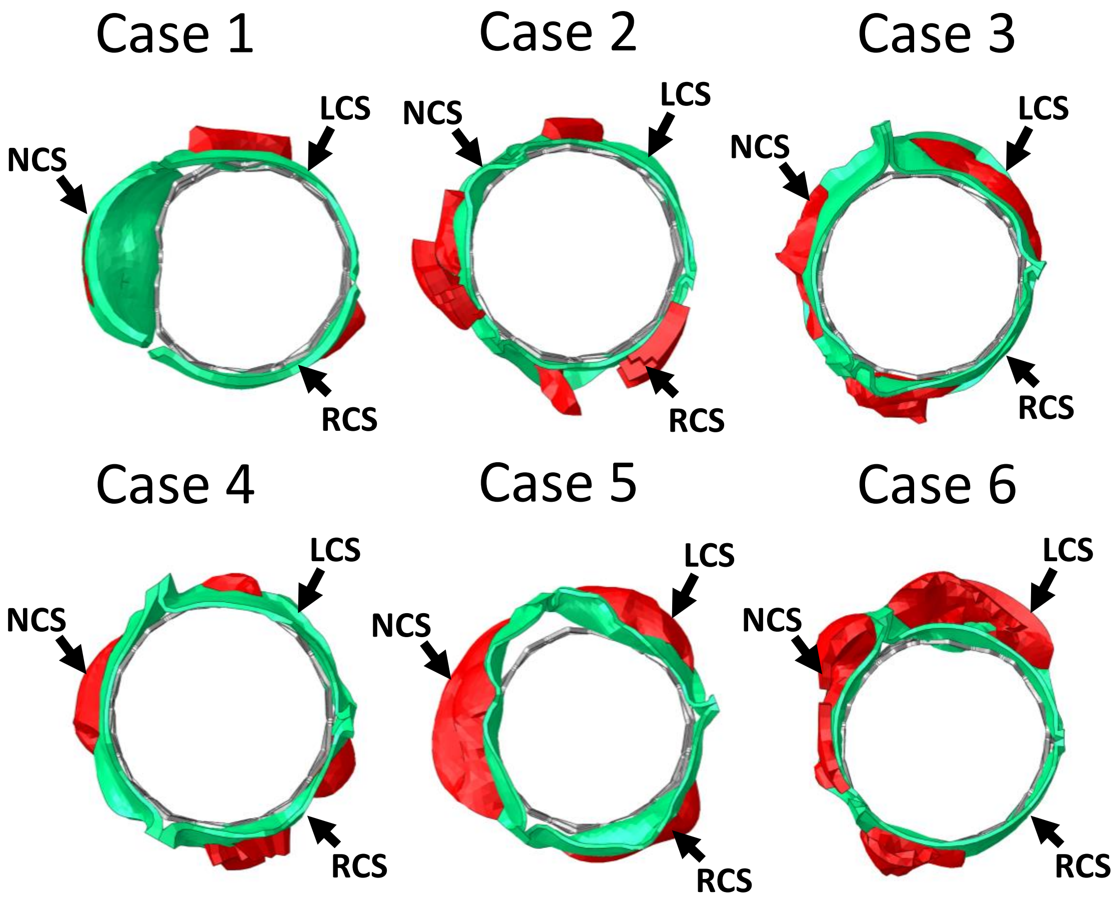

Figure 7.9 Top views of the TAV stent inside deformed native leaflets were utilized to assess the possible paravalvular leak.

Case 1 Aortic Rupture Case: The simulation of the TAV implantation procedure revealed that asymmetric distribution of the aortic calcification lead to asymmetric expansion of the TAV stent with respect to the center of the aortic root. The TAV stent in the non-coronary sinus region was partially expanded (Figure 7.9), compared to fully expanded stent in the less calcified left coronary sinus region. The calcified spot on the interior of the left coronary sinus was displaced by the TAV stent, causing stress concentration at the bottom of the left coronary sinus. Contact radial force between the TAV stent and aortic root reached 109 N, when the stent was fully deployed. Rupture of the aortic root at the bottom of the left coronary sinus occurred at roughly 82 % of the balloon volume. Rupture location in the simulation was the same as that observed in Case 1. *Case 2, 3, and 4 Successful Cases:* Our simulation results of TAV deployment were comparable to the angiogram and echocardiogram of the patients. No potential coronary artery occlusion (Figure 7.8) or PVL (Figure 7.9) was present. *Case 5 Valve-in-Valve Case:* The valve positioning of the first TAV was replicated in the FE model. PVL (Figure 7.9) was also observed in our simulation results after the deployment of the first TAV. The location of the leak was similar to the echocardiogram of the patient. *Case 6 Cancelled Case:* Our simulation suggested possibility of left coronary artery occlusion, which was in accordance with imaging assessments. Moreover, aortic rupture was present in our simulated findings.

In this section, we presented, to our knowledge, the first study using retrospective and prospective patient imaging data to develop realistic patient-specific FE models of TAV implantation procedure, which incorporated human aortic tissue material properties with material failure criteria, and balloon expansion process. Our simulation results demonstrated that the FE models of the 5 retrospective cases accurately replicated clinical outcomes of the TAV implantation procedures, especially adverse events such as PVL and aortic root rupture. Furthermore, our method was implemented in a prospective case study. Our simulation predicted the possibility of left coronary artery occlusion, which agreed with imaging assessments of the patient.

7.3.2 Computational-Based TAV Design Optimization

While computational-based preoperative planning necessitates patient-specific analyses, population-based probabilistic studies will be important for TAV design optimization. As discussed in the previous sections, the human aortic anatomy and tissue properties are highly variable and this creates uncertainty in the deployed TAV stent geometry as well as the leaflet coaptation. Probabilistic TAV computational models which account for this uncertainty will facilitate the design of next-generation TAV devices which are more robust to common deployment configurations.

7.3.3 Emerging Clinical Challenges

7.2.2.2 TAVI to Treat Aortic Insufficiency

Currently TAVI is only recommended for patients with severe AS: the commercially available, first generation, TAV devices are not suitable for patients with noncalcific aortic valve disease. The presence of leaflet calcification helps prevent device migration, and without calcification new anchoring methods must be explored. Several devices currently in clinical trials employ new anchoring methods and show promising results [181-183].

7.2.2.3 TAVI to Treat Bioprosthetic Valve Failure

TAV implantation within a failed surgical bioprosthetic valve has been shown to be feasible and safe with a reported procedural success rate of 93.1% in the largest reported TAV-in-surgical valve registry to date with 202 patients from 38 centers [184]. Considering this success rate with the morbidity and mortality associated with valve reoperation valve-in-valve (ViV) treatment for surgical valve failure will likely become an increasingly attractive option for both patients and clinicians [185]. However, the ViV configuration has been shown to distort the newly implanted TAV leaflet configuration[142], and has been hypothesized to affect transvalvular gradients, effective orifice areas, and leaflet and stent durability [121, 186-191]. The altered TAV biomechanics in this setting is not well understood, and will be an important area of research to determine optimal ViV strategies.

7.2.2.4 TAVI Long-Term Durability

Little is known about the long-term durability of TAVI devices in general, owing to the relative immaturity of TAVI and the advanced age and illness of the patients selected for this treatment. However, TAV leaflets are made of similar materials as surgical bioprosthetic valves with known durability issues, and TAV leaflets have been shown to experience higher leaflet stresses and strains [68, 70] than traditional surgical valves, particularly in the presence of aortic calcification resulting in non-circular, asymmetric stent deployment [70]. Therefore, it follows that as we gain experience with TAVI, device failure due to leaflet degeneration may become a more significant problem. Before TAV intervention can be considered a potential alternative treatment for lower-risk patients with longer life expectancies, there is a pressing need for new strategies to evaluate and improve leaflet durability.

APPENDIX A - QUANTIFICATION OF STRUCTURAL COMPLIANCE OF AGED HUMAN AND PORCINE AORTIC ROOT TISSUES

In this appendix, due to the limited knowledge of structural compliance and regional variation of aged human aortic root tissue in the literature, inflation tests were conducted to characterize the regional structural compliance of the aged human aortic root. The results generated in this appendix could be valuable to TAVI clinical feasibility studies using animal models and future prosthetic device design.

A.1 Introduction

Aortic root is defined as the portion of the left ventricular outflow tract which supports the leaflets of the aortic valve, delineated by the sinotublular ridge superiorly and bases of the valve leaflets inferiorly [36]. It comprises the sinuses, the aortic valve leaflets, the commissures, and the interleaflet triangles. The sinuses are expanded portions of the aortic root which are confined proximally by the attachments of the valve leaflets and distally by the sinotubular junction. The most common forms of aortic root diseases include aortic stenosis and aortic aneurysms. Surgical and transcatheter approaches have been used to treat these diseases with the purpose of restoring the normal function of the aortic root. Hence, the knowledge of both normal anatomy and physiological function of the human aortic root is critical to the clinical success of these operations [192]. Moreover, since aortic root diseases primarily affect patients with advanced age, there is a dire need for a complete understanding of biomechanical responses of aged human aortic tissues. However, the knowledge of structural compliance and regional variation of aged human aortic root tissue remains very limited.

The extensibility of the aortic root in the circumferential (CIRC) and longitudinal (LONG) directions was studied by several research groups [193-196] using pressure inflation tests with radiopaque markers or sonomicrometric crystals using either in vitro or in vivo animal models. The results were, however, limited to the overall dimensional changes of the whole aortic root, not specific to each of the sinuses. Studies using either planar biaxial tests [197-202] or uniaxial tests [203, 204] quantified the aortic root material properties at a specific location. Since the aortic root is heterogeneous, the overall aortic root structural compliance may not be accurately derived using such localized material testing data.

In this section, regional structural compliance of the aged human aortic root was characterized and compared, including the three sinuses: the non-coronary sinus (NCS), the left coronary sinus (LCS) and the right coronary sinus (RCS), and at three regions along the LONG direction of each sinus: the upper sinus (US), the middle sinus (MS) and the lower sinus (LS) near the aortic annulus, and the ascending aorta (AA) above the NCS. Since porcine models were used to assess the feasibility of transcatheter aortic valve (TAV) implantation under the assumption that porcine tissues are similar to aged human tissues [205], porcine aortic roots were also characterized and compared to the human ones.

A.2 Materials and Methods

A.2.1 Tissue Preparation

Ten human cadaver hearts (age of 81.00 ± 8.74 years and weight of 563.50 ± 218.35g) without any valvular heart disease were obtained from the National Disease Research Interchange (NDRI, Philadelphia, PA). The use of human tissues was approved by the Institutional Review Board at the University of Connecticut. The characteristics of human specimens were listed in Table A.1. All human hearts were fresh frozen within a post-mortem recovery interval (15.32 ± 6.51 hours) and remained frozen until delivery on the next day. All hearts were stored in −80˚C freezer prior to testing. Ten fresh frozen porcine hearts (6 – 9 months old and weight of 600.09 ± 75.46 g) were obtained from the Animal Technologies, Inc. (Tyler, TX) and stored in −80˚C freezer. Prior to testing, each heart was submerged in a 37˚C water bath until totally defrosted. Both human and porcine hearts were frozen and thaw using the same procedure. The aortic root including ascending aorta was carefully separated from the left ventricle and surrounding tissues. All adherent connective and fatty tissues on the surface of the aortic root were carefully removed from the specimens. The coronary arteries were occluded with sutures to prevent leakage during pressurization of the aortic root.

Table A.1 Patients’ clinical information

Specimen	**1**	**2**	**3**	**4**	**5**	**6**	**7**	**8**	**9**	**10**
Age	81	96	82	75	63	75	82	83	87	86
Sex	F	F	M	M	M	F	M	M	F	F
Cause of death	ALZ	CPA	COPD	CA	UNKN	CPA	CPA	VD	UNKN	UNKN
Risk factors										
Hypertension	N	N	Y	N	Y	Y	Y	Y	N	Y
Diabetes	N	UNKN	Y	N	N	N	N	N	N	N
Asthma	N	N	N	N	N	N	N	N	Y	N
Pneumonia	Y	N	N	N	N	N	N	N	N	N
Dementia	Y	N	N	N	N	N	N	Y	Y	Y
HCL	N	N	N	N	Y	Y	Y	N	N	Y
Emphysema	N	N	N	N	N	N	N	N	Y	N

Footnote: ALZ: Alzheimer’s disease, CA: cardiac arrest, CHF: congestive heart failure, COPD: chronic obstructive pulmonary disorder, CPA: chronic pulmonary aspergillosis, HCL: Hypercholesterolemia (high cholesterol levels), HTN: hypertension, RA: respiratory arrest, UNKN: unknown, VD: Vascular Dementia.

A.2.2 Experiment Setup

Each aortic root was cannulated at the AA using a plastic fitting, mounted vertically to a laboratory stand via a plastic ring clamp, and submerged in 0.9% saline solution. Fig. A.1 shows the setup of the inflation test system. The plastic fitting was connected to a pressure transducer (model BLPR2, World Precision Instruments, Sarasota, FL) and a 100 mL surgical syringe through plastic barb fittings and flexible tubing. The syringe filled with saline solution was used to pressurize the aortic root. A hand-held pressure gauge with a range up to 300 mmHg was connected to the tubing for calibration of the pressure transducer. The pressure transducer and hand-held pressure gauge were positioned at the same height level as the aortic root in order to minimize the pressure difference. The pressure transducer was calibrated up to 200 mmHg against the pressure gauge with error less than 1 mmHg. After 10 cycles of preconditioning, the aortic root was inflated from 0 to 200 mmHg by smoothly injecting saline solution to the root. An inflation pressure of 200 mmHg was chosen because the aortic root may bear high loads during procedures such as TAV implantation. Two CCD cameras (model XC-ST50, Sony Corporation of America, Park Ridge, NJ), positioned approximately 30 degree apart from each other, were utilized to capture the motion of the markers on the specimen at 30 frames per second. An in-house LabVIEW (National Instruments, Austin TX) program was developed to simultaneously acquire videos from the two cameras and pressure data from the pressure transducer.

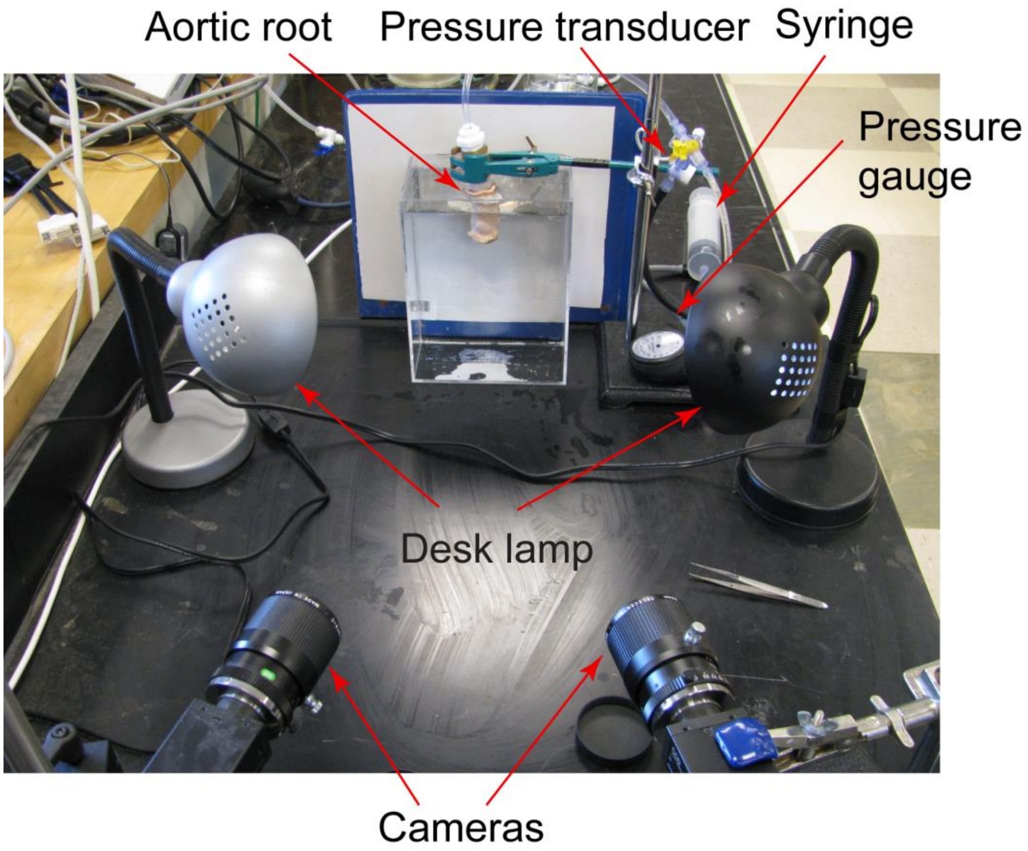

Figure A.1 Schematic of the primary components in the inflation test system, including a specimen chamber, an inflation test system consisting of a pressure transducer, pressure gauge, syringe and two digital cameras.

A.2.3 Surface Strain Computation

The marker layout on the aortic root is shown in Fig. A.2a. The markers were used to calculate the mechanical responses of each sinus and at three regions along the LONG direction— US, MS and LS, as well as AA. To minimize the effect of coronary arteries on the strain measurement of RCS and LCS, the markers were affixed away from coronary arterial ostia. The marker pattern on the specimen was arranged so that each region consists of 7 markers (Fig. A.2b). Three dimensional (3D) spatial coordinates of the markers were reconstructed from the 2D images using the direct linear transformation method [206-208]. The 3D coordinates of all markers were captured at all frames to calculate the displacement gradients and the regional in-plane Green strain.

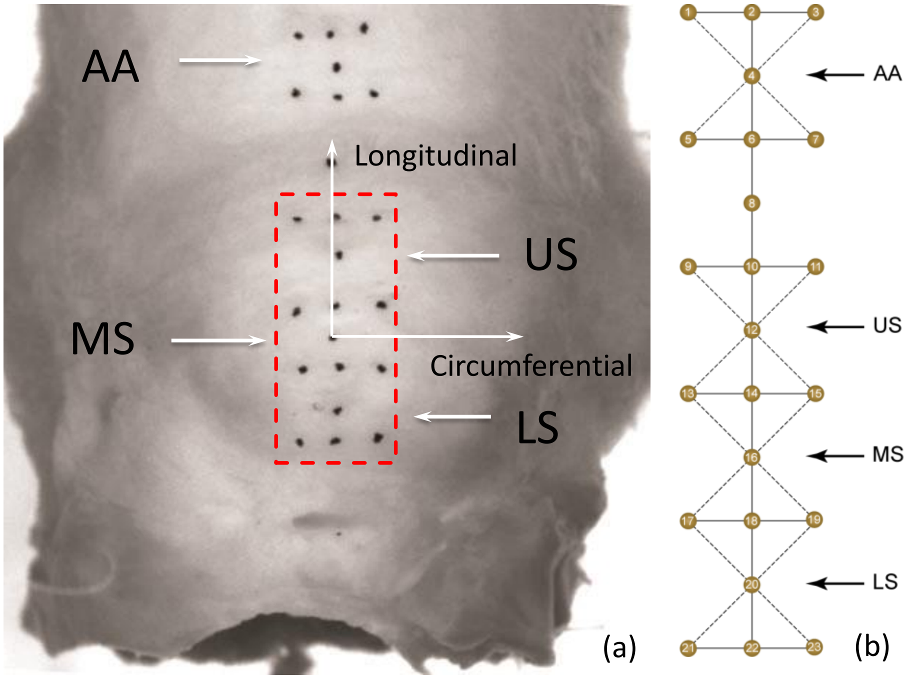

Figure A.2 a) The marker layout on the surface of non-coronary sinus (NCS) demarcating the Upper Sinus (US), Middle Sinus (MS) and Lower Sinus (LS) regions and the ascending aorta (AA). Note the AA was tested on the region superior to NCS only; b) the numbering of the markers on each sinus region.

To compute the in-plane Green strain within each region, shell-based 2D isoparametric finite element shape functions [209] were used to fit the surface geometry of each region. Following the surface fitting methods reported by Sacks et al. 2002 [210], the local surface of aortic sinus, in the region delimited by the 7 markers, was approximated by a seven-node C0-continuity quadratic Lagrangian element. The surface fitting of the initial state (Pressure = 0 mmHg) yields the reference configuration of the region. To determine the strain field at each frame, the displacements of each marker were computed as the difference between the reference and the deformed spatial marker positions. The displacement component was fitted separately using the same shape functions. This fitting was completed for each region at each frame. The in-plane components of Green strain (E_{ij}) were determined by the fitted continuous displacement functions (ui), as follows:

$$E_{ij} = \frac{1}{2}\left[\frac{\partial u_j}{\partial x_i} + \frac{\partial u_i}{\partial x_j} + \frac{\partial u_\alpha}{\partial x_i}\frac{\partial u_\alpha}{\partial x_j}\right], \tag{A.1}$$

where xi and xj indicate differentiation with respect to the in-surface coordinate components, α is the repeating index. The respected stretches λ11 and λ22 in the CIRC and LONG directions were calculated for each region by

$$\begin{aligned} \lambda_{11} &= \sqrt{\mathbf{u} \cdot \mathbf{Cu}}; \\ \lambda_{22} &= \sqrt{\mathbf{v} \cdot \mathbf{Cv}}, \end{aligned} \tag{A.2}$$

where u and v are unit vectors along the CIRC and LONG directions, respectively, $\boldsymbol{C} = 2\boldsymbol{E} + \boldsymbol{I}$ denotes the right Cauchy-Green tensor, where I is the identity tensor.

A.2.4 Data analysis

To estimate the structural stiffness of aortic root tissues, the pressure–strain elastic modulus Ep is calculated [211] by

$$E_p = \frac{P_{sys} - P_{dia}}{(\lambda_{sys} - \lambda_{dia})/\lambda_{dia}}, \tag{A.3}$$

where sys and dia denote the systolic and diastolic phases, respectively. We chose Pdia = 10.67 kPa (80 mmHg) and Psys = 16.00 kPa (120 mmHg). λ_{sys} and λ_{dia} are corresponding stretches in either CIRC or LONG direction. The pressure-strain elastic modulus was used to compare the structure stiffness between different regions.

To further analyze the aortic compliance, the extensibility of the samples was calculated and compared via the areal strain as follows

$$e = \lambda_{11p}\,\lambda_{22p} - 1, \tag{A.4}$$

where λ11p and λ22p are the CIRC and LONG stretch values, respectively, at three pressure levels of p =10, 15, and 25 kPa. A pressure of 25 kPa was chosen to represent a hypertensive condition. Patients' characterization including age, gender, hypertension (HTN) or normotensive (NTN) were related to the biomechanical parameters to determine any correlation.

A.2.5 Statistical Analysis

Statistical analyses were evaluated using SigmaPlot (V11.0, Systat Software Inc., San Jose, CA). Both one-way and two-way Repeated Measures ANOVA tests were used to compare the difference among the three sinuses and the regions along the LONG direction. The Tukey pairwise multiple comparison procedures were performed to identify which group is different, with $p < 0.05$ was considered a statistically significant difference and $p < 0.001$ indicates highly statistical significance. The Student's t-test was used to determine significant differences between the parameters between human and porcine tissues.

A.3 Results

A.3.1 Pressure-Green strain responses

The mean pressure-Green strain responses of human and porcine sinus tissues were shown in Figs. A.3 and A.4. The human tissues were distinctively stiffer than porcine tissues. Specifically, the human tissue stiffened rapidly at a low pressure range of 5 – 10 kPa, whereas porcine tissue responses behaved linearly up to 15 – 20 kPa. At the pressure of 27 kPa, the peak strains were similar in both LONG and CIRC directions for the human aorta, while for the porcine aorta the CIRC strains were higher than the LONG strains (Table A.2). Similar to the sinuses, the structural responses of human AA tissues were much stiffer than those of porcine tissues, as shown in Fig. A.5.

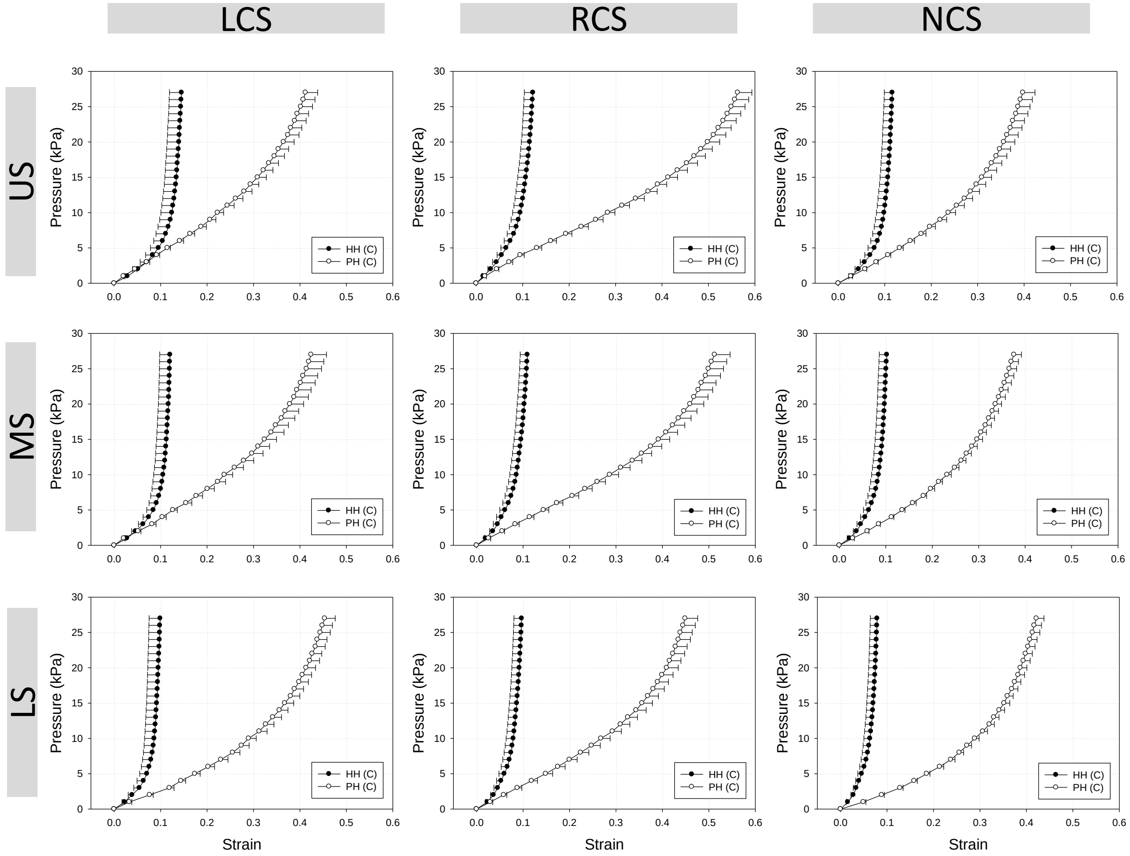

Figure A.3 The pressure-Green strain curves (mean and standard error) in the circumferential (CIRC) direction of human (HH) and porcine (PH) aortic root tissues. LCS – Left Coronary Sinus, RCS – Right Coronary Sinus, NCS – Non-coronary sinus, US – Upper Sinus, MS – Middle Sinus, and LS – Lower Sinus.

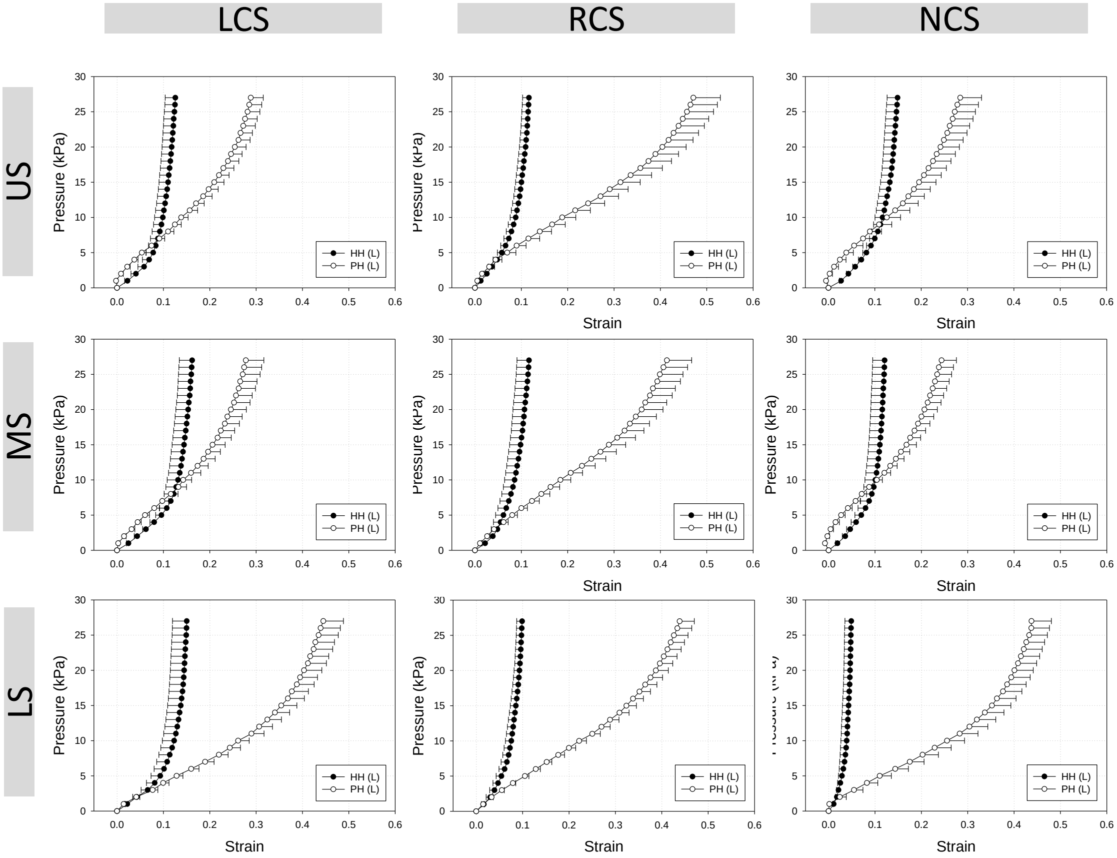

Figure A.4 The pressure-Green strain curves (mean and standard error) in the longitudinal (C) direction of human (HH) and porcine (PH) aortic root tissues.

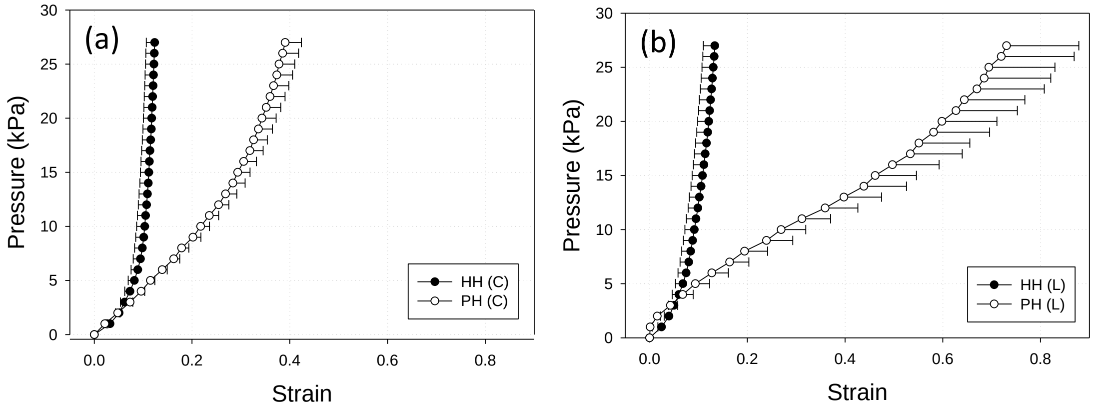

Figure A.5 The pressure-Green strain curves (mean and standard error) in the circumferential (C) and longitudinal (L) directions of human (HH) and porcine (PH) ascending aortic tissues.

Table A.2 Maximum strains at a maximum stress of 27 kPa for both human and porcine aortas.

		Human		**Porcine**	
		CIRC	***LONG***	***CIRC***	***LONG***
LCS					
	US	0.15± 0.08	0.13± 0.07	0.41± 0.08	0.29± 0.09
	MS	0.12± 0.07	0.16± 0.09	0.42± 0.10	0.28± 0.12
	LS	0.10± 0.08	0.15± 0.10	0.45± 0.07	0.45± 0.13
RCS					
	US	0.12± 0.06	0.12± 0.04	0.56± 0.09	0.47± 0.18
	MS	0.11± 0.05	0.12± 0.08	0.51± 0.11	0.41± 0.17
	LS	0.10± 0.05	0.10± 0.04	0.45± 0.09	0.44± 0.10
NCS					
	US	0.12± 0.06	0.15± 0.07	0.40± 0.08	0.28± 0.14
	MS	0.10± 0.05	0.12± 0.08	0.38± 0.05	0.24± 0.10
	LS	0.08± 0.05	0.05± 0.04	0.42± 0.05	0.44± 0.13
AA		0.12± 0.05	0.13± 0.08	0.39± 0.09	0.73± 0.42

There are no significant differences in the pressure-strain modulus among the three human sinuses, see Fig. A.6a (i.e., the averaged responses of LS, MS and US of each sinus). However, various regional differences were observed, see Fig. A.6c-d. In the CIRC direction, the LS regions were the stiffest in the LCS (p = 0.023) and RCS (p =

0.048) sinuses, while NCS had relatively uniform stiffness. In the LONG direction, there were no significant difference of stiffness among the three LS, MS and US regions. However, the AA regions were significantly more compliant than the LS regions of LCS ($p = 0.035$), RCS ($p = 0.028$), NCS ($p = 0.016$) and the MS regions of RCS ($p = 0.008$) and NCS ($p = 0.004$).

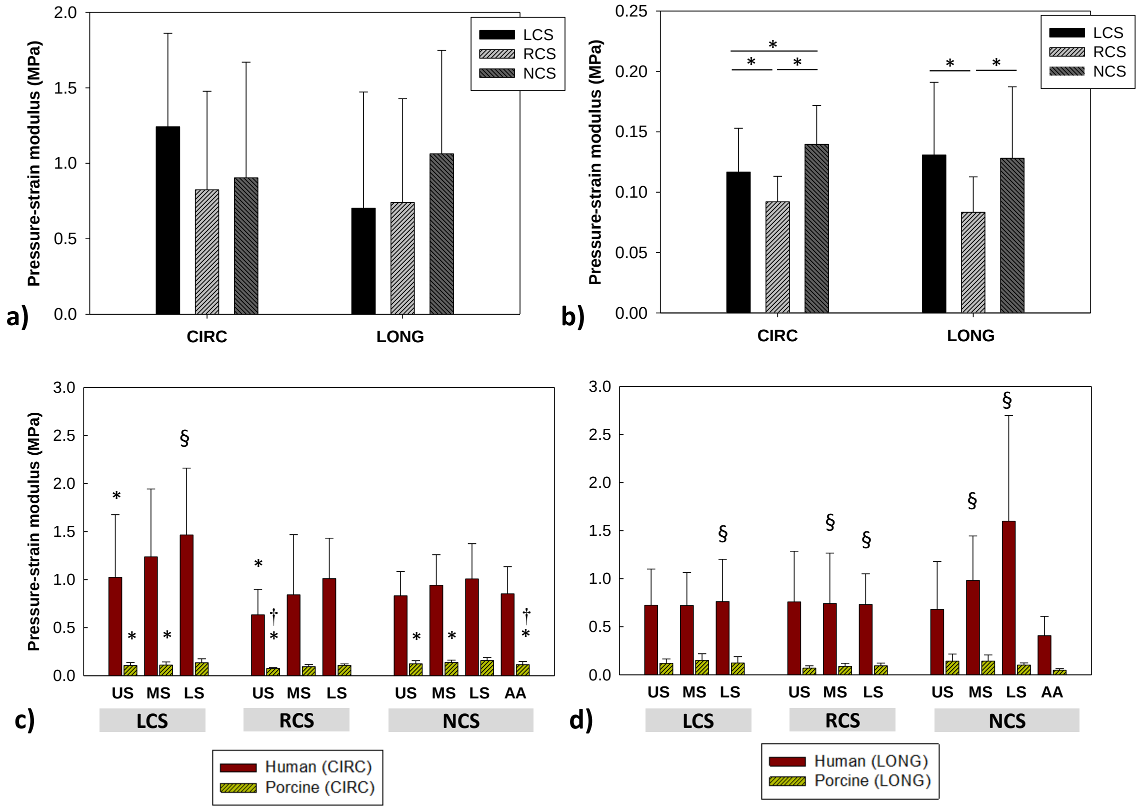

Figure A.6 Variation of the pressure-strain modulus in the circumferential (CIRC) and longitudinal (LONG) directions among the three sinuses of (a) human and (b) porcine tissues and among the regions of the sinuses in the (c) CIRC and (d) LONG of the human and porcine aortic tissues. * $p < 0.05$ compared to LS; † $p < 0.05$ compared to MS; § $p < 0.05$ compared to AA. All human aortic tissues were significantly stiffer than the corresponding porcine tissues.

Significant differences between porcine sinuses were observed: NCS was stiffer than RCS ($p < 0.001$) in both CIRC and LONG directions and LCS ($p = 0.042$) in the CIRC direction. LCS was stiffer than RCS in the CIRC ($p = 0.027$) and LONG ($p < 0.001$) directions, as shown in Fig. A.6b. For the regional variation, in the CIRC direction, LS was stiffer than US ($p = 0.001$) and MS ($p = 0.006$) of LCS, US ($p < 0.001$) of RCS, US ($p < 0.001$), MS ($p = 0.018$) of NCS and AA ($p < 0.001$). The MS regions were stiffer than US of RCS ($p = 0.033$) and AA ($p = 0.016$). No regional differences were observed in LONG direction of porcine specimens.

A.3.2 Areal strain comparison

No regional differences in areal strain were observed between sinuses and regions in human LCS and RCS specimens (Fig. A.7). For human NCS, the US and MS regions were significantly more extensible than LS regions (US vs. LS: $p < 0.001$ at all pressure levels; MS vs. LS: $p <0.05$ at all pressure level). For porcine specimens, on the other hand, the LS regions were more extensible than other regions, particularly compared to US and MS regions in LCS (LS vs. US: $p < 0.05$; LS vs. MS: $p <0.05$) and NCS (LS vs. US: $p < 0.05$; LS vs. MS: $p <0.05$). For the RCS specimens, however, LS regions were similar to other regions at all pressure levels. The porcine AA specimens were more extensible than all sinus regions, $p < 0.05$. Note that for human specimens, no differences in areal strain were observed between the sinuses and AA specimens or between the pressure levels. A significant difference was observed in all pairwise comparison of areal strain between human and porcine aortic tissues.

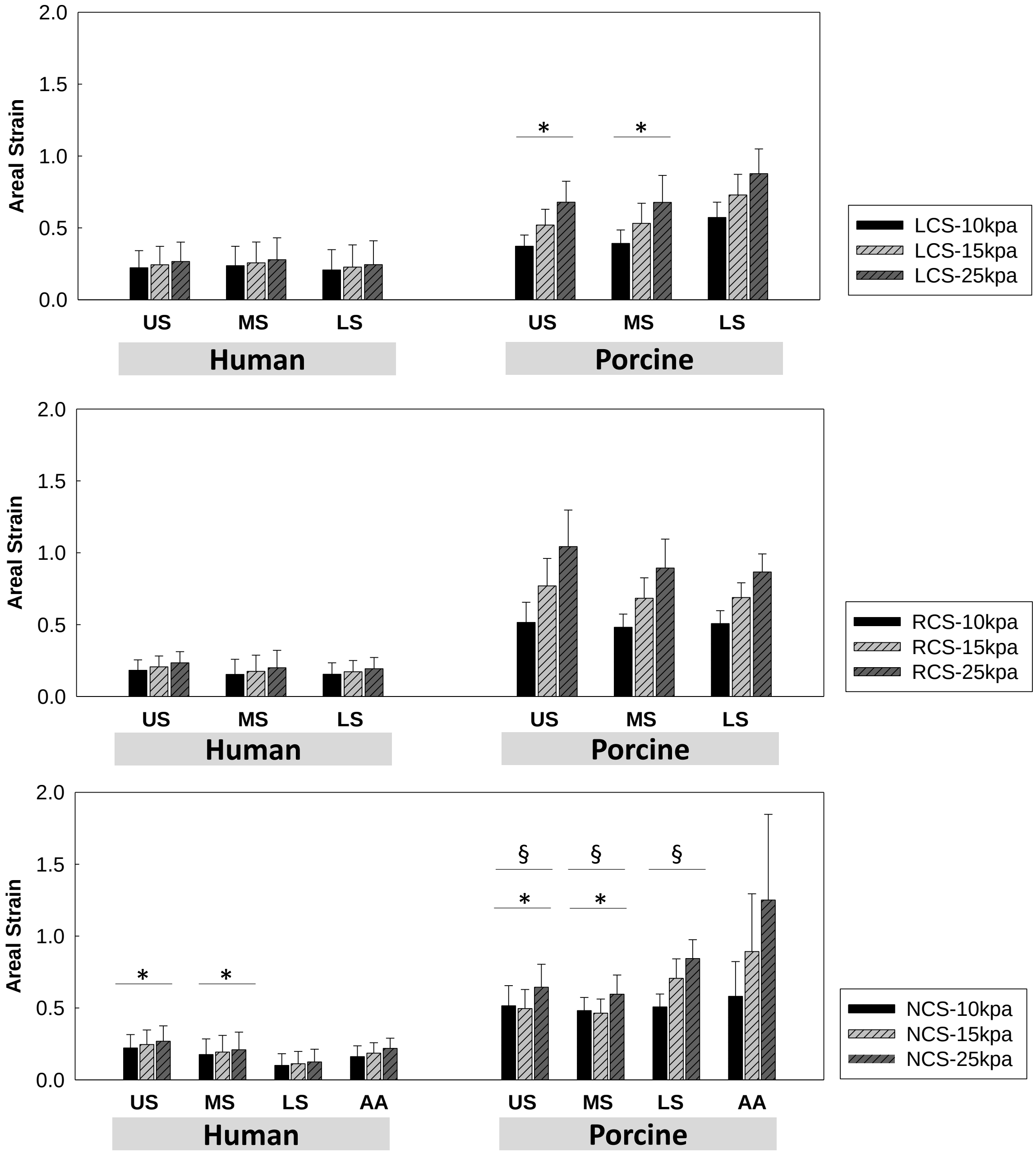

Figure A.7 Variation in (a) circumferential (CIRC) and (b) longitudinal (LONG) pressure-strain modulus of the human and porcine aortic tissues. * $p < 0.05$ compared to LS; § $p < 0.05$ compared to AA. Difference between stress levels within sinus and regions are all significant for porcine, but not human tissues. All human aortic tissues were significantly stiffer than the corresponding porcine tissues.

A.3.3 Correlation between age and compliance

A correlation trend was observed between age and human aortic compliance. Fig. A.8 shows the aortic tissue areal strain significantly decreased as age increases in LCS and NCS. While all regions in NCS specimens negatively correlated strongly with age, only the MS and LS of LCS decreased as age increases. The pressure-strain moduli correlated very weakly with age and were only significant for the LS (p = 0.045 for CIRC direction) and MS (p = 0.041 for LONG direction) of LCS specimens.

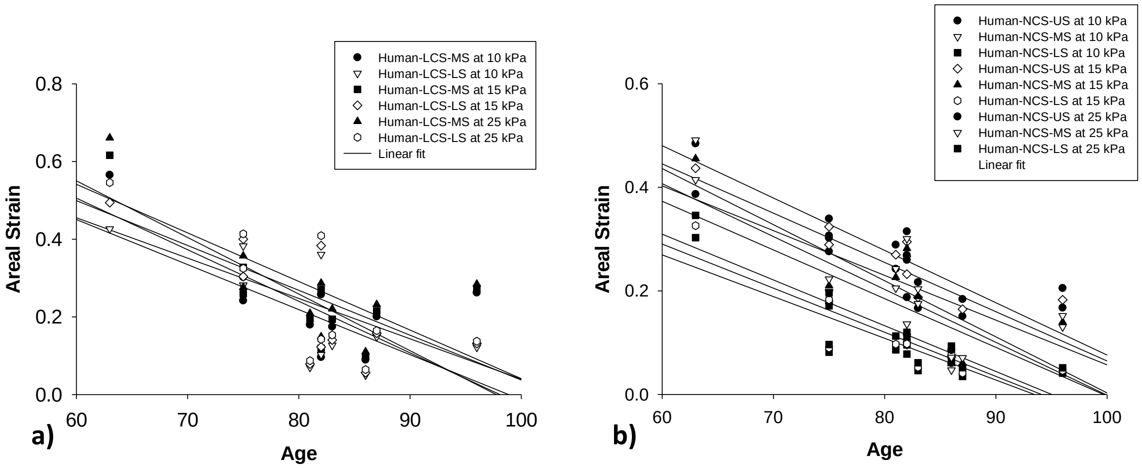

	LCS-MS		LCS-LS		NCS-US		NCS-MS		NCS-LS	
	R	***p***	***R***	***p***	***R***	***p***	***R***	***p***	***R***	***p***
At 10 kPa	-0.698,	0.025	-0.751	0.012	-0.825	0.003	-0.767	0.010	-0.871	0.001
At 15 kPa	-0.720	0.019	-0.770	0.009	-0.827	0.003	-0.770	0.009	-0.870	0.001
At 25 kPa	-0.698	0.025	-0.751	0.012	-0.825	0.003	-0.767	0.010	-0.871	0.001

Figure A.8 Correlations between age and areal strain for (a) LCS and (b) NCS specimens. Table shows the correlation coefficient, R, and p-values. Solid lines are the linear fits to the datasets.

A.4 Discussion

In this appendix, the structural properties of the aged human and porcine aortic tissues were investigated using a 3D marker tracking technique. This tracking technique allowed quantification and comparison of the structural properties of three regions along the LONG direction of the three sinuses, and AA. We found that tissue stiffness at the physiological pressure range was similar among the human three sinuses. The AA region were found to be more compliant than the sinuses, which is consistent with other studies. Martin et al. [201] found that AA tissues were more compliant than LCS and RCS tissues in the LONG direction. Azadani et al. [197] found that fresh human AA tissues were significantly more compliant than the sinus tissues in both the CIRC and LONG directions. Similarly, Gundiah et al. [202] also determined that their porcine sinus tissues were stiffer than AA tissues in both directions.

The regional structural stiffness of human aorta was observed. The CIRC LS regions were the stiffest in the LCS and RCS sinuses, while NCS had relatively uniform stiffness. The observation that human LS was stiffer than MS and US may be explained by the fact that calcification of human aortic roots is mainly localized at the region adjacent to the aortic annulus. The samples were selected from an advanced aged patient group. Light calcium deposition was observed in the lumen layer of the root, at the annular-sinus regions, commissure regions and sinotubular junction in most of patient samples as shown in Fig. 9, which could contribute to the high stiffness of the LS region. However, it did not affect the valve function, i.e. the valves were closed properly during testing. Another factor that might have caused a high stiffness in structural tissue properties is hypertension. Hypertension is a significant risk factor for many diseases and is well known to induce changes in the mechanical properties of the cardiovascular [212] and other arteries [213]. A total of six out of ten patients had a record of systematic hypertension. We observed that these three out of six patients exhibited a higher physiological stiffness than the group mean in the LS region. Our observation suggests a trend towards an increase in physiological stiffness with either or both calcification and hypertension. In addition, a negative correlation between age and human tissue compliance was observed. The microstructural components such as elastin and collagen play an important role in tissue compliance. Studies have shown that the decrease in elastin functionality [214] and the increase in collagen fiber recruitments with aging [215, 216] might greatly impact the mechanical properties of aortic tissues, resulting in higher stiffness and lower areal strain. A future study on the changes of the microstructure in aging aorta in relation to changes in the structural properties as a result of the hemodynamic alternation is needed to elucidate an increase in stiffness of aged human aortic tissues.

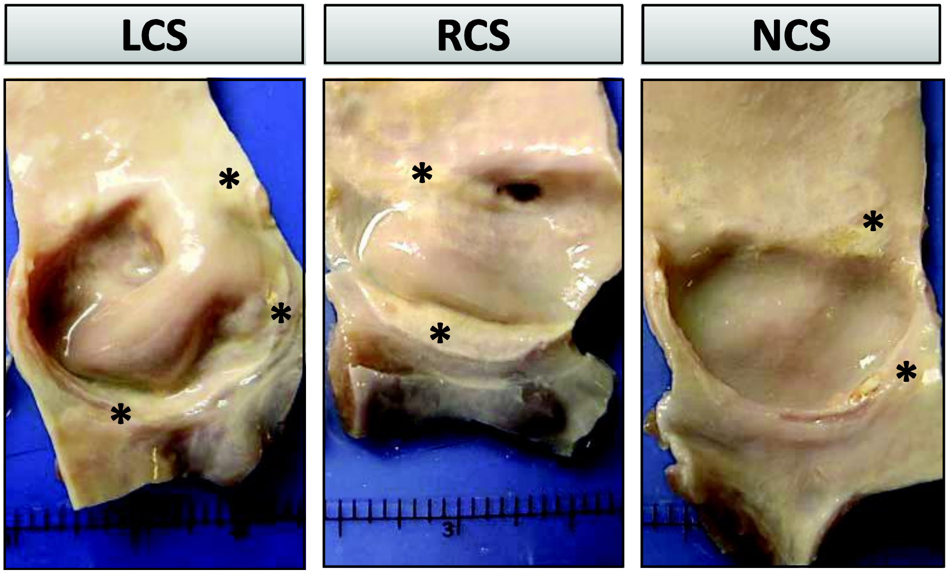

Figure A.9 Representative images of the Left-Coronary Sinus (LCS), Right-Coronary Sinus (RCS) and Non-Coronary Sinus (NCS) of a human aortic root (Specimen 5). Asterisks indicate locations of calcium deposition in the lumen layer of the aortic wall. [1mm sub-division for all images]

Statistical significant differences in stiffness and areal strain between human and porcine aortic root tissues were found in this section, which is similar to a previous study [201] comparing the planar biaxial mechanical properties of human and porcine aortic tissues. One reason is that human specimens used in this section were obtained from older patients with mean age of 81 ± 8.74 years, which could result in an overall higher stiffness of human aortic tissues. As shown in Fig. A.7, for human samples, there was no significant increase in the areal strain when pressure increased from 10 to 25 kPa.

However, for porcine specimens, there was a significant increase in the areal strain as pressure increases. These differences indicate that porcine aortic tissues might not be analogous to human. As this phenomenon has been previously reported in aortic tissues [201] and other cardiovascular tissue studies [159], it is important to know the discrepancy between the animal and human models to avoid erroneous assumption when one attempts to apply animal data to human study, particularly in the pre-clinical animal study of prosthetic devices. Computational modeling has also been employed as a predictive tool to study the biomechanics of the aortic root and to better understand the complex interactions between prostheses and host tissues. To date, due to the lack of experimental data, many computational studies assumed homogeneity [97] of aortic root and of different locations on the root. The aortic root has been characterized as either linear elastic (isotropic or anisotropic) [217-221] and nonlinear hyperelastic [222-225]. The current experimental data provide a detailed quantification of regional aortic responses which could be used to derive tissue material responses using inverse finite element analysis [226] as well as to validate the simulation results.

A.4.1 Limitations

Several assumptions and simplifications were made in the present study. Both human and porcine tissues were frozen prior to testing. Therefore, the structural properties obtained might be different than those of fresh tissues. Due to the limited sample size, we were not able to identify any correlation between structural properties to age, gender and disease states such as hypertension. The graphite markers on the LCS and RCS might not be affixed in the central area of the sinus due to the presence of the coronary arteries. In addition, the structural properties of the AA were measured approximately 5 - 10 mm above the NCS. We also assumed that the material properties of this region were not varied along the CIRC direction. The anterior and posterior regions of AA tissues were reported to be similar in the studies by Gundiah et al. and Azadani et al. [25, 26].

A.5 Conclusion

In this appendix, the regional structural compliance of aged human and porcine aortic tissues was quantified. The experimental results of ten aged human hearts revealed no significant difference in stiffness among the sinuses in both directions. The regional structural stiffness of human aortas in CIRC direction varied with the LS being the stiffest in left and right sinuses. The NCS regions were uniform in stiffness in both CIRC and LONG directions. The asymmetric structural properties were observed among porcine aortic sinuses, with the NCS being the stiffest in the CIRC direction and the RCS being the least stiff in both directions. Stiffness in porcine lower regions was higher than middle, upper sinuses and ascending aortas in the CIRC direction. Aged human aortic tissues were significantly stiffer than 6-9 months old porcine aortic tissues, indicating that the mechanical properties of porcine may not be analogous to aged human ones. These observations suggest that clinical interpretations of animal trials on prosthetic devices should be determined with caution.

REFERENCES

[1] AHA, "American Heart Association: Heart Disease and Stroke Statistics—2010 Update," 2010.

[2] C. M. Otto and R. O. Bonow, *Valvular Heart Disease: A Companion to Braunwald's Heart Disease,* 3rd ed. Philadelphia: Saunders, 2009.

[3] B. A. Carabello and W. J. Paulus, "Aortic stenosis," *Lancet,* vol. 373, pp. 956-66, 2009.

[4] W. D. Merryman, "Mechano-potential etiologies of aortic valve disease," *Journal of Biomechanics,* vol. 43, pp. 87-92, 2010.

[5] B. F. Stewart, D. Siscovick, B. K. Lind, J. M. Gardin, J. S. Gottdiener, V. E. Smith, *et al.*, "Clinical factors associated with calcific aortic valve disease. Cardiovascular Health Study," *Journal of the American College of Cardiology,* vol. 29, pp. 630-4, 1997.

[6] M. Lindroos, M. Kupari, J. Heikkila, and R. Tilvis, "Prevalence of aortic valve abnormalities in the elderly: an echocardiographic study of a random population sample," *J Am Coll Cardiol,* vol. 21, pp. 1220-5, Apr 1993.

[7] P. Libby, R. O. Bonow, D. P. Zipes, and D. L. Mann, *Braunwald's Heart Disease: A Textbook of Cardiovascular Medicine*, 9th ed. Philadelphia, PA: Saunders, an imprint of Elsevier, 2011.

[8] M. B. Leon, C. R. Smith, M. Mack, D. C. Miller, J. W. Moses, L. G. Svensson*, et al.*, "Transcatheter aortic-valve implantation for aortic stenosis in patients who cannot undergo surgery," *New England Journal of Medicine,* vol. 363, pp. 1597-1607, 2010.

[9] B. A. Carabello and W. J. Paulus, "Aortic stenosis," *The Lancet,* vol. 373, pp. 956-966.

[10] D. R. Holmes Jr, M. J. Mack, S. Kaul, A. Agnihotri, K. P. Alexander, S. R. Bailey, *et al.*, "2012 ACCF/AATS/SCAI/STS Expert Consensus Document on Transcatheter Aortic Valve Replacement," *Journal of the American College of Cardiology,* vol. 59, pp. 1200-1254, 2012.

[11] (2009). *US market for cardiac surgery devices*.

[12] A. S. Go, D. Mozaffarian, V. L. Roger, E. J. Benjamin, J. D. Berry, W. B. Borden, *et al.*, "Heart Disease and Stroke Statistics—2013 Update: A Report From the American Heart Association," *Circulation,* vol. 127, pp. e6-e245, January 1, 2013 2013.

[13] B. Iung, G. Baron, E. G. Butchart, F. Delahaye, C. Gohlke-Barwolf, O. W. Levang, *et al.*, "A prospective survey of patients with valvular heart disease in Europe: The Euro Heart Survey on Valvular Heart Disease," *Eur Heart J.,* vol. 24, pp. 1231-43., 2003.

[14] D. S. Bach, D. Siao, S. E. Girard, C. Duvernoy, B. D. McCallister, and S. K. Gualano, "Evaluation of Patients With Severe Symptomatic Aortic Stenosis Who Do Not Undergo Aortic Valve Replacement," *Circulation: Cardiovascular Quality and Outcomes,* vol. 2, pp. 533-539, November 1, 2009 2009.

[15] M. B. Leon, C. R. Smith, M. Mack, D. C. Miller, J. W. Moses, L. G. Svensson*, et al.*, "Transcatheter aortic-valve implantation for aortic stenosis in patients who cannot undergo surgery," *N Engl J Med,* vol. 363, pp. 1597-607, 2010.

[16] C. R. Smith, M. B. Leon, M. J. Mack, D. C. Miller, J. W. Moses, L. G. Svensson, *et al.*, "Transcatheter versus surgical aortic-valve replacement in high-risk patients," *N Engl J Med,* vol. 364, pp. 2187-98, Jun 9 2011.

[17] S. Haussig, G. Schuler, and A. Linke, "Worldwide TAVI registries: what have we learned?," *Clinical Research in Cardiology,* 2014.

[18] A. Cribier, H. Eltchaninoff, A. Bash, N. Borenstein, C. Tron, F. Bauer, *et al.*, "Percutaneous transcatheter implantation of an aortic valve prosthesis for calcific

aortic stenosis: first human case description," *Circulation*, vol. 106, pp. 3006-8, 2002.

[19] P. Blanke, U. J. Schoepf, and J. A. Leipsic, "CT in transcatheter aortic valve replacement," *Radiology*, vol. 269, pp. 650-69, Dec 2013.

[20] S. K. Kodali, M. R. Williams, C. R. Smith, L. G. Svensson, J. G. Webb, R. R. Makkar, *et al.*, "Two-Year Outcomes after Transcatheter or Surgical Aortic-Valve Replacement," *New England Journal of Medicine*, vol. 366, pp. 1686-1695, 2012.

[21] K. Milburn, V. Bapat, and M. Thomas, "Valve-in-valve implantations: is this the new standard for degenerated bioprostheses? Review of the literature," *Clinical Research in Cardiology*, pp. 1-13, 2014.

[22] J. G. Webb, M. Chandavimol, C. R. Thompson, D. R. Ricci, R. G. Carere, B. I. Munt, *et al.*, "Percutaneous aortic valve implantation retrograde from the femoral artery," *Circulation*, vol. 113, pp. 842-50, 2006.

[23] M. Padala, E. Sarin, P. Willis, V. Babaliaros, P. Block, R. Guyton, *et al.*, "An Engineering Review of Transcatheter Aortic Valve Technologies," *Cardiovascular Engineering and Technology*, vol. 1, pp. 77-87, 2010/03/01 2010.

[24] A. L. Bartorelli, D. Andreini, E. Sisillo, G. Tamborini, M. Fusari, and P. Biglioli, "Left main coronary artery occlusion after percutaneous aortic valve implantation," *Ann Thorac Surg*, vol. 89, pp. 953-5, Mar 2013.

[25] P. Genereux, S. J. Head, R. Hahn, B. Daneault, S. Kodali, M. R. Williams, *et al.*, "Paravalvular leak after transcatheter aortic valve replacement: the new Achilles' heel? A comprehensive review of the literature," *J Am Coll Cardiol*, vol. 61, pp. 1125-36, Mar 19 2013.

[26] K. Hayashida, E. Bouvier, and T. Lefevre, "Successful management of annulus rupture in transcatheter aortic valve implantation," *J Am Coll Cardiol Intv*, vol. 6, pp. 90-1, Jan 2013.

[27] K. Okuyama, H. Jilaihawi, and R. R. Makkar, "Leaflet length and left main coronary artery occlusion following transcatheter aortic valve replacement," *Catheter Cardiovasc Interv*, Jun 14 2013.

[28] S. K. Kodali, M. R. Williams, C. R. Smith, L. G. Svensson, J. G. Webb, R. R. Makkar, *et al.*, "Two-year outcomes after transcatheter or surgical aortic-valve replacement," *N Engl J Med*, vol. 366, pp. 1686-95, May 3 2012.

[29] L. Nombela-Franco, J. G. Webb, P. P. de Jaegere, S. Toggweiler, R. J. Nuis, A. E. Dager, *et al.*, "Timing, predictive factors, and prognostic value of cerebrovascular events in a large cohort of patients undergoing transcatheter aortic valve implantation," *Circulation*, vol. 126, pp. 3041-53, Dec 18 2012.

[30] R. J. Nuis, N. M. Van Mieghem, C. J. Schultz, A. Moelker, R. M. van der Boon, R. J. van Geuns, *et al.*, "Frequency and causes of stroke during or after transcatheter aortic valve implantation," *Am J Cardiol*, vol. 109, pp. 1637-43, Jun 1 2012.

[31] M. Barbanti, T. H. Yang, J. Rodes Cabau, C. Tamburino, D. A. Wood, H. Jilaihawi, *et al.*, "Anatomical and procedural features associated with aortic root rupture during balloon-expandable transcatheter aortic valve replacement," *Circulation*, vol. 128, pp. 244-53, Jul 16 2013.

[32] M. Pasic, A. Unbehaun, S. Dreysse, S. Buz, T. Drews, M. Kukucka, *et al.*, "Rupture of the device landing zone during transcatheter aortic valve implantation: a life-threatening but treatable complication," *Circ Cardiovasc Interv*, vol. 5, pp. 424-32, Jun 2012.

[33] A. Aminian, J. Lalmand, and D. Dolatabadi, "Late contained aortic root rupture and ventricular septal defect after transcatheter aortic valve implantation," *Catheter Cardiovasc Interv*, Mar 16 2012.

[34] H. B. Ribeiro, L. Nombela-Franco, M. Urena, M. Mok, S. Pasian, D. Doyle, *et al.*, "Coronary obstruction following transcatheter aortic valve implantation: a systematic review," *JACC Cardiovasc Interv*, vol. 6, pp. 452-61, May 2013.

[35] H. B. Ribeiro, J. G. Webb, R. R. Makkar, M. G. Cohen, S. R. Kapadia, S. Kodali, *et al.*, "Predictive factors, management, and clinical outcomes of coronary obstruction following transcatheter aortic valve implantation: insights from a large multicenter registry," *J Am Coll Cardiol*, vol. 62, pp. 1552-62, Oct 22 2013.

[36] M. J. Underwood, G. El Khoury, D. Deronck, D. Glineur, and R. Dion, "The aortic root: structure, function, and surgical reconstruction," *Heart,* vol. 83, pp. 376-80, Apr 2000.

[37] R. H. Anderson, W. A. Devine, S. Y. Ho, A. Smith, and R. McKay, "The myth of the aortic annulus: the anatomy of the subaortic outflow tract," *Ann Thorac Surg,* vol. 52, pp. 640-6, Sep 1991.

[38] R. H. Anderson, M. Lal, and S. Y. Ho, "Anatomy of the aortic root with particular emphasis on options for its surgical enlargement," *Journal of Heart Valve Disease*, vol. 5 Suppl 3, pp. S249-57, 1996.

[39] S. Staubach, J. Franke, U. Gerckens, G. Schuler, R. Zahn, H. Eggebrecht, *et al.*, "Impact of aortic valve calcification on the outcome of transcatheter aortic valve implantation: results from the prospective multicenter German TAVI registry," *Catheter Cardiovasc Interv,* vol. 81, pp. 348-55, Feb 2013.

[40] J. Webb, S. Pasupati, K. Humphries, C. Thompson, L. Altwegg, R. Moss, *et al.*, "Percutaneous transarterial aortic valve replacement in selected high-risk patients with aortic stenosis," *Circulation,* vol. 116, pp. 755-763, 2007.

[41] R. Gurvitch, J. G. Webb, R. Yuan, M. Johnson, C. Hague, A. B. Willson, *et al.*, "Aortic annulus diameter determination by multidetector computed tomography: reproducibility, applicability, and implications for transcatheter aortic valve implantation," *JACC Cardiovasc Interv,* vol. 4, pp. 1235-45, Nov 2011.

[42] H. Jilaihawi, N. Doctor, M. Kashif, T. Chakravarty, A. Rafique, M. Makar, *et al.*, "Aortic annular sizing for transcatheter aortic valve replacement using cross-sectional 3-dimensional transesophageal echocardiography," *J Am Coll Cardiol,* vol. 61, pp. 908-16, Mar 5 2013.

[43] A. M. Kasel, S. Cassese, S. Bleiziffer, M. Amaki, R. T. Hahn, A. Kastrati, *et al.*, "Standardized imaging for aortic annular sizing: implications for transcatheter valve selection," *JACC Cardiovasc Imaging,* vol. 6, pp. 249-62, Feb 2013.

[44] C. J. Schultz, A. D. Moelker, A. Tzikas, A. Rossi, R. J. van Geuns, P. J. de Feyter, *et al.*, "Cardiac CT: necessary for precise sizing for transcatheter aortic implantation," *EuroIntervention,* vol. 6 Suppl G, pp. G6-G13, May 2010.

[45] Q. Wang, G. Book, S. Contreras Ortiz, C. Primiano, R. McKay, S. Kodali, *et al.*, "Dimensional Analysis of Aortic Root Geometry During Diastole Using 3D Models Reconstructed from Clinical 64-Slice Computed Tomography Images," *Cardiovasc Eng Technol,* vol. 2, pp. 324-333, 2011.

[46] L. F. Tops, D. A. Wood, V. Delgado, J. D. Schuijf, J. R. Mayo, S. Pasupati, *et al.*, "Noninvasive evaluation of the aortic root with multislice computed tomography implications for transcatheter aortic valve replacement," *JACC Cardiovasc Imaging,* vol. 1, pp. 321-30, May 2008.

[47] D. A. Wood, L. F. Tops, J. R. Mayo, S. Pasupati, M. J. Schalij, K. Humphries, *et al.*, "Role of multislice computed tomography in transcatheter aortic valve replacement," *Am J Cardiol,* vol. 103, pp. 1295-301, May 1 2009.

[48] H. Jilaihawi, M. Kashif, G. Fontana, A. Furugen, T. Shiota, G. Friede, *et al.*, "Cross-sectional computed tomographic assessment improves accuracy of aortic annular sizing for transcatheter aortic valve replacement and reduces the incidence of paravalvular aortic regurgitation," *J Am Coll Cardiol,* vol. 59, pp. 1275-86, Apr 3 2012.

[49] M. B. Leon, H. Gada, and G. P. Fontana, "Challenges and future opportunities for transcatheter aortic valve therapy," *Prog Cardiovasc Dis,* vol. 56, pp. 635-45, May-Jun 2014.

[50] M. Taramasso, A. Pozzoli, A. Latib, G. La Canna, A. Colombo, F. Maisano, *et al.*, "New devices for TAVI: technologies and initial clinical experiences," *Nat Rev Cardiol,* vol. 11, pp. 157-67, Mar 2014.

[51] C. J. Schultz, A. Weustink, N. Piazza, A. Otten, N. Mollet, G. Krestin, *et al.*, "Geometry and degree of apposition of the CoreValve ReValving system with multislice computed tomography after implantation in patients with aortic stenosis," *J Am Coll Cardiol,* vol. 54, pp. 911-8, Sep 1 2009.

[52] P. Stolzmann, J. Knight, L. Desbiolles, W. Maier, H. Scheffel, A. Plass, *et al.*, "Remodelling of the aortic root in severe tricuspid aortic stenosis: implications for transcatheter aortic valve implantation," *European Radiology,* vol. 19, pp. 1316-23, 2009.

[53] C. Martin, T. Pham, and W. Sun, "Significant differences in the material properties between aged human and porcine aortic tissues," *Eur J Cardiothorac Surg,* vol. 40, pp. 28-34, 2011.

[54] C. Martin and W. Sun, "Biomechanical characterization of aortic valve tissue in humans and common animal models," *J Biomed Mater Res A,* vol. 100, pp. 1591-9, Jun 2012.

[55] N. Saikrishnan, S. Gupta, and A. Yoganathan, "Hemodynamics of the Boston Scientific Lotus™ Valve: An In Vitro Study," *Cardiovascular Engineering and Technology,* vol. 4, pp. 427-439, 2013/12/01 2013.

[56] M. Scharfschwerdt, R. Meyer-Saraei, C. Schmidtke, and H. H. Sievers, "Hemodynamics of the Edwards Sapien XT transcatheter heart valve in noncircular aortic annuli," *J Thorac Cardiovasc Surg,* vol. 148, pp. 126-32, Jul 2014.

[57] S. Stuhle, D. Wendt, G. Houl, H. Wendt, M. Schlamann, M. Thielmann, *et al.*, "In-vitro investigation of the hemodynamics of the Edwards Sapien transcatheter heart valve," *J Heart Valve Dis,* vol. 20, pp. 53-63, Jan 2011.

[58] A. Ducci, S. Tzamtzis, M. J. Mullen, and G. Burriesci, "Hemodynamics in the Valsalva sinuses after transcatheter aortic valve implantation (TAVI)," *J Heart Valve Dis,* vol. 22, pp. 688-96, Sep 2013.

[59] M. Kuetting, A. Sedaghat, M. Utzenrath, J. M. Sinning, C. Schmitz, J. Roggenkamp, *et al.*, "In vitro assessment of the influence of aortic annulus ovality on the hydrodynamic performance of self-expanding transcatheter heart valve prostheses," *J Biomech,* vol. 47, pp. 957-65, Mar 21 2014.

[60] P. S. Gunning, N. Saikrishnan, L. M. McNamara, and A. P. Yoganathan, "An in vitro evaluation of the impact of eccentric deployment on transcatheter aortic valve hemodynamics," *Ann Biomed Eng,* vol. 42, pp. 1195-206, Jun 2014.

[61] E. M. Groves, A. Falahatpisheh, J. L. Su, and A. Kheradvar, "The Effects of Positioning of Transcatheter Aortic Valve on Fluid Dynamics of the Aortic Root," *ASAIO J,* Jul 9 2014.

[62] H. Maleki, S. Shahriari, M. Labrosse, P. Pibarot, and L. Kadem, "An In Vitro Model of Aortic Stenosis for the Assessment of Transcatheter Aortic Valve Implantation," *J Biomech Eng,* vol. 136, May 1 2014.

[63] T. E. Claiborne, J. Sheriff, M. Kuetting, U. Steinseifer, M. J. Slepian, and D. Bluestein, "In vitro evaluation of a novel hemodynamically optimized trileaflet polymeric prosthetic heart valve," *J Biomech Eng,* vol. 135, p. 021021, Feb 2013.

[64] K. Li, Q. Wang, T. Pham, and W. Sun, "Quantification of structural compliance of aged human and porcine aortic root tissues," *J Biomed Mater Res A,* Jul 27 2013.

[65] J. Mummert, E. Sirois, and W. Sun, "Quantification of biomechanical interaction of transcatheter aortic valve stent deployed in porcine and ovine hearts," *Ann Biomed Eng,* vol. 41, pp. 577-86, Mar 2013.

[66] N. Saikrishnan, G. Kumar, F. J. Sawaya, S. Lerakis, and A. P. Yoganathan, "Accurate Assessment of Aortic Stenosis: A Review of Diagnostic Modalities and Hemodynamics," *Circulation,* vol. 129, pp. 244-253, January 14, 2014 2014.

[67] P. Schoenhagen, A. Hill, T. Kelley, Z. Popovic, and S. S. Halliburton, "In vivo imaging and computational analysis of the aortic root. Application in clinical research and design of transcatheter aortic valve systems," *J Cardiovasc Transl Res,* vol. 4, pp. 459-69, Aug 2011.

[68] K. Li and W. Sun, "Simulated thin pericardial bioprosthetic valve leaflet deformation under static pressure-only loading conditions: implications for percutaneous valves," *Ann Biomed Eng,* vol. 38, pp. 2690-701, Aug 2010.

[69] A. N. Smuts, D. C. Blaine, C. Scheffer, H. Weich, A. F. Doubell, and K. H. Dellimore, "Application of finite element analysis to the design of tissue leaflets for a percutaneous aortic valve," *J Mech Behav Biomed Mater,* vol. 4, pp. 85-98, Jan 2010.

[70] W. Sun, K. Li, and E. Sirois, "Simulated elliptical bioprosthetic valve deformation: implications for asymmetric transcatheter valve deployment," *Journal of Biomechanics,* vol. 43, pp. 3085-90, 2010.

[71] M. Gessat, L. Altwegg, T. Frauenfelder, A. Plass, and V. Falk, "Cubic hermite bezier spline based reconstruction of implanted aortic valve stents from CT images," in *Engineering in Medicine and Biology Society,EMBC, 2011 Annual International Conference of the IEEE*, 2011, pp. 2667-2670.

[72] M. Gessat, R. Hopf, T. Pollok, C. Russ, T. Frauenfelder, S. H. Sundermann, *et al.*, "Image-Based Mechanical Analysis of Stent Deformation: Concept and

Exemplary Implementation for Aortic Valve Stents," *Biomedical Engineering, IEEE Transactions on,* vol. 61, pp. 4-15, 2014.

[73] S. Tzamtzis, J. Viquerat, J. Yap, M. J. Mullen, and G. Burriesci, "Numerical analysis of the radial force produced by the Medtronic-CoreValve and Edwards-SAPIEN after transcatheter aortic valve implantation (TAVI)," *Med Eng Phys,* vol. 35, pp. 125-30, Jan 2013.

[74] C. Capelli, G. M. Bosi, E. Cerri, J. Nordmeyer, T. Odenwald, P. Bonhoeffer, *et al.*, "Patient-specific simulations of transcatheter aortic valve stent implantation," *Med Biol Eng Comput,* vol. 50, pp. 183-92, 2012.

[75] Q. Wang, E. Sirois, and W. Sun, "Patient-specific modeling of biomechanical interaction in transcatheter aortic valve deployment," *J Biomech,* vol. 45, pp. 1965-71, Jul 26 2012.

[76] F. Auricchio, M. Conti, S. Morganti, and A. Reali, "Simulation of transcatheter aortic valve implantation: a patient-specific finite element approach," *Comput Methods Biomech Biomed Engin,* Feb 13 2013.

[77] P. S. Gunning, T. J. Vaughan, and L. M. McNamara, "Simulation of Self Expanding Transcatheter Aortic Valve in a Realistic Aortic Root: Implications of Deployment Geometry on Leaflet Deformation," *Ann Biomed Eng,* Jun 10 2014.

[78] S. Morganti, M. Conti, M. Aiello, A. Valentini, A. Mazzola, A. Reali, *et al.*, "Simulation of transcatheter aortic valve implantation through patient-specific finite element analysis: Two clinical cases," *Journal of Biomechanics,* vol. 47, pp. 2547-2555, 8/22/ 2014.

[79] S. Grbic, T. Mansi, R. Ionasec, I. Voigt, H. Houle, M. John, *et al.*, "Image-based computational models for TAVI planning: from CT images to implant deployment," *Med Image Comput Comput Assist Interv,* vol. 16, pp. 395-402, 2013.

[80] Q. Wang, S. Kodali, C. Primiano, and W. Sun, "Simulations of transcatheter aortic valve implantation: implications for aortic root rupture," *Biomechanics and Modeling in Mechanobiology,* pp. 1-10, 2014/04/16 2014.

[81] Q. Wang, C. Primiano, R. McKay, S. Kodali, and W. Sun, "CT Image-Based Engineering Analysis of Transcatheter Aortic Valve Replacement," *JACC: Cardiovascular Imaging,* vol. 7, pp. 526-528, 2014.

[82] H. A. Dwyer, P. B. Matthews, A. Azadani, N. Jaussaud, L. Ge, T. S. Guy, *et al.*, "Computational fluid dynamics simulation of transcatheter aortic valve degeneration," *Interact Cardiovasc Thorac Surg,* vol. 9, pp. 301-8, Aug 2009.

[83] H. A. Dwyer, P. B. Matthews, A. Azadani, L. Ge, T. S. Guy, and E. E. Tseng, "Migration forces of transcatheter aortic valves in patients with noncalcific aortic insufficiency," *Journal of Thoracic & Cardiovascular Surgery,* vol. 138, pp. 1227-33, 2009.

[84] E. Sirois, Q. Wang, and W. Sun, "Fluid Simulation of a Transcatheter Aortic Valve Deployment into a Patient-Specific Aortic Root," *Cardiovascular Engineering and Technology,* vol. 2, pp. 186-195, 2011.

[85] M. S. Sacks, "Biaxial mechanical evaluation of planar biological materials," *Journal of Elasticity,* vol. 61, pp. 199-246, 2000.

[86] Y. C. Fung, *Biomechanics: Mechanical Properties of Living Tissues*, 2nd ed. New York: Springer Verlag, 1993.

[87] A. Cataloglu, R. E. Clark, and P. L. Gould, "Stress analysis of aortic valve leaflets with smoothed geometrical data," *Journal of Biomechanics,* vol. 10, pp. 153-158, 1977.

[88] K. S. Kunzelman, R. P. Cochran, C. Chuong, W. S. Ring, E. D. Verrier, and R. D. Eberhart, "Finite element analysis of the mitral valve," *The Journal of heart valve disease,* vol. 2, pp. 326-340, 1993.

[89] A. M. Pouch, C. Xu, P. A. Yushkevich, A. S. Jassar, M. Vergnat, J. H. Gorman, 3rd, *et al.*, "Semi-automated mitral valve morphometry and computational stress analysis using 3D ultrasound," *J Biomech*, vol. 45, pp. 903-7, Mar 15 2012.

[90] M. Stevanella, G. Krishnamurthy, E. Votta, J. C. Swanson, A. Redaelli, and N. B. Ingels, Jr., "Mitral leaflet modeling: Importance of in vivo shape and material properties," *J Biomech*, vol. 44, pp. 2229-35, Aug 11 2011.

[91] E. Votta, F. Maisano, S. F. Bolling, O. Alfieri, F. M. Montevecchi, and A. Redaelli, "The Geoform Disease-Specific Annuloplasty System: A Finite Element Study," *Annals of Thoracic Surgery*, vol. 84, pp. 92-101, 2007.

[92] G. Krishnamurthy, D. B. Ennis, A. Itoh, W. Bothe, J. C. Swanson, M. Karlsson, *et al.*, "Material properties of the ovine mitral valve anterior leaflet in vivo from inverse finite element analysis," *American Journal of Physiology - Heart and Circulatory Physiology*, vol. 295, pp. H1141-H1149, 2008.

[93] J. D. Humphery, *Cardiovascular Solid Mechanics*: Springer Verlag, 2002.

[94] W. Sun, A. Abad, and M. S. Sacks, "Simulated bioprosthetic heart valve deformation under quasi-static loading," *J Biomech Eng*, vol. 127, pp. 905-14, 2005 Nov 2005.

[95] M. S. Sacks and W. Sun, "Multiaxial Mechanical Behavior of Biological Materials," *Annu Rev Biomed Eng*, Apr 18 2003.

[96] M. R. Labrosse, K. Lobo, and C. J. Beller, "Structural analysis of the natural aortic valve in dynamics: From unpressurized to physiologically loaded," *Journal of Biomechanics*, vol. 43, pp. 1916-1922, 2010.

[97] M. R. Labrosse, M. Boodhwani, B. Sohmer, and C. J. Beller, "Modeling leaflet correction techniques in aortic valve repair: A finite element study," *Journal of Biomechanics*, vol. 44, pp. 2292-2298, 2011.

[98] J. A. Weiss, B. N. Maker, and S. Govindjee, "Finite element implementation of incompressible, transversely isotropic hyperelasticity," *Computer Methods in Applied Mechanics and Engineering,* vol. 135, pp. 107-128, Aug 15 1996.

[99] G. A. Holzapfel, T. C. Gasser , and R. W. Ogden, "A new constitutive framework for arterial wall mechanics and a comparative study of material models," *J. Elasticity,* vol. 61, pp. 1–48, 2000.

[100] V. Prot, B. Skallerud, G. Sommer, and G. A. Holzapfel, "On modelling and analysis of healthy and pathological human mitral valves: two case studies," *Journal of the mechanical behavior of biomedical materials,* vol. 3, pp. 167-177, 2010.

[101] M. Stevanella, F. Maffessanti, C. A. Conti, E. Votta, A. Arnoldi, M. Lombardi*, et al.*, "Mitral Valve Patient-Specific Finite Element Modeling from Cardiac MRI: Application to an Annuloplasty Procedure," *Cardiovascular Engineering and Technology,* vol. 2, pp. 66-76, 2011.

[102] K. May-Newman and F. C. Yin, "A constitutive law for mitral valve tissue," *J Biomech Eng,* vol. 120, pp. 38-47, Feb 1998.

[103] C. A. Conti, E. Votta, A. Della Corte, L. Del Viscovo, C. Bancone, M. Cotrufo*, et al.*, "Dynamic finite element analysis of the aortic root from MRI-derived parameters," *Med Eng Phys,* vol. 32, pp. 212-21, Mar 2010.

[104] F. Auricchio, M. Conti, S. Morganti, and A. Reali, "Simulation of transcatheter aortic valve implantation: a patient-specific finite element approach," *Computer Methods in Biomechanics and Biomedical Engineering,* 2013.

[105] J. C. Cornily, M. Gilard, E. Bezon, V. Jan, P. Y. Pennec, Y. Etienne*, et al.*, "Cardiac multislice spiral computed tomography as an alternative to coronary angiography in the preoperative assessment of coronary artery disease before aortic valve surgery: a management outcome study," *Archives of cardiovascular diseases,* vol. 103, pp. 170-5, 2010.

[106] D. Fleischmann, D. H. Liang, R. S. Mitchell, and D. C. Miller, "Pre- and postoperative imaging of the aortic root for valve-sparing aortic root repair (V-SARR)," *Seminars in Thoracic & Cardiovascular Surgery,* vol. 20, pp. 365-73, 2008.

[107] E. Grube, J. C. Laborde, U. Gerckens, T. Felderhoff, B. Sauren, L. Buellesfeld*, et al.*, "Percutaneous implantation of the CoreValve self-expanding valve prosthesis in high-risk patients with aortic valve disease: the Siegburg first-in-man study," *Circulation,* vol. 114, pp. 1616-24, 2006.

[108] F. R. de Graaf, J. D. Schuijf, V. Delgado, J. E. van Velzen, L. J. Kroft, A. de Roos*, et al.*, "Clinical application of CT coronary angiography: state of the art," *Heart Lung Circ,* vol. 19, pp. 107-16, Mar 2010.

[109] J. K. Willmann, D. Weishaupt, M. Lachat, R. Kobza, J. E. Roos, B. Seifert*, et al.*, "Electrocardiographically gated multi-detector row CT for assessment of valvular morphology and calcification in aortic stenosis," *Radiology,* vol. 225, pp. 120-8, 2002.

[110] L. F. Tops, D. A. Wood, V. Delgado, J. D. Schuijf, J. R. Mayo, S. Pasupati*, et al.*, "Noninvasive evaluation of the aortic root with multislice computed tomography implications for transcatheter aortic valve replacement," *Jacc: Cardiovascular Imaging,* vol. 1, pp. 321-30, 2008.

[111] K. S. Martin, Will; Lorensen, Bill, "Visualization Toolkit (VTK)," ed: Kitware, Inc, 2009.

[112] M. Akhtar, E. M. Tuzcu, S. R. Kapadia, L. G. Svensson, R. K. Greenberg, E. E. Roselli*, et al.*, "Aortic root morphology in patients undergoing percutaneous aortic valve replacement: evidence of aortic root remodeling," *Journal of Thoracic & Cardiovascular Surgery,* vol. 137, pp. 950-6, 2009.

[113] M. Akhtar, E. M. Tuzcu, S. R. Kapadia, L. G. Svensson, R. K. Greenberg, E. E. Roselli*, et al.*, "Aortic root morphology in patients undergoing percutaneous

aortic valve replacement: evidence of aortic root remodeling," *J Thorac Cardiovasc Surg,* vol. 137, pp. 950-6, Apr 2009.

[114] D. Messika-Zeitoun, J. M. Serfaty, E. Brochet, G. Ducrocq, L. Lepage, D. Detaint*, et al.*, "Multimodal assessment of the aortic annulus diameter: implications for transcatheter aortic valve implantation," *J Am Coll Cardiol,* vol. 55, pp. 186-94, Jan 19 2010.

[115] C. J. Schultz, A. Moelker, N. Piazza, A. Tzikas, A. Otten, R. J. Nuis*, et al.*, "Three dimensional evaluation of the aortic annulus using multislice computer tomography: are manufacturer's guidelines for sizing for percutaneous aortic valve replacement helpful?," *Eur Heart J,* Dec 7 2009.

[116] V. Delgado, A. C. Ng, M. Shanks, F. van der Kley, J. D. Schuijf, N. R. van de Veire*, et al.*, "Transcatheter aortic valve implantation: role of multimodality cardiac imaging," *Expert Rev Cardiovasc Ther,* vol. 8, pp. 113-23, Jan 2010.

[117] V. Delgado, A. C. Ng, J. D. Schuijf, F. van der Kley, M. Shanks, L. F. Tops*, et al.*, "Automated assessment of the aortic root dimensions with multidetector row computed tomography," *Annals of Thoracic Surgery,* vol. 91, pp. 716-23, 2010.

[118] T. Kazui, H. Izumoto, K. Yoshioka, and K. Kawazoe, "Dynamic morphologic changes in the normal aortic annulus during systole and diastole," *Journal of Heart Valve Disease,* vol. 15, pp. 617-21, 2006.

[119] R. Gurvitch, D. A. Wood, E. L. Tay, J. Leipsic, J. Ye, S. V. Lichtenstein*, et al.*, "Transcatheter aortic valve implantation: durability of clinical and hemodynamic outcomes beyond 3 years in a large patient cohort," *Circulation,* vol. 122, pp. 1319-27, Sep 28 2010.

[120] J. G. Webb, L. Altwegg, R. H. Boone, A. Cheung, J. Ye, S. Lichtenstein*, et al.*, "Transcatheter aortic valve implantation: impact on clinical and valve-related outcomes," *Circulation,* vol. 119, pp. 3009-16, 2009.

[121] J. Ye, A. Cheung, S. V. Lichtenstein, F. Nietlispach, S. Albugami, J. B. Masson, *et al.*, "Transapical transcatheter aortic valve implantation: follow-up to 3 years," *J Thorac Cardiovasc Surg,* vol. 139, pp. 1107-13, 1113 e1, May 2010.

[122] A. Zajarias and A. G. Cribier, "Outcomes and safety of percutaneous aortic valve replacement," *J Am Coll Cardiol,* vol. 53, pp. 1829-36, May 19 2009.

[123] E. Grube, G. Schuler, L. Buellesfeld, U. Gerckens, A. Linke, P. Wenaweser, *et al.*, "Percutaneous aortic valve replacement for severe aortic stenosis in high-risk patients using the second- and current third-generation self-expanding CoreValve prosthesis: device success and 30-day clinical outcome," *J Am Coll Cardiol.,* vol. 50, pp. 69-76, 2007.

[124] F. Auricchio, M. Conti, S. Morganti, and P. Totaro, "A computational tool to support pre-operative planning of stentless aortic valve implant," *Med Eng Phys,* Jun 7 2011.

[125] M. R. Labrosse, K. Lobo, and C. J. Beller, "Structural analysis of the natural aortic valve in dynamics: from unpressurized to physiologically loaded," *J Biomech,* vol. 43, pp. 1916-22, Jul 20 2010.

[126] A. Mangini, M. G. Lemma, M. Soncini, E. Votta, M. Contino, R. Vismara, *et al.*, "The aortic interleaflet triangles annuloplasty: a multidisciplinary appraisal," *Eur J Cardiothorac Surg,* Feb 10 2011.

[127] R. Haj-Ali, L. P. Dasi, H. S. Kim, J. Choi, H. W. Leo, and A. P. Yoganathan, "Structural simulations of prosthetic tri-leaflet aortic heart valves," *Journal of Biomechanics,* vol. 41, pp. 1510-9, 2008.

[128] G. V. Kumar and L. Mathew, "Effects of design parameters on the radial force of percutaneous aortic valve stents," *Cardiovasc Revasc Med,* vol. 11, pp. 101-4, Apr-Jun 2010.

[129] J. G. Webb, S. Pasupati, L. Achtem, and C. R. Thompson, "Rapid pacing to facilitate transcatheter prosthetic heart valve implantation," *Catheterization & Cardiovascular Interventions*, vol. 68, pp. 199-204, 2006.

[130] J. Lu, X. Zhou, and M. L. Raghavan, "Inverse method of stress analysis for cerebral aneurysms," *Biomechanics & Modeling in Mechanobiology*, vol. 7, pp. 477-86, 2008.

[131] L. Speelman, E. M. Bosboom, G. W. Schurink, J. Buth, M. Breeuwer, M. J. Jacobs, *et al.*, "Initial stress and nonlinear material behavior in patient-specific AAA wall stress analysis," *Journal of Biomechanics*, vol. 42, pp. 1713-9, 2009.

[132] M. B. Leon, C. R. Smith, M. Mack, D. C. Miller, J. W. Moses, L. G. Svensson, *et al.*, "Transcatheter aortic-valve implantation for aortic stenosis in patients who cannot undergo surgery," *New England Journal of Medicine*, vol. 363, pp. 1597-607, 2010.

[133] R. V. Marrey, R. Burgermeister, R. B. Grishaber, and R. O. Ritchie, "Fatigue and life prediction for cobalt-chromium stents: A fracture mechanics analysis," *Biomaterials*, vol. 27, pp. 1988-2000, 2006.

[134] T. C. Gasser, R. W. Ogden, and G. A. Holzapfel, "Hyperelastic modelling of arterial layers with distributed collagen fibre orientations," *Journal of the Royal Society Interface*, vol. 3, pp. 15-35, 2006.

[135] M. S. Sacks and W. Sun, "Multiaxial mechanical behavior of biological materials," *Annu Rev Biomed Eng*, vol. 5, pp. 251-84, 2003.

[136] C. Sanchez-Giron, M. De Icaza Herrera, H. Eltchaninoff, M. Godin, C. Tron, B. Baala, *et al.*, "Circularity Index in deployed Edwards Sapien aortic valve bioprosthesis," *European Heart Journal*, p. 920, 2009

[137] S. Vad, A. Eskinazi, T. Corbett, T. McGloughlin, and J. P. Vande Geest, "Determination of coefficient of friction for self-expanding stent-grafts," *J Biomech Eng*, vol. 132, p. 121007, 2010.

[138] Q. Wang, G. Book, S. Contreras Ortiz, C. Primiano, R. McKay, S. Kodali, *et al.*, "Dimensional Analysis of Aortic Root Geometry During Diastole Using 3D Models Reconstructed from Clinical 64-Slice Computed Tomography Images," *Cardiovascular Engineering and Technology,* pp. 1-10, 2011.

[139] X. Zhou, M. L. Raghavan, R. E. Harbaugh, and J. Lu, "Patient-specific wall stress analysis in cerebral aneurysms using inverse shell model," *Annals of Biomedical Engineering,* vol. 38, pp. 478-89, 2010.

[140] Y. C. Fung, S. Q. Liu, and J. B. Zhou, "Remodeling of the constitutive equation while a blood vessel remodels itself under stress," *J Biomech Eng,* vol. 115, pp. 453-9, Nov 1993.

[141] F. Hauck, D. Wendt, W. Muller, S. Stuhle, H. Wendt, M. Thielmann, *et al.*, "A new tool for the resection of aortic valves: In-vitro results for turning moments and forces using Nitinol cutting edges," *Minim Invasive Ther Allied Technol,* vol. 18, pp. 164-71, 2009.

[142] R. Zegdi, V. Ciobotaru, M. Noghin, G. Sleilaty, A. Lafont, C. Latremouille, *et al.*, "Is it reasonable to treat all calcified stenotic aortic valves with a valved stent? Results from a human anatomic study in adults," *Journal of the American College of Cardiology,* vol. 51, pp. 579-84, 2008.

[143] D. M. Ebenstein, D. Coughlin, J. Chapman, C. Li, and L. A. Pruitt, "Nanomechanical properties of calcification, fibrous tissue, and hematoma from atherosclerotic plaques," *J Biomed Mater Res A,* vol. 91, pp. 1028-37, 2009.

[144] G. A. Holzapfel, G. Sommer, and P. Regitnig, "Anisotropic mechanical properties of tissue components in human atherosclerotic plaques," *J Biomech Eng,* vol. 126, pp. 657-65, 2004.

[145] M. Jeziorska, C. McCollum, and D. E. Wooley, "Observations on bone formation and remodelling in advanced atherosclerotic lesions of human carotid arteries," *Virchows Archiv,* vol. 433, pp. 559-65, 1998.

[146] A. Eker, F. B. Sozzi, F. Civaia, and F. Bourlon, "Aortic annulus rupture during transcatheter aortic valve implantation: safe aortic root replacement," *Eur J Cardiothorac Surg,* vol. 41, p. 1205, May 2012.

[147] K. Hayashida, E. Bouvier, T. Lefevre, T. Hovasse, M. C. Morice, B. Chevalier*, et al.*, "Potential mechanism of annulus rupture during transcatheter aortic valve implantation," *Catheter Cardiovasc Interv,* Jun 21 2012.

[148] L. Lee, R. Henderson, and K. Baig, "Successful treatment of aortic root rupture following transcatheter aortic valve implantation in a heavily calcified aorta: A novel approach to a serious complication," *Catheter Cardiovasc Interv,* Apr 25 2012.

[149] A. Rezq, S. Basavarajaiah, A. Latib, K. Takagi, T. Hasegawa, F. Figini*, et al.*, "Incidence, management, and outcomes of cardiac tamponade during transcatheter aortic valve implantation: a single-center study," *JACC Cardiovasc Interv,* vol. 5, pp. 1264-72, Dec 2012.

[150] R. Lange, S. Bleiziffer, N. Piazza, D. Mazzitelli, A. Hutter, P. Tassani-Prell*, et al.*, "Incidence and treatment of procedural cardiovascular complications associated with trans-arterial and trans-apical interventional aortic valve implantation in 412 consecutive patients," *Eur J Cardiothorac Surg,* vol. 40, pp. 1105-13, 2011.

[151] C. Russ, R. Hopf, S. Hirsch, S. Sundermann, V. Falk, G. Szekely*, et al.*, "Simulation of transcatheter aortic valve implantation under consideration of leaflet calcification," in *Engineering in Medicine and Biology Society (EMBC), 2013 35th Annual International Conference of the IEEE*, 2013, pp. 711-714.

[152] T. C. Gasser, R. W. Ogden, and G. A. Holzapfel, "Hyperelastic modelling of arterial layers with distributed collagen fibre orientations," *J R Soc Interface,* vol. 3, pp. 15-35, 2006.

[153] R. W. Ogden, "Large Deformation Isotropic Elasticity - On the Correlation of Theory and Experiment for Incompressible Rubberlike Solids," *Proc R Soc Lond A* vol. 326, pp. 565-584, February 1, 1972 1972.

[154] M. Samim, P. R. Stella, P. Agostoni, J. Kluin, F. Ramjankhan, G. Sieswerda, *et al.*, "A prospective "oversizing" strategy of the Edwards SAPIEN bioprosthesis: Results and impact on aortic regurgitation," *J Thorac Cardiovasc Surg,* Feb 27 2012.

[155] D. Berdajs, "Aortic root rupture: implications of catheter-guided aortic valve replacement," *Curr Opin Cardiol,* vol. 28, pp. 632-8, Nov 2013.

[156] A. Cribier, H. Eltchaninoff, and N. Borenstein, "Trans-catheter implantation of balloon-expandable prosthetic heart valves: Early results in an animal model " *Circulation,* vol. 104 (SUPPL. 11), pp. 11-552, 2001.

[157] G. Lutter, D. Kuklinski, G. Berg, P. Von Samson, J. Martin, M. Handke, *et al.*, "Percutaneous aortic valve replacement: an experimental study. I. Studies on implantation," *J Thorac Cardiovasc Surg,* vol. 123, pp. 768-76, Apr 2002.

[158] T. M. Dewey, T. Walther, M. Doss, D. Brown, W. H. Ryan, L. Svensson, *et al.*, "Transapical aortic valve implantation: an animal feasibility study," *Ann Thorac Surg,* vol. 82, pp. 110-6, Jul 2006.

[159] T. Pham and W. Sun, "Comparison of biaxial mechanical properties of coronary sinus tissues from porcine, ovine and aged human species," *J Mech Behav Biomed Mater,* vol. 6, pp. 21-9, Feb 2012.

[160] T. Pham and W. Sun, "Material properties of aged human mitral valve leaflets," *J Biomed Mater Res A,* Aug 30 2013.

[161] M. Leon, C. Smith, M. Mack, D. Miller, J. Moses, L. Svensson, *et al.*, "Transcatheter aortic-valve implantation for aortic stenosis in patients who cannot undergo surgery," *N Engl J Med,* vol. 363, pp. 1597-607., 2010.

[162] R. Del Valle-Fernández, C. Martinez, and C. Ruiz, "Transcatheter aortic valve implantation," *Cardiol Clin.,* vol. 28, pp. 155-68, 2010.

[163] J. Webb, S. Pasupati, K. Humphries, C. Thompson, L. Altwegg, R. Moss, *et al.*, "Percutaneous transarterial aortic valve replacement in selected high-risk patients with aortic stenosis," *Circulation,* vol. 7, pp. 755-763, 2007.

[164] E. Grube, G. Schuler, L. Buellesfeld, U. Gerckens, A. Linke, P. Wenaweser, *et al.*, "Percutaneous aortic valve replacement for severe aortic stenosis in high-risk patients using the second- and current third-generation self-expanding CoreValve prosthesis: device success and 30-day clinical outcome," *J Am Coll Cardiol. ,* vol. 1, pp. 69-76, 2007.

[165] J. Ye, A. Cheung, S. V. Lichtenstein, R. G. Carere, C. R. Thompson, S. Pasupati, *et al.*, "Transapical aortic valve implantation in humans," *Journal of Thoracic and Cardiovascular Surgery,* vol. 131, pp. 1194-1196, 2006.

[166] J. Ye, A. Cheung, S. V. Lichtenstein, F. Nietlispach, S. Albugami, J. B. Masson, *et al.*, "Transapical transcatheter aortic valve implantation: Follow-up toÂ 3 years," *Journal of Thoracic and Cardiovascular Surgery,* vol. 139, pp. 1107-1113.e1, 2010.

[167] N. C. Dang, M. S. Aboodi, T. Sakaguchi, H. S. Wasserman, M. Argenziano, D. M. Cosgrove, *et al.*, "Surgical revision after percutaneous mitral valve repair with a clip: initial multicenter experience," *Ann Thorac Surg.,* vol. 80, pp. 2338-42., 2005.

[168] H. Dwyer, P. Matthews, A. Azadani, L. Ge, T. Guy, and E. Tseng, "Migration forces of transcatheter aortic valves in patients with noncalcific aortic insufficiency.," *J Thorac Cardiovasc Surg.,* vol. 138, pp. 1227-33, 2009.

[169] M. S. Sacks and F. J. Schoen, "Collagen fiber disruption occurs independent of calcification in clinically explanted bioprosthetic heart valves," *J Biomed Mater Res,* vol. 62, pp. 359-71, Dec 5 2002.

[170] F. Schoen and R. Levy, "Tissue heart valves: Current challenges and future research perspectives," *Journal of Biomedical Materials Research,* vol. 47, pp. 439-465, 1999.

[171] W. Sun, K. Li, and E. Sirois, "Simulated elliptical bioprosthetic valve deformation: Implications for asymmetric transcatheter valve deployment," *Journal of Biomechanics,* vol. 43, pp. 3085-3090, 2010.

[172] F. Auricchio, "A robust integration-algorithm for a finite-strain shape-memory-alloy superelastic model," *International Journal of Plasticity,* vol. 17, pp. 971-990, 7// 2001.

[173] M. W. Gee, C. Reeps, H. H. Eckstein, and W. A. Wall, "Prestressing in finite deformation abdominal aortic aneurysm simulation," *Journal of Biomechanics,* vol. 42, pp. 1732-1739, 2009.

[174] J. Lu, X. Zhou, and M. L. Raghavan, "Inverse method of stress analysis for cerebral aneurysms," *Biomechanics and Modeling in Mechanobiology,* vol. 7, pp. 477-486, 2008.

[175] K. S. Kunzelman, D. R. Einstein, and R. P. Cochran, "Fluid-structure interaction models of the mitral valve: function in normal and pathological states," *Philos Trans R Soc Lond B Biol Sci,* vol. 362, pp. 1393-406, Aug 29 2007.

[176] M. Nicosia, R. P. Cochran, D. R. Einstein, C. J. Rutland, and K. S. Kunzelman, "A coupled fluid-structure finite element model of the aortic valve and root," *J Heart Valve Dis,* vol. 12, pp. 781-9, 2003

[177] M. Y. S. Kuan and D. M. Espino, "Systolic fluid–structure interaction model of the congenitally bicuspid aortic valve: assessment of modelling requirements," *Computer Methods in Biomechanics and Biomedical Engineering,* pp. 1-16, 2014.

[178] G. Marom, M. Peleg, R. Halevi, M. Rosenfeld, E. Raanani, A. Hamdan, *et al.*, "Fluid-Structure Interaction Model of Aortic Valve With Porcine-Specific

Collagen Fiber Alignment in the Cusps," *Journal of Biomechanical Engineering,* vol. 135, pp. 101001-101001, 2013.

[179] S. Nobari, R. Mongrain, R. Leask, and R. Cartier, "The effect of aortic wall and aortic leaflet stiffening on coronary hemodynamic: a fluid–structure interaction study," *Medical & Biological Engineering & Computing,* vol. 51, pp. 923-936, 2013/08/01 2013.

[180] K. D. Lau, V. Diaz, P. Scambler, and G. Burriesci, "Mitral valve dynamics in structural and fluid–structure interaction models," *Medical Engineering & Physics,* vol. 32, pp. 1057-1064, 11// 2010.

[181] R. Chandola, R. Cusimano, M. Osten, and E. Horlick, "Postcardiac Transplant Transcatheter Core Valve Implantation for Aortic Insufficiency Secondary to Impella Device Placement," *The Annals of Thoracic Surgery,* vol. 93, pp. e155-e157, 6// 2012.

[182] N. Dumonteil, B. Marcheix, O. Lairez, and J.-C. Laborde, "Transcatheter aortic valve implantation for severe, non-calcified aortic regurgitation and narrow aortic root: Description from a case report of a new approach to potentially avoid coronary artery obstruction," *Catheterization and Cardiovascular Interventions,* vol. 82, pp. E124-E127, 2013.

[183] M. Seiffert, P. Diemert, D. Koschyk, J. Schirmer, L. Conradi, R. Schnabel, *et al.*, "Transapical Implantation of a Second-Generation Transcatheter Heart Valve in Patients With Noncalcified Aortic Regurgitation," *JACC: Cardiovascular Interventions,* vol. 6, pp. 590-597, 6// 2013.

[184] R. Lange and N. Piazza, "Transcatheter aortic valve-in-surgical aortic valve implantation: current status and future perspectives," *European Journal of Cardio-Thoracic Surgery,* vol. 44, pp. 403-406, September 1, 2013 2013.

[185] J. G. Webb and D. Dvir, "Transcatheter Aortic Valve Replacement for Bioprosthetic Aortic Valve Failure: The Valve-in-Valve Procedure," *Circulation,* vol. 127, pp. 2542-2550, June 25, 2013 2013.

[186] R. Gurvitch, A. Cheung, J. Ye, D. A. Wood, A. B. Willson, S. Toggweiler*, et al.*, "Transcatheter Valve-in-Valve Implantation for Failed Surgical Bioprosthetic Valves," *Journal of the American College of Cardiology,* vol. 58, pp. 2196-2209, 11/15/ 2011.

[187] A. N. Azadani, S. Chitsaz, P. B. Matthews, N. Jaussaud, J. Leung, T. Tsinman*, et al.*, "Comparison of mechanical properties of human ascending aorta and aortic sinuses," *Ann Thorac Surg,* vol. 93, pp. 87-94, Jan 2012.

[188] A. W. Leber, M. Kasel, T. Ischinger, U. H. Ebersberger, D. Antoni, M. Schmidt*, et al.*, "Aortic valve calcium score as a predictor for outcome after TAVI using the CoreValve revalving system," *International Journal of Cardiology,* vol. 166, pp. 652-657, 7/1/ 2013.

[189] D. John, L. Buellesfeld, S. Yuecel, R. Mueller, G. Latsios, H. Beucher*, et al.*, "Correlation of Device Landing Zone Calcification and Acute Procedural Success in Patients Undergoing Transcatheter Aortic Valve Implantations With the Self-Expanding CoreValve Prosthesis," *JACC: Cardiovascular Interventions,* vol. 3, pp. 233-243, 2// 2010.

[190] A. J. Muñoz-García, J. H. Alonso-Briales, M. F. Jiménez-Navarro, J. Caballero-Borrego, A. J. Domínguez-Franco, I. Rodríguez-Bailón*, et al.*, "Mechanisms, treatment and course of paravalvular aortic regurgitation after percutaneous implantation of the CoreValve aortic prosthesis," *International Journal of Cardiology,* vol. 149, pp. 389-392, 6/16/ 2011.

[191] R. Koos, A. H. Mahnken, G. Dohmen, K. Brehmer, R. W. Günther, R. Autschbach*, et al.*, "Association of aortic valve calcification severity with the

degree of aortic regurgitation after transcatheter aortic valve implantation," *International Journal of Cardiology*, vol. 150, pp. 142-145, 7/15/ 2011.

[192] Q. Wang, G. Book, S. C. Ortiz, C. Primiano, R. McKay, S. Kodali, *et al.*, "Dimensional Analysis of Aortic Root Geometry During Diastole Using 3D Models Reconstructed from Clinical 64-Slice Computed Tomography Images," *Cardiovascular Engineering and Technology*, vol. 2, pp. 324-333, 2011.

[193] P. Dagum, G. R. Green, F. J. Nistal, G. T. Daughters, T. A. Timek, L. E. Foppiano, *et al.*, "Deformational dynamics of the aortic root: Modes and physiologic determinants," *Circulation*, vol. 100, 1999.

[194] B. Hansen, A. H. Menkis, and I. Vesely, "Longitudinal and radial distensibility of the porcine aortic root," *The Annals of Thoracic Surgery*, vol. 60, pp. S384-S390, 1995.

[195] E. Lansac, H. S. Lim, Y. Shomura, K. H. Lim, N. T. Rice, W. Goetz, *et al.*, "A four-dimensional study of the aortic root dynamics," *European Journal of Cardio-thoracic Surgery*, vol. 22, pp. 497-503, 2002.

[196] I. Vesely, A. H. Menkis, B. Rutt, and G. Campbell, "Aortic valve/root interactions in porcine hearts: implications for bioprosthetic valve sizing," *J Card Surg*, vol. 6, pp. 482-9, Dec 1991.

[197] A. N. Azadani, S. Chitsaz, P. B. Matthews, N. Jaussaud, J. Leung, T. Tsinman, *et al.*, "Comparison of mechanical properties of human ascending aorta and aortic sinuses," *Annals of Thoracic Surgery*, vol. 93, pp. 87-94, 2012.

[198] N. Gundiah, K. Kam, P. B. Matthews, J. Guccione, H. A. Dwyer, D. Saloner, *et al.*, "Asymmetric Mechanical Properties of Porcine Aortic Sinuses," *Annals of Thoracic Surgery*, vol. 85, pp. 1631-1638, 2008.

[199] M. A. Nicosia, J. S. Kasalko, R. P. Cochran, D. R. Einstein, and K. S. Kunzelman, "Biaxial mechanical properties of porcine ascending aortic wall tissue," *Journal of Heart Valve Disease*, vol. 11, pp. 680-687, 2002.

[200] P. B. Matthews, A. N. Azadani, C.-S. Jhun, L. Ge, T. S. Guy, J. M. Guccione, *et al.*, "Comparison of Porcine Pulmonary and Aortic Root Material Properties," *The Annals of Thoracic Surgery*, vol. 89, pp. 1981-1988, 2010.

[201] C. Martin, T. Pham, and W. Sun, "Significant differences in the material properties between aged human and porcine aortic tissues," *European Journal of Cardio-thoracic Surgery*, vol. 40, pp. 28-34, July 1, 2011 2011.

[202] N. Gundiah, P. B. Matthews, R. Karimi, A. Azadani, J. Guccione, T. S. Guy, *et al.*, "Significant material property differences between the porcine ascending aorta and aortic sinuses," *The Journal of heart valve disease*, vol. 17, pp. 606-613, 2008.

[203] C. Ferraresi, A. Manuelo Bertetto, D. Maffiodo, W. Franco, and L. Mazza, "One-dimensional experimental mechanical characterisation of porcine aortic root wall," *Medical and Biological Engineering and Computing*, vol. 37, pp. 202-207, 1999.

[204] D. C. Iliopoulos, E. P. Kritharis, S. Boussias, A. Demis, D. Koudoumas, C. D. Iliopoulos, *et al.*, "Rupture properties of aneurysmal aortic roots," in *2011 10th International Workshop on Biomedical Engineering*, Kos, Greece, 2011, pp. 1-4.

[205] T. Walther, T. Dewey, G. Wimmer-Greinecker, M. Doss, R. Hambrecht, G. Schuler, *et al.*, "Transapical approach for sutureless stent-fixed aortic valve implantation: experimental results," *European Journal of Cardio-thoracic Surgery*, vol. 29, pp. 703-708, 2006.

[206] K. H. Marzan GT, "A Computer Program for Direct Linear Transformation Solution of the Collinearity Condition and some Applications of it," *Proceedings of the Symposium on Close-Range Photogrammetric Systems*, pp. 420-476, 1975.

[207] A. K. S. Iyengar, H. Sugimoto, D. B. Smith, and M. S. Sacks, "Dynamic in vitro quantification of bioprosthetic heart valve leaflet motion using structured light projection," *Annals of Biomedical Engineering*, vol. 29, pp. 963-973, Nov 2001.

[208] W. Sun, A. Abad, and M. S. Sacks, "Simulated Bioprosthetic Heart Valve Deformation under Quasi-Static Loading," *Journal of Biomechanical Engineering,* vol. 127, pp. 905-914, 2005.

[209] K. J. Bathe, *Finite Element Procedures* Englewood Cliffs, NJ: Prentice Hall, Inc, 1996.

[210] M. S. Sacks, Z. He, L. Baijens, S. Wanant, P. Shah, H. Sugimoto*, et al.*, "Surface strains in the anterior leaflet of the functioning mitral valve," *Annals of Biomedical Engineering,* vol. 30, pp. 1281-90, 2002.

[211] J. Kim and S. Baek, "Circumferential variations of mechanical behavior of the porcine thoracic aorta during the inflation test," *Journal of Biomechanics,* vol. 44, pp. 1941-1947, 2011.

[212] T. Matsumoto and K. Hayashi, "Stress and strain distribution in hypertensive and normotensive rat aorta considering residual strain," *J Biomech Eng,* vol. 118, pp. 62-73, Feb 1996.

[213] M. A. Hajdu and G. L. Baumbach, "Mechanics of large and small cerebral arteries in chronic hypertension," *Am J Physiol,* vol. 266, pp. H1027-33, Mar 1994.

[214] E. Fonck, G. G. Feigl, J. Fasel, D. Sage, M. Unser, D. A. Rufenacht*, et al.*, "Effect of aging on elastin functionality in human cerebral arteries," *Stroke,* vol. 40, pp. 2552-6, Jul 2009.

[215] M. Garcia and G. S. Kassab, "Right coronary artery becomes stiffer with increase in elastin and collagen in right ventricular hypertrophy," *J Appl Physiol,* vol. 106, pp. 1338-46, Apr 2009.

[216] F. L. Wuyts, V. J. Vanhuyse, G. J. Langewouters, W. F. Decraemer, E. R. Raman, and S. Buyle, "Elastic properties of human aortas in relation to age and atherosclerosis: a structural model," *Physics in Medicine and Biology,* vol. 40, p. 1577, 1995.

[217] C. A. Conti, E. Votta, A. Della Corte, L. Del Viscovo, C. Bancone, M. Cotrufo*, et al.*, "Dynamic finite element analysis of the aortic root from MRI-derived parameters," *Medical Engineering & Physics*, vol. 32, pp. 212-221, 2010.

[218] M. Soncini, E. Votta, S. Zinicchino, V. Burrone, A. Mangini, M. Lemma*, et al.*, "Aortic root performance after valve sparing procedure: A comparative finite element analysis," *Medical Engineering & Physics*, vol. 31, pp. 234-243, 2009.

[219] M. A. Nicosia, R. P. Cochran, D. R. Einstein, C. J. Rutland, and K. S. Kunzelman, "A coupled fluid-structure finite element model of the aortic valve and root," *Journal of Heart Valve Disease*, vol. 12, pp. 781-789, 2003.

[220] A. Mangini, M. G. Lemma, M. Soncini, E. Votta, M. Contino, R. Vismara*, et al.*, "The aortic interleaflet triangles annuloplasty: a multidisciplinary appraisal," *European Journal of Cardio-thoracic Surgery*, vol. 40, pp. 851-857, October 1, 2011 2011.

[221] G. Marom, R. Haj-Ali, M. Rosenfeld, H. J. Schäfers, and E. Raanani, "Aortic root numeric model: Annulus diameter prediction of effective height and coaptation in post–aortic valve repair," *The Journal of Thoracic and Cardiovascular Surgery*, vol. DOI: 10.1016/j.jtcvs.2012.01.080.

[222] E. J. Weinberg and M. R. Kaazempur Mofrad, "A multiscale computational comparison of the bicuspid and tricuspid aortic valves in relation to calcific aortic stenosis," *Journal of Biomechanics*, vol. 41, pp. 3482-3487, 2008.

[223] A. Ranga, R. Mongrain, R. Mendes Galaz, Y. Biadillah, and R. Cartier, "Large-displacement 3D structural analysis of an aortic valve model with nonlinear material properties," *Journal of Medical Engineering and Technology*, vol. 28, pp. 95-103, 2004.

[224] F. Auricchio, M. Conti, S. Demertzis, and S. Morganti, "Finite element analysis of aortic root dilation: a new procedure to reproduce pathology based on

experimental data," *Computer Methods in Biomechanics and Biomedical Engineering,* vol. 14, pp. 875-882, 2011/10/01 2011.

[225] F. Auricchio, M. Conti, S. Morganti, and P. Totaro, "A computational tool to support pre-operative planning of stentless aortic valve implant," *Medical Engineering & Physics,* vol. 33, pp. 1183-1192, 2011.

[226] J. E. Bischoff, E. S. Drexler, A. J. Slifka, and C. N. McCowan, "Quantifying nonlinear anisotropic elastic material properties of biological tissue by use of membrane inflation," *Computer Methods in Biomechanics and Biomedical Engineering*, vol. 12, pp. 353 - 369, 2009.